Theses and Dissertations

Summer 2017

Intra-operative biomechanical analysis for improvement of intra-articular fracture reduction

Andrew Martin Kern
University of Iowa

Follow this and additional works at: https://ir.uiowa.edu/etd

Part of the Biomedical Engineering and Bioengineering Commons

Recommended Citation
Kern, Andrew Martin. "Intra-operative biomechanical analysis for improvement of intra-articular fracture reduction." PhD (Doctor of Philosophy) thesis, University of Iowa, 2017.
https://doi.org/10.17077/etd.52t7-4ngm

INTRA-OPERATIVE BIOMECHANICAL ANALYSIS FOR IMPROVEMENT OF
INTRA-ARTICULAR FRACTURE REDUCTION

by

Andrew Martin Kern

A thesis submitted in partial fulfillment
of the requirements for the Doctor of Philosophy
degree in Biomedical Engineering in the
Graduate College of
The University of Iowa

August 2017

Thesis Supervisor: Professor Donald D. Anderson

Graduate College
The University of Iowa
Iowa City, Iowa

CERTIFICATE OF APPROVAL

_____

PH.D. THESIS

_____

This is to certify that the Ph.D. thesis of

Andrew Martin Kern

has been approved by the Examining Committee for
the thesis requirement for the Doctor of Philosophy degree
in Biomedical Engineering at the August 2017 graduation.

Thesis Committee:_____
                 Donald D. Anderson, Thesis Supervisor

                 _____
                 Geb W. Thomas

                 _____
                 Nicole M. Grosland

                 _____
                 Joseph M. Reinhardt

                 _____
                 J. Lawrence Marsh

To Mandi,

Thank you for your love, support and patience.

ACKNOWLEDGEMENTS

ABSTRACT

Intra-articular fractures (IAFs) often lead to poor outcomes, despite surgeons' best efforts at reconstructing the fractured articular surface. The objective of articular fracture reduction is to improve joint congruity thereby lower articular contact pressure and minimize the risk of post-traumatic osteoarthritis (PTOA). Surgical fracture reductions performed using less invasive approaches (i.e., percutaneously) rely heavily upon C-arm fluoroscopy to judge articular surface congruity. Based on varied outcomes, it appears that the use of 2D imaging alone for this purpose may prove inadequate. Despite this, there has been little investigation into novel metrics for assessment of reduction quality.

This work first explores seven methods for assessment of reduction quality (3 2D, 3 3D, and one biomechanical). The results indicate that metrics which take 3D measurement or joint biomechanics into account when characterizing reduction quality are more strongly correlated with PTOA development.

A computer assisted surgery system, which provides up-to-date 3D fracture geometry and contact stress distributions intra-operatively, was developed. Its utility was explored in a series of ten cadaveric tibial plafond fracture reductions, where contact stresses and contact areas were compared in surgeries with vs. without biomechanical guidance.

The use of biomechanical guidance caused an increase in surgical time and fluoroscopy usage (39% and 17%, respectively). However, it facilitated decreases in the mean and maximum contact stress by 0.7 and 1.5 MPa, respectively. Contact areas engaged at known deleterious levels (contact stress > 4.5 MPa) were also 44% lower in cases which used guidance.

The findings of this work suggest that enhanced visualization of a fracture intra-operatively may facilitate improved long-term outcomes. Further development and study of this system is warranted.

PUBLIC ABSTRACT

Bone fractures involving load bearing joints such as the hip, knee or ankle (also known as intra-articular fractures or IAFs) are difficult to treat, as they often lead to a form of arthritis, post-traumatic osteoarthritis (PTOA). The effects of PTOA, such as joint pain and reduced mobility significantly degrade a patient's quality of life contributing to lost productivity, depression, obesity, and heart disease.

Surgeons attempt to prevent PTOA by accurately reconstructing fractured joint surfaces. Despite their best efforts, the prevalence of PTOA remains high. There is a growing body of evidence that joint reconstruction is limited by visualization and assessment of the fracture during surgery.

This work addresses this problem through the development of a computer-based visualization system for use during fracture reduction surgery. To determine appropriate information for display to the surgeon, multiple methods for assessment of fracture reduction are explored. It is found that methods that account for three-dimensional geometry of the fracture and mechanical function of the joint have strong correlations with PTOA development.

The computer-based visualization system is tested in a series of ten cadaver ankle fracture surgeries. It is found to have acceptable levels of accuracy and usability. Use of enhanced visualization corresponded to improved quality in joint reconstruction, as assessed by mechanical simulation. Implications for this work suggest that with further development this system may facilitate improved long-term outcomes following intra-articular fracture.

TABLE OF CONTENTS

LIST OF TABLES

LIST OF FIGURES

xi

CHAPTER 1: BACKGROUND AND MOTIVATION

Bone fractures are routinely treated by orthopaedic clinicians, and patients typically enjoy excellent outcomes. However, intra-articular fractures (IAFs), a subset of bone fractures that are treated surgically, present a greater challenge and more frequently lead to poor long-term outcomes. IAFs occur when one or more fractures extend through the weight bearing cartilage surface of a joint, where the mechanism of injury is typically a high energy impact, such as falls from a height, motor vehicle accidents, or sports-related injuries. Presentation of these fractures range from simple fractures with minimal displacement to complex and highly comminuted fractures. (Figure 1.1) Although varied treatment strategies for these injuries have been utilized, the incidence of poor outcomes remains high. Short-term complications (e.g., soft tissue breakdown, infection, malunion of fragments, and disruptions to circulation, etc.) lead to secondary procedures that pose additional risk to the patient. Even if short-term complications are avoided, the injury remains at risk long-term for development of post-traumatic osteoarthritis.[1, 2]

Post-traumatic osteoarthritis (PTOA) is a form of secondary osteoarthritis (OA) whose initiation can be traced to a known traumatic event. While symptomatically similar to idiopathic OA, PTOA is found in a much younger patient population and exhibits faster disease progression.[3] It has been estimated to affect 5.6 million individuals in the United States, and encumber $3 billion in direct healthcare costs.[4] Radiographically it is characterized by joint space thinning, growth of osteophytes, and eventual gross deformity of the joint. Pain, limited range of motion, and crepitus are hallmark symptoms of PTOA, which lead to reduced quality of life, lost productivity and other

comorbidities.[5] While the exact causes of PTOA are unknown, it is thought that mechanical injury to the cartilage begins a cascade of biological degradation, ultimately leading to disease.[6] Major contributing mechanical factors to the onset and development of PTOA include acute fracture severity joint instability and residual joint incongruity.[7] Although recent studies have found good correlation between each of these factors and PTOA development, the relative impact of each remains unclear.[8-10] While acute cartilage damage due to the injury is immutable, both joint stability, and articular congruity can be modified by clinical intervention. It is widely held that the quality of a surgical reduction (i.e., restoration of anatomical bone morphology) is the primary determinant of long-term outcomes following IAFs. Accordingly, treatment protocols almost universally emphasize the importance of joint restoration.[1-3]

The three main goals for treatment of IAFs in the ankle are "(1) anatomic restoration of joint surface; (2) rigid fixation of the fracture fragments; and (3) early mobilization of the ankle joint". [1] The most widely adopted treatment protocols for IAFs utilize open reduction and internal fixation (ORIF) of the bone fragments.[1, 7] Plates and screws are used to fix multiple bone fragments in an attempt to form a stable reconstruction of the original anatomy of the joint. Open reduction provides direct visualization of much of the fracture, and eases the implantation of fixation hardware. (Figure 1.1) However, large extensile approaches typically used in ORIF carry with them increased risk of post-surgical infection, and aggressive plating techniques have a greater risk of soft tissue breakdown.[11] In an attempt to avoid these complications several alternative surgical approaches have been adopted, such as external reduction with percutaneous fixation.[12] Although surgical approach is reported to alter both short- and long-term outcomes,

2

results are inconsistent between studies. The rate of poor outcomes of articular fracture remains high, despite continual efforts to achieve anatomical fracture reduction.[13]

Figure 1.1: Intra-articular fractures are high-energy fractures that exhibit idiosyncratic fracture patterns making their reductions difficult. ORIF and percutaneous reduction are two techniques used to achieve reduction and fixation of these fractures.

Regardless of surgical approach, modern tibial plafond fracture reduction involves the use of C-arm fluoroscopy to provide real-time feedback of bone and instrument position. Fluoroscopy is a projective radiographic imaging modality that provides low-radiation-dose images of patient anatomy. (Figure 1.2) While C-arm fluoroscopy is similar to conventional radiography, it trades image quality and field of view for low radiation dosage, enabling many images to be collected over the course of a procedure. Depending on the procedure and surgeon preference, C-arm fluoroscopy typically provides between 20 - 200 images over the course of a procedure to provide information that cannot be directly visualized. This tool allows a skilled surgeon to rely less on direct visualization, thus reducing incision size and associated complications.[11] Fluoroscopy images are limited in that they provide a two-dimensional projection of a three-dimensional world, which then requires mental interpretation.[6] (Figure 1.2) This can be unreliable where articular step-off, impaction, and gaps are either underestimated or missed.[14-18] It has been shown that surgeons are incapable of reliably assessing a number of key features on fluoroscopic images of fracture reduction.[14]

www.manaraa.com

While detecting mal-reduction of a fracture through fluoroscopic imaging is difficult, it can be more reliably measured through computed tomography (CT) imaging, direct visualization, and in some cases conventional radiography. [14, 16, 17] Direct visualization of bone fragments increases exposure of the injury and risk of infection. Three dimensional imaging modalities have limited applicability and practicality in a surgical setting. CT images may be obtained in the OR currently through the use of instrumentation such as the Medtronic O-arm,(Medtronic Surgical Technologies, Louisville, CO) however this device is cumbersome and delivers substantially higher radiation dose than fluoroscopy (to the patient and staff).[19] This has caused O-arms to be utilized primarily for spinal surgery procedures where its significant limitations are deemed an acceptable trade-off for increased navigation capability. Alternatively, modern state-of-the-art mobile C-arm fluoroscopy systems are capable of providing cone-beam CT images which also provide 3D volumetric imaging. Again while these systems are more flexible than standard CT instrumentation, they are prohibitively expensive, and offer increased radiation dose.[20] Both of these tomographic modalities perform a single static image, over the course of a fracture reduction would require multiple image acquisitions and vastly increase radiation exposure. While the information provided by 3D imaging modalities is highly desired by clinicians, current commercially available hardware has not met the practical needs for intra-operative use in fracture reduction. This highlights a need for systems which provide 3D visualization similar to tomographic imaging intra-operatively, which are cognizant of practicalities of these procedures.[6, 14] Computer-based tracking of individual bone fragments is a solution that may enable

4

surgeons to improve visualization of fracture reduction while maintaining familiar treatment protocols.
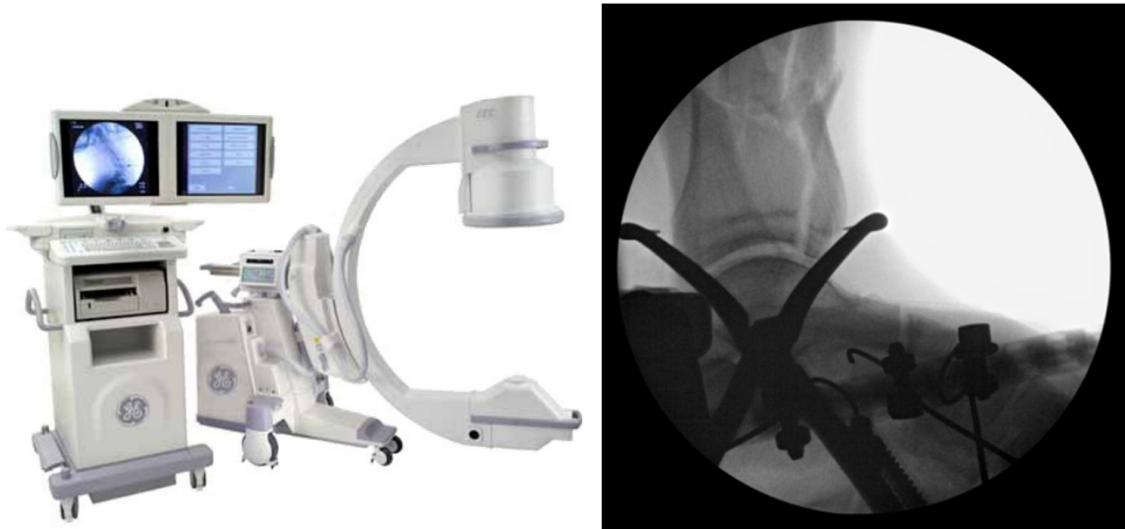
Figure 1.2: C-arm fluoroscopy is crucial in determining the positioning and orientation of bone fragments and surgical tools. This is a difficult task due to image distortion, resolution, and occlusion.

Surgical navigation systems and computer-assisted surgery have been used in research and clinical applications since the early 1990's with a marked increase in prevalence in recent years.[21] A wide range of systems have been tested and marketed, ranging from pre-operative planning tools, to hardware implantation guides, to augmented reality systems, and even full robotic surgery systems. In general these systems create a computational model of a real-world process, utilize instrumentation to synchronize the computer model to the real world, and then use that model to provide additional information that cannot otherwise be measured.[21] In orthopaedics, surgical navigation systems have largely relied on optical markers, anchored rigidly in bone, as the primary mode of synchronization.[22] These optical markers can be cumbersome, are subject to being dislodged, and are sensitive to visual obstructions. In IAFs, optical tracking systems are infeasible, where large numbers of small fragments are tightly

5

packed, and undergo large displacements and rotations (sometimes >90°), preventing simple placement of fiducials. As such, methods for markerless tracking of fracture reduction must be adapted and created for use within the OR.

Markerless registration of bones, while not widely used clinically, is well established in research settings.[23] Commonly referred to as 2D-3D registration, implementations of these systems vary across research groups. Accuracies are typically on the order of 0.2 mm and 0.5°, which is likely superior to what a surgeon is physically able to achieve.[24] Research systems are purpose-built, highly calibrated systems that acquire multiple simultaneous images, but they require large amounts of time, and have a high computational burden to process results. In recent literature a number of markerless registration methods have been adapted towards clinical use. [24-28] These systems have either failed to achieve registration speeds necessary for clinical use, demonstrate results in a realistic setting, or provide efficacy data indicating clinical improvement. In addition, none of these systems have been utilized to provide biomechanics data (e.g. joint contact stress, incongruity) which may be relevant to surgical outcomes. Specific adaptation of established methods, when tailored to provide real-time surgical feedback, can potentially improve surgeon performance and improve patient outcomes of IAFs.

Real-time 3D visualization of a fracture reduction presents a potentially significant shift in the manner in which IAFs are treated. Presentation of 3D models, articular incongruity measures, and contact stress distribution data will provide surgeons with a more complete mental representation of the fracture reduction. Improved understanding will aid in determining progression through the procedure, as well as the difficult risk-benefit analysis of when to finalize a procedure vs. continuing to pursue perfection. The

6

purpose of this work is to develop a software and hardware platform targeted to real-time tracking of bone fragments in a surgical setting. (Figure 1.3) This platform's accuracy, speed, and robustness are evaluated in the context of a publically available gold-standard dataset, as well as in a cadaveric surgical setting (introducing motion artifact, large motions of the C-arm, presence of surgical hardware). Once the 3D position of bone fragments can be reliably measured, a host of new information can be provided to the surgeon in the operating room. Computational simulations of contact stress are performed and delivered in near real-time to surgeons within a surgical environment. Finally, the efficacy of this system is explored in its ability to improve surgeon performance, in terms of speed, reduction quality, and contact stress.
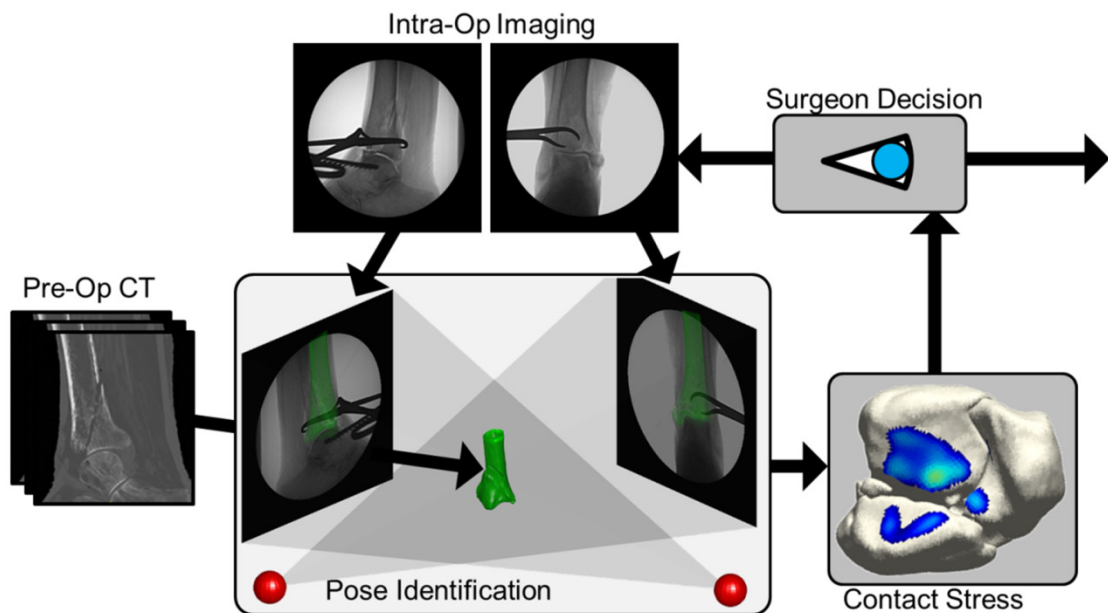
Figure 1.3: Proposed intra-operative contact stress assessment system uses pre-operative CT scans and intra-operative bi-plane imaging to determine the pose of fracture fragments, predict contact stress of fragments in these positions, and display results to the surgeon. The surgeon can use these results to determine progression through the reduction.

While PTOA is a significant problem following articular fracture across a multitude of joints, this study is focused on the talocrural joint (ankle). In many ways, the ankle is ideal for the study of PTOA as it has a low prevalence of primary OA, however following IAF incidence of PTOA is quite high.[29, 30] In practical terms, it is a small joint with minimal surrounding soft tissue enabling simpler dissection, access, manipulation and instrumentation.

In brief, the distal tibia and fibula form a mortise into which the talar dome is seated. During normal gait the tibia and talus articulate in a complex gliding motion which is stabilized laterally by the fibula and medially by the medial malleolus of the tibia. The geometry of an intact tibio-talar joint can be seen in Figure 1.4. In the following document, contact stress distributions (color-maps) will be displayed multiple times. To orient the reader, these color maps are always displayed on the distal articular surface of the tibia. (Figure 1.4)
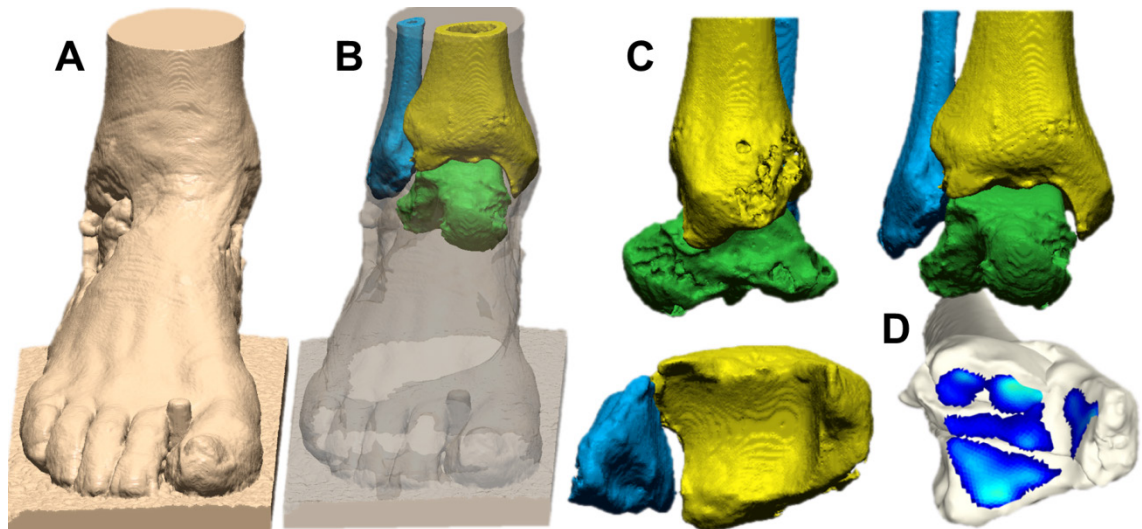
Figure 1.4: The human tibio-talar joint is the proximal most articulation in the ankle (A). It consists of 3 bones the tibia, (yellow) fibula, (blue) and talus (green). Sagittal, coronal and transverse views of these bones are shown (C). Subsequent sections of this document will display contact-stress distributions on articular surface of the distal tibia (D).

1.1 PREVIOUS LITERATURE

1.1.1 ARTICULAR CONGRUITY AND OUTCOMES

Restoration of the articular surface during fracture reduction has been recognized clinically for decades as an important factor in long-term outcomes.[1, 2] However, previous studies, which relate systematic measurement of articular reduction quality to outcome, have shown inconsistent results.[29] For example, in a review of 106 ankle fractures, Stufkens et al. 2010, found reductions classified as poor to be significantly less likely to have good or excellent outcomes (79.3% good results for optimal reduction vs. 25.5% good results for poor reduction.) and poor long-term outcomes.[31] The poor, fair or good assessment of fracture reduction quality was performed using post-operative radiographs. It is difficult to understand the reliability of these measurements, however, as it was a review of previously published case-reports from a variety of institutions. A similar finding from Berkes et al. 2013 showed ankles with articular step-off >2mm to have significantly worse pain and disability than ankles with <2mm step-off, using post-operative CT imaging in a cohort of 108 ankle fractures.[32] Multiple studies however, have found contradictory results showing no relation between articular congruity, and long-term outcomes. By rank-ordering radiographs of 25 tibial plafond fractures, DeCoster et al. 1999, found no correlation between reduction quality and patient reported outcomes.[33] Their analysis did find significant correlation between radiographic arthrosis scores and reduction quality, indicating some relation between these two factors. Additionally, ranking of injury severity was found to be correlated with reduction quality, indicating that more severe injuries tend to be more poorly reduced. In a later study from the same institution, Williams et al. 2004 similarly found a significant relationship between articular reduction quality and radiographic OA using rank-ordering of 32 tibial

plafond fractures.[34] Again, no significant correlation was found between patient reported scores and articular reduction quality; however, in-depth analysis of patient demographics found socioeconomic factors to have strong influence on self-reported scores. Wyrsch and McFerran 1996, in a study of 39 tibial plafond fractures, found no association between clinical outcomes and articular congruity assessed radiographically. They did however find that ORIF had significantly increased complication rates, compared to external fixation with limited internal fixation, showing a positive indication for the use of less invasive surgical technique. [35] While not a comprehensive review of prior work, this is illustrative of the difficulty of studying the influence of articular reduction, where variations in patient factors, study design, treatment and measurement techniques obfuscate causative factors.

Given the multi-factorial etiology of poor outcomes following IAF, variability between studies is perhaps unsurprising.[29, 36] Age, gender, soft tissue damage, fracture type, and fracture severity have all been found to be influencing variables in long-term fracture outcomes.[36] Comorbidities such as obesity, infection and diabetes have also been found as important in disease progression.[37] Variables such as age, weight, and obesity are common risk factors for many diseases and can be controlled with carefully designed analysis. Other influences, such as fracture severity or type are idiosyncratic and not typically robustly quantified. Although it is known that fracture severity on its own is correlated with long-term outcomes, typical qualitative clinical estimation has been found to be unreliable.[33, 38] Work has been performed to quantitatively measure articular fracture severity, however these methods have not yet been sufficiently refined for routine clinical use.[39] Perhaps wider-spread adoption of these quantitative measures of

10

fracture severity could help to elucidate the underlying importance of articular reduction quality.

Direct causes of poor long-term outcomes following articular fracture are thought to be due to aberrant mechanical loading. Conditions including acute impact injury, chronic overloading, and joint instability lead to a cascade of biological degradation which progresses into PTOA.[6, 7, 10, 40, 41] Although acute fracture severity has been shown as an important factor in PTOA development, it is not modifiable by clinical intervention.[10, 38] Conversely, chronic joint overloading is thought to be under direct control of the clinician through surgical reduction.

1.1.2 MECHANICAL FACTORS IN POOR LONG-TERM OUTCOMES

With the emphasis on anatomical reduction clinically, maintenance of mechanical function (alteration of contact stress) is implicit. This is supported by cadaveric analyses published in the literature relating contact stress patterns to articular incongruity. Fitzpatrick et al. 2004, varied articular step-off magnitude on a cadaveric posterior malleolus fracture. Although significant increases in contact stress were not measured, loading patterns were shifted to cartilage areas which normally do not see significant load.[42] This indicates not only the importance of contact stress magnitude but also the spatial location of articular contact. In cadaveric acetabular fractures, Hak et al. 1997 found a significant increase in contact stress as a result of both step-off and gap articular malreduction.[43] This altered articular contact stress has been related to biological changes, such as chondrocyte death, and alterations in cartilage metabolism.[7, 41] Computational studies such as Anderson et al. 2011 found a relationship between chronic contact stress exposure and poor outcomes on a cohort of 10 tibial plafond fractures

11

helping to complete the link between articular congruity, joint mechanics, biological changes and poor patient outcomes.[9]

1.1.3 VISUALIZATION OF FRACTURE REDUCTION

Based on the results of previous work, it seems that clinicians already strive for anatomical fracture reduction and the importance of restoration of joint mechanics is well understood. Despite improved understanding of the injurious loading mechanisms, articular congruity and disease progression following IAF, the prevalence of poor outcomes remains unchanged over the last several decades.[13] It is possible that other factors such as acute injury severity are prevailing, and development of biological treatment is required to see significant clinical improvement.[41] Conversely, there is a large body of evidence that clinical assessment of articular fracture reduction is inaccurate and unreliable.[6]

During ORIF procedures, direct visualization has long been considered the gold-standard for assessment and performance of articular reduction. In a series of syndesmotic reduction procedures, Miller et al. 2009, showed that cases which used direct visualization had significantly lower prevalence of malreduction than fluoroscopy. Despite the improvement, a substantial number of imprecise reductions (16%) remained with direct visualization.[44] There is additional evidence that ORIF has a greater risk for short-term infection and soft tissue breakdown due to increased trauma and exposure of the joint.[35, 37] Avoidance of these risks has caused clinicians to shift towards limited plating techniques, staged reduction with external fixation, and percutaneous reductions, all of which rely heavily on fluoroscopic imaging.[11]

Use of indirect visualization ultimately relies on the clinician's interpretation of a complex 3D scene from an imperfect, 2D projective image. A surgeon's internal representation of the fracture pattern (i.e. their "mental model") is informed by the provided image data.[45] This process is not fully understood, but Hu et al. 1994, found that clinician experience is a factor in eye gaze and motion patterns during detection of bone fractures.[46] This indicates that experience and training at least play some role in this interpretation. In general, this process is prone to error and mis-diagnosis.[47] In the application of articular fracture of the human ankle, Ebraheim et al. 2000, found that anteroposterior radiographs in isolation fail to adequately visualize the posterior aspect of the tibia.[15] The innovative technique used in this study progressively removed sections of the posterior malleolus of a cadaveric tibial plafond, and compared radiographs of these different sections. It was reported that only an extremely faint line was visible to highlight the posterior tibia. During surgical reduction, it seems likely this this faint indication is overlooked. Capo et al. 2009 compared fluoroscopic measurements from a closed reduction of a Bennett's fracture with direct visualization post-operatively. They found both fluoroscopic and radiographic measurement to vary significantly from direct measurement of fracture step-off and gap.[18] C-arm fluoroscopy was also shown to be insufficient for detection of rotational malreduction in syndesmosis repair by Marmor et al. 2011. Sensitivity of <0.3 was found in cases with the tibia externally rotated up to 30°.[48] Using CT as a gold-standard, Garner et al. 2015, examined the sensitivity of fluoroscopy and radiography for the detection of articular incongruity >2mm in 105 ankle fractures. It was found that fluoroscopy had extremely low sensitivity, (21%) and reliability for detection of articular incongruity. Radiography had only slightly better

13

sensitivity (36%) and reliability.[14] Similarly, Buchler et al. 2009, found that radiographic measures have poor accuracy for detecting a number of fracture features in tri-malleolar tibia fractures (measurement of a posterolateral fragment was the only finding with "good" accuracy). This study also emphasizes the need for CT assessment for tibia fractures, especially in cases which are "easy" as problematic features may evade detection.[17] Borrelli Jr. et al. 2002, performed a similar study in acetabular fractures finding again that radiography has poor sensitivity for detecting articular gap and step-off (25%). The authors also emphasized the need for pre-operative tomographic imaging to provide reliable assessment of fracture reductions.[16] The cumulative results of these publications sow serious doubts about the reliability and accuracy of purely radiographic imaging for the assessment of articular fracture reduction. It may also shed light on the seemingly erratic findings of studies relating articular congruity to long-term outcomes.[14, 32] Almost universally, the previous findings recommend CT imaging as a supplement for improving understanding of articular fracture morphology.

1.1.4 METRICS OF REDUCTION QUALITY

Despite the low reliability of articular congruity assessment and the known importance of joint mechanics on long-term outcomes, little work has been published on novel measures for fracture reduction assessment. To the best of our knowledge de Muinck Keizer et al. 2016, was the first publication to extend the concept of articular step-off and gap to a 3D surface-based measurement. They compute the surface area of the "void" left by gaps on the articular surface as well as 3D displacement of subchondral bone surface from their "intact" positions. Their study shows excellent reliability of their novel measurements, as well as correlation with more standard metrics of congruity.[49]

14

Unfortunately these metrics are not compared to outcomes, so it is difficult to understand their clinical applicability. As articular congruity is thought to be a proximate measure for articular joint mechanics, it may be useful to explore biomechanical measurement directly. Conconi et al. 2014, uses a measure of joint congruity derived from the Winkler elastic foundation contact model to predict early OA changes in the carpometacarpal joint.[50] Although they find no significant differences related to OA, this measure represents a unique merging of articular congruity and contact mechanics in joint assessment. Metrics of articular reduction which require use of CT-based measurement or complex data processing are likely of little utility clinically. If the surgeon is unable to interpret the reduction reliably intra-operatively it seems unlikely that pre- and post-operative measurements will provide meaningful improvement.

1.1.5 COMPUTER ASSISTED SURGERY IN FRACTURE REDUCTION

Computer assisted surgery (CAS) presents an opportunity to provide enhanced and novel information regarding articular fracture reduction, intra-operatively. Computer assisted surgery systems, in short, require "accurate, detailed patient-specific models of anatomy", "registration of the models to the patient", "maintenance of that registration", and "tracking of medical instruments in the surgical field".[51] This synchronization of patient specific anatomical data, with real-time actions in the operating room allows display of information that is otherwise unavailable. While a vast number of computer assisted surgery systems have been designed, published and even sold commercially.[21] Only a small number have been applied for the alignment of articular surfaces. Traditionally, CAS systems have utilized optical markers to perform real-time tracking of patient anatomy. Optical markers are identified and tracked using one or more pairs of

stereo cameras, positioned throughout the operating room. Using the known relative positioning of these points, a direct linear transform (DLT) is used to estimate the absolute position of optical markers within the room.[21] These markers are cumbersome as they need to be placed in the surgical field during while the patient is present, extending operative time. They protrude into the working area of the surgeon as they are often on long "tree" arrangements. They are also susceptible to being dislodged, requiring recalibration of the system. Alternatively, internal image-based (2D-3D registration) registration can be used to track anatomy visualized solely on fluoroscopic imaging views. While these techniques have been used in biomechanical research for decades, clinically their use has been limited.[23] This method involves matching a computer generated model to features on an operative clinical image. These features include shape contours, image intensity, gradients, shape invariants, and frequency components.[23] Clinical use of 2D-3D registration is limited by its high computational requirements and general inability to self-detect registration failure. The use of graphics processing units (GPUs) to perform tracking computations is quickly solving the former problem.[25] On the latter, Varnavas et al. 2013 and 2015 have presented novel methods of tracking and detecting registration failure which may be implemented in future systems.[52, 53]

A computer assisted surgery system for the repair of distal radius fractures has been presented in Gong et al. 2011. This system uses fluoroscopy-based 2D-3D registration to provide spatial information about the positioning of multiple bone-fragments relative to a pre-operative surgical plan. Reported alignment accuracy is reported to range from 1.53 to 2.79 mm, registration success rates are reported at 81 to 91% and reported registration times are on the order of 4 minutes.[54] While this study represents excellent progress

16

towards developing computer aided tracking of fracture reduction, it falls short in several key areas. Experiments are performed on simulated data and phantom-based data, which overly idealize a natural surgical setting. Realistically significant levels of noise would further inhibit registration accuracy and performance. The registration accuracy reported in this study is barely acceptable for the task of restoring joint congruity, as 2 mm is widely regarded as the threshold for "anatomical" reduction. Also the registration time required is suspect, as 4 minutes is likely too long for actual intra-operative use.

A hybrid fluoroscopy and optical based CAS system is reported in Zheng et al. 2008 for use in diaphyseal fracture reduction. This system uses a rigid optical tracking frame which is anchored to both halves of the diaphyseal fracture. These halves are registered to the tracking frame using image-based registration, and optical tracking is used for subsequent guidance. This allows for low-radiation or radiation-free progression throughout the operation. No quantitative data are provided about the performance of this system, however it is tested in a live patient trial.[55] The necessity of CAS systems for reduction of simple (un-comminuted) long-bone fractures is unclear. Particularly difficult cases that may benefit from this system are likely to have many highly comminuted fragments, which are not accommodated by the described framework.

A novel robotic CAS system for articular fracture reduction is presented in Dagnino et al. 2017. This system again is a hybrid 2D-3D and optical-based registration. Large optical fiducial trees are anchored in fracture fragments and 2D-3D registration is used to co-register the fiducials and fragments. Optical tracking is used to further guide the surgery. Robotic manipulators are used to precisely reduce each fragment following a subject-specific pre-operative plan. Registration accuracy is reported as 0.88 and 1.15

mm for phantom and cadaver surgeries, respectively. The final error in reduction was found to be 1.2 mm or 2°. Registration time is reported on the order of 40 minutes, and total surgical time is on the order of 110 minutes.[56] This system shows interesting and promising results, however it is unclear how many simultaneous fragments can be tracked with the use of optical fiducials. The size of fragments relative to the optical tracking trees is also a potential concern when definitively fixing the fragments, where the guidance instrumentation may block optimal screw placement. The registration time is also likely prohibitive for clinical use. The authors mention they are likely to improve this element in the next iteration of the system. Finally, when the robotic system fails, it may be difficult for an orthopaedic surgeon to intervene with the vast alteration to the layout of the operating room.

Murphy et al. 2014, reports the implementation and usage of a CAS system which measures joint biomechanics in real-time intra-operatively. This system, which they refer to as a biomechanical guidance system (BGS) is designed for use in periacetabular osteotomy. In this procedure the clinician frees the acetabulum from the pelvis with a series of osteotomy cuts, performs a complex realignment to improve joint biomechanics (presumably) and then fixes the acetabulum in the new orientation. The BGS system detailed in this study uses optical tracking and fiducials to track surgical instruments, the acetabulum, and the pelvis. Joint mechanics are computed using an expedited contact stress analysis metric, discrete element analysis (DEA). The BGS is evaluated in nineteen cadaveric validations, and system accuracy is found to be 1.4 and 1.8 mm in translation and 1.0 and 2.2° in rotation.[57]

The BGS presents an exciting new development in CAS, particularly in the context of joint surgery, as it paves the way for assessment of joint mechanics rather than simply incongruity. It seems likely that congruity of a joint does not capture all aspects of joint morphology important to long term outcome. Accordingly, systems which measure known mechanistic indices of poor outcome following articular fracture may enable improved results from these devastating injuries. Although advancements have been made in CAS systems which track articular fracture reductions, as well as systems which monitor joint biomechanics during joint surgery, no one study has demonstrated both simultaneously. Additionally, analysis of these systems falls short either by failure to demonstrate performance in a realistic setting, or by failure to provide any indication of clinical performance or efficacy. A need remains for a system which estimates joint biomechanics intra-operatively, during articular fracture surgery, using unobtrusive methods that are applicable to a wide variety of articular joint fractures.

CHAPTER 2: METRICS OF ARTICULAR REDUCTION QUALITY

Achievement of "anatomical" articular reduction has long been considered a primary determinant of outcomes following intra-articular fracture (IAF).[13, 15, 16, 18, 58] In particular, it is believed that a poorly reconstructed joint causes an aberrant mechanical environment, resulting in the onset and progression of post-traumatic osteoarthritis (PTOA).[6, 7, 10, 13] This is particularly true in the talocrural joint, where incidence of primary osteoarthritis is rare – as many as 78% of ankle OA cases have been reported to be post-traumatic in origin.[29, 31] In addition, it has been shown there is a relation between articular incongruity, joint mechanics and long-term patient outcomes.[9, 32] Despite the importance placed on these reconstructions, clinically the "quality" of a fracture reduction is often assessed using manual measurements from 2D radiographic techniques.[14] To date, little research has been conducted exploring assessment of reduction quality, using novel 3D imaging and modeling methods.[6, 49]

In typical surgical procedures, assessment of articular congruity/reduction quality has been determined through manual measurements on 2D projective imaging (radiography or fluoroscopy), or 2D slices from tomographic imaging.[59] With projective imaging, these manual measurements are subject to significant error due to projective distortion, and difficulty of image interpretation. In a cohort of 174 ankle fractures Garner et al. 2015 showed that only 21% of intra-articular step-off >2mm could be detected using fluoroscopic vs. CT imaging.[14] These results align with findings from similar studies that compared radiography to CT, drawing into question the validity of projective imaging techniques for direct assessment of articular reduction quality.[15-18, 48] In regard to patient outcomes, direct 2D measurement from projective and

20

tomographic images may be suboptimal as they typically rely on a small number of measurements, selected from limited views. Difficulty with image interpretation from limited viewpoints, or biased selection of a small number of measurements, may reduce the effectiveness of these 2D measurement techniques.

Two novel metrics for the assessment of articular reduction quality have been developed to potentially reduce the limitations of traditional 2D projective and tomographic metrics. First, a three dimensional articular step-off metric was developed. This metric accounts for discontinuity across the entire articular surface rather than a subset of user selected measurements. It was hypothesized that by measuring incongruity over the entirety of the joint, values near the periphery of the joint, possibly of reduced mechanical importance, may introduce error. To reduce the effects of this error, schemes such as weighting values near the articular surface more heavily were explored, however a more direct metric was chosen. Second, a biomechanical metric, contact stress-time exposure computed with finite element analysis (FEA), was tested in an attempt to capture both the geometry of the joint and its effect on patient biomechanics. Both metrics rely on data derived from a 3D CT segmentation of the fractured limb, thus reducing sensitivity to image acquisition plane.

The objective of this study was to compare standard 2D metrics of articular fracture reduction quality with two novel metrics: 3D step-off and contact stress exposure computed with FEA. Measurement techniques for the 2D, 3D, and biomechanical metrics are described and demonstrated on CT data from a cohort of ten post-operative tibial plafond fractures. (Figure 2.1) These metrics are evaluated relative to two-year post-op Kellgren Lawrence (KL) grade, a score of radiographic OA, as an early indication of their

21

predictive ability for OA outcomes.[60] KL grade is a radiographic score, based on a plain film standing radiograph. Features such as joint space narrowing, osteophyte growth, and bony geometry are identified. A score ranging from 0-4 is assigned, where 0 indicates no evidence of disease and 4 indicates presence of severe OA.
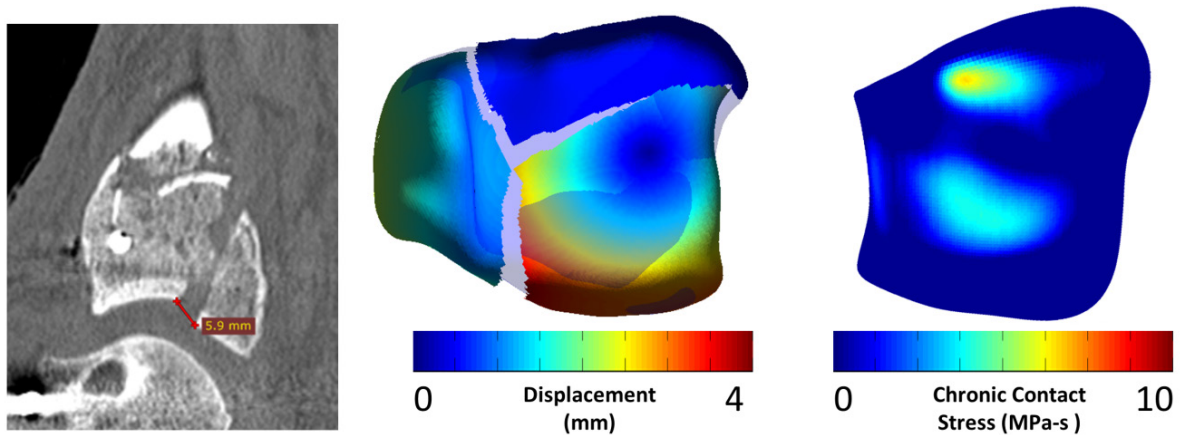
Figure 2.1: 2D metrics (left), 3D metrics (middle) and biomechanical metrics (right) are all compared in a cohort of 10 post-op tibial plafond fracture subjects.

2.1 METHODOLOGY

Clinical CT data from 10 tibial plafond fractures treated at the University of Iowa Hospitals and Clinics was gathered from a previous FEA study of contact stress and OA severity.[8] More complete information regarding subject demographics can be found in Anderson et al. 2011.[9] In brief, the cohort consisted of 8 male and 2 female subjects with mean ages of 32.4±6.9 years and mean body mass of 92.7±16.2 kg. CT scans of the post-op fractured and intact contralateral limbs were acquired using standard orthopaedic protocol within 12 hours following definitive reduction. Scans were acquired with in-plane resolution from 0.25 to 0.5 mm and slice thickness of 0.3 to 0.5mm following reconstruction.[8]

Segmentation of the CT data to generate surface models for FEA mesh construction was performed in the previous study. This was completed using an iso-surfacing algorithm to acquire a preliminary surface model (OSIRIX software, www.osirix-viewer.com), followed by manual smoothing and cleaning operations performed in Geomagic Studio (3D Systems, Rock Hill, SC, USA) . Further details about the segmentation and FEA meshing process can be found in Li et al. 2008.[8]

2.1.1 2D MEASUREMENT

The simplest measurement technique utilized, meant to mimic measurements commonly performed by clinicians, was metrics of 2D step-off taken from CT slices. Using a graphical interface, a trained clinician was presented with a single slice of a CT volume, and a set of manual measurement tools. On each slice, the clinician was instructed to identify the largest articular incongruity by drawing a line bridging the gap between these two discrete sections. (Figure 2.2) If more than one fracture was present, the clinician was instructed to select the largest incongruity for each slice. The length of this line was recorded as 2D articular incongruity metric. This measurement was performed on each slice of the CT volume in both sagittal and coronal reconstruction planes. Data were reduced to a single value for each viewing plane by selecting the maximum value through the thickness of each plane. To account for fracture lines oblique to the CT reconstruction plane a third measurement, 2D distance, was also computed where $dist_{sag}$ and $dist_{cor}$ represent manual measurement in the sagittal and coronal reconstructions, respectively (Eq. 2.1).

$$2D \ Distance = \sqrt{dist_{sag}^2 + dist_{cor}^2}$$

2.1

23
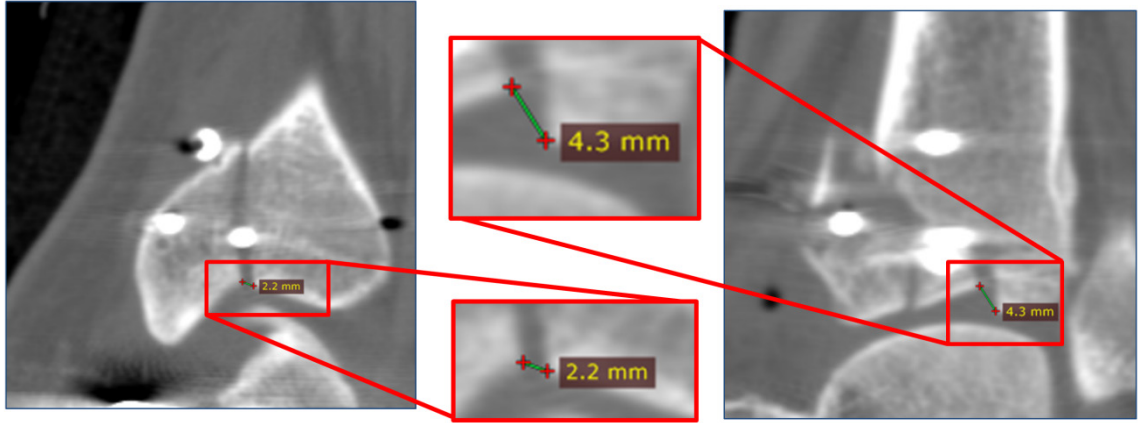
Figure 2.2: 2D measurements performed manually by connecting the fracture edges of largest articular discontinuity of every slice in sagittal (left) and coronal (right) views. This is repeated for all CT slices containing fractured articular surface. The maximum value for each view is recorded.

2.1.2 3D MEASUREMENT

A 3D measurement technique, based on segmentations of the subchondral bone surface, was developed in an attempt to address potential shortcomings of 2D techniques. In short, this metric relies upon measurement of the rigid spatial transformation required to bring surface geometry of the intact contralateral bone into registration with post-op fractured bone surface.

Processed surface models of the intact contralateral bone (obtained from CT segmentations) are mirrored, and aligned to the intact contralateral bone using an iterative closest point algorithm (ICP).[61] The articular surface of the intact bone is segmented into individual articular fracture regions (AFRs) corresponding to the articular regions of independent fracture fragments. This is a manual process completed using the region selection tool in Geomagic Studio, and it results in a separate surface model for each AFR. (Figure 2.3) If appropriate correspondence between the intact and fracture surfaces could not be identified, that area is labeled as segmental defect and omitted from all AFRs. Each AFR is registered to its corresponding fragment on the post-op surface

24

model using the ICP alignment tool within Geomagic Studio. The homogeneous spatial transformation, T_j^{AFR}, which brings AFR j into registration with the post-operative fractured bone, is recorded for all m fragments (AFRs) within a case.
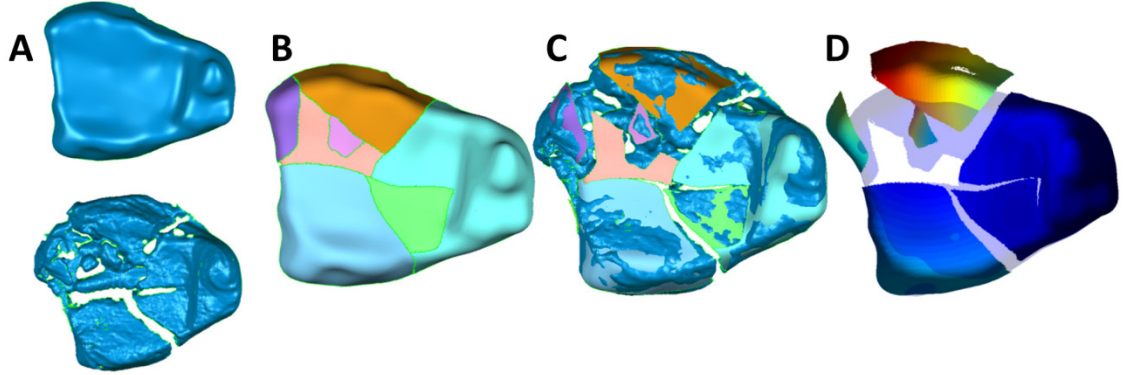
Figure 2.3: 3D measurements performed using surface model of intact contralateral joint (A top) and post-op fractured joint (A bottom). The intact model is manually separated into regions corresponding to fragment articular surfaces (AFRs) denoted by different colored regions (B). Individual AFRs are aligned to post-op fractured orientation (C) using an iterative closest point algorithm. The Euclidean distance traveled by vertices on each AFR, are reported (D).

The surface models of individual AFRs and their corresponding transformations are processed with a custom MATLAB (Matlab 2014a, Mathworks, Natick, MA, USA) algorithm, which quantifies the Euclidean distance between each AFR in intact and fractured positions. Displacement of each vertex, v_i, within an AFR is recorded, and mean displacement (Eq. 2.2) and max displacement (Eq. 2.3) computed for each AFR.

$$AFRMean_j = \frac{1}{n}\sum_{i=0}^{n}\left\|v_i - T_j^{AFR}v_i\right\|$$

2.2

$$AFRMax_j = \max_{i=0...n}\left\|v_i - T_j^{AFR}v_i\right\|$$

2.3

Three final distance metrics are recorded for each total fracture; Metric 1 (Eq. 2.4) consists of the mean of each $AFRMean$; Metric 2 (Eq. 2.5) is the maximum of the $AFRMean$ values; Metric 3 (Eq. 2.6) is the maximum of the $AFRMax$ values.

$$Metric\ 1 = \frac{1}{m}\sum_{j=0}^{m} AFRMean_j$$

2.4

$$Metric\ 2 = \max_{j=0\ldots m}\{AFRMean_j\}$$

2.5

$$Metric\ 3 = \max_{j=0\ldots m}\{AFRMax_j\}$$

2.6

2.1.3 BIOMECHANICAL MEASUREMENT

The final metric explored as an indicator of articular reduction quality, was contact stress-time exposure, as reported in Anderson et al. 2011. The identical contact stress-time exposure data derived from FEA was utilized for this study. In brief, contact stress was computed from a discretized 13 step gait cycle on 10 post-op fractured ankles. Hexahedral finite element meshes of the subchondral bone and cartilage were constructed according to subject specific geometry. Cartilage was treated as linear elastic and isotropic, (Young's Modulus of 12 MPa, Poisson's ratio of 0.42).[8] For complete details on the mechanical analysis performed see Li et al. 2008 and Anderson et al. 2011.[8, 62]

Following mechanical analysis, contact stress-time exposure was calculated as the product of the percentage of articular surface area which exceeded a contact stress threshold P_d (MPa) which also exceeded a contact stress-time threshold P_{dose}^{crit} (MPa-s)

26

these were selected as 4.5 MPa and 3.0 MPa-s respectively. (Eq. 2.7) Again, this methodology and dataset has been reported previously by Anderson et al. 2011.

$$\widehat{P}_{\text{Stress}-\text{Time}} = \sum_{i=1}^{13} \frac{area(P_i > P_{dose}^{crit} \ \& \ P_i > P_d)}{area(P_i > P_d)}$$

2.7

2.1.4 EXPERIMENTAL DESIGN

Measurement of six geometrical metrics (3 two-dimensional and 3 three-dimensional) were performed by a single rater. Correlation of all 7 metrics (6 geometrical and 1 biomechanical) were correlated with two-year post-op KL grades, using Pearson correlation ($\alpha = 0.05$). To determine if the strength of correlation with KL grade were significantly different within the 7 metrics, Meng's Z-test was used. [63]

2.2 RESULTS

All 7 metrics were computed successfully on the ten included subjects. Results visually comparing articular contact stress and 3D step-off can be seen in Figure 2.4.
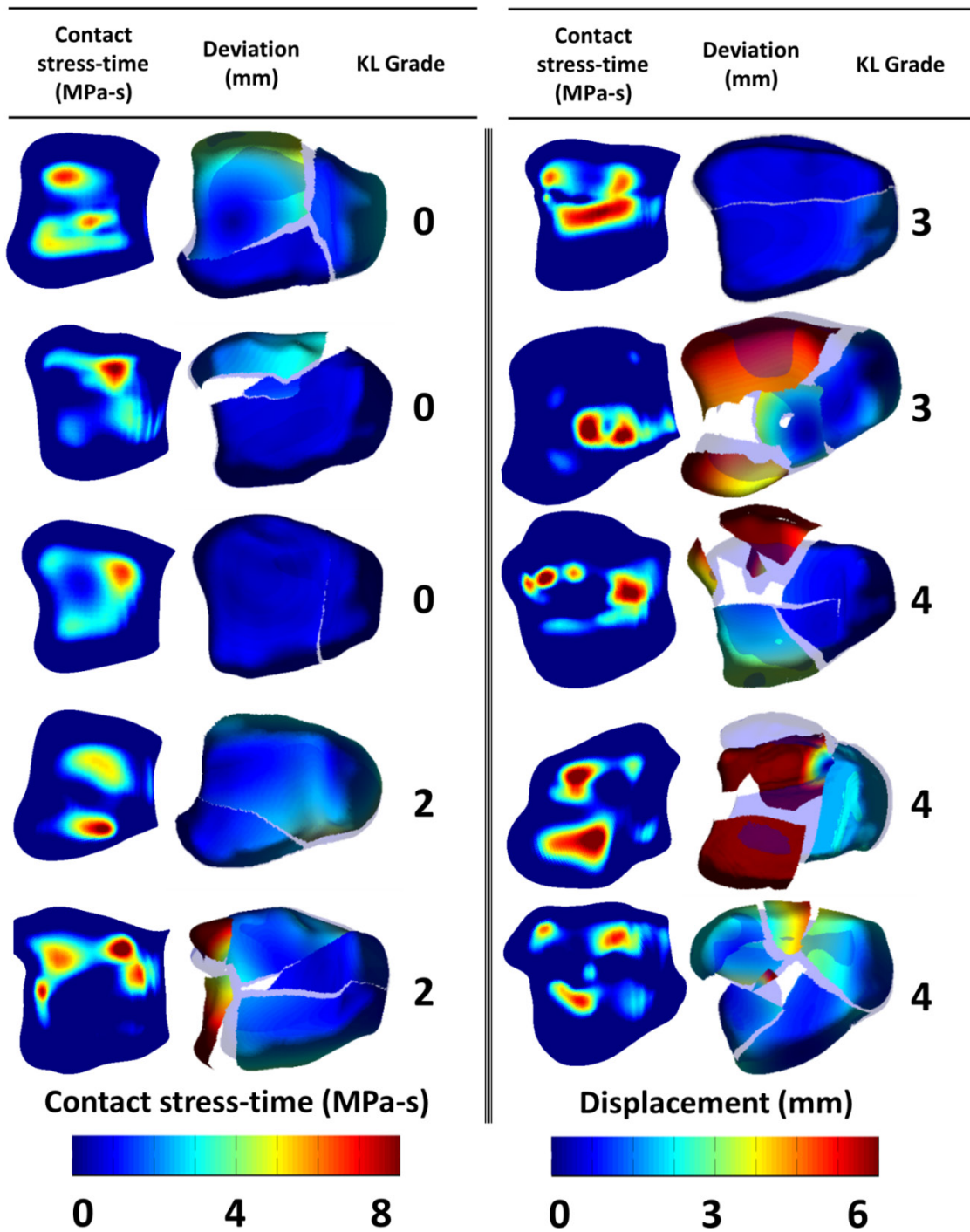
Figure 2.4: Contact stress-time (MPa-s) (left column), 3D displacement (right column) and KL Grade. Focal concentrations of contact stress, visually compare well to areas of high fragment displacement.

There was a significant correlation of 3D step-off metrics ($p < 0.05$), and contact stress exposure ($p < 0.001$) with KL Grade (Table 2.1). Using Meng's Z-Test to compare correlated correlation coefficients, significant differences were only present between

28

contacts stress exposure/2D sagittal step-off, and contact stress exposure/2D distance (Table 2.2).[63]

Table 2.1: Two-tailed Pearson Correlation of Articular Reduction Quality Metrics with KL Grade

Correlation of Seven Articular Reduction Metrics with KL Grade		**mean ± std**	**r (p-value)**
2D Step-off	**Coronal**	6.3 ± 5.3	0.58 (0.081)
	Sagittal	5.1 ± 4.9	0.48 (0.163)
	Distance	8.2 ± 7.2	0.54 (0.108)
3D Step-off	**Metric 1**	2.4 ± 1.8	0.66 (**0.040**)
	Metric 2	3.9 ± 2.9	0.69 (**0.027**)
	Metric 3	5.9 ± 4.1	0.70 (**0.024**)
Contact Stress	**Exposure**	35.7 ± 11.5	0.86 (**0.001**)

Table 2.2: Strength of Correlation of Comparisons of Seven Articular Reduction Quality Metrics with KL Grade Measured by Meng's Z Test

Correlation Comparison of Seven Articular Reduction Metrics with KL Grade (Mengs' Z Test p-values)						
2D Step-off		**3D Step-off**			**Contact Stress Exposure**	
Sagittal	**Distance**	**Metric 1**	**Metric 2**	**Metric 3**		
(0.127)	(0.135)	(0.384)	(0.310)	(0.303)	(0.056)	**Coronal**
	(0.124)	(0.283)	(0.212)	(0.205)	(0.042)	**Sagittal** (2D Step-off)
		(0.341)	(0.267)	(0.261)	(0.050)	**Distance**
			(0.321)	(0.280)	(0.138)	**Metric 1**
				(0.389)	(0.166)	**Metric 2** (3D Step-off)
					(0.180)	**Metric 3**

2.3 DISCUSSION

Based on these results, 2D measurements even from tomographic imaging do not adequately describe the quality of joint reconstruction. No statistically significant

29

www.manaraa.com

correlation was found between our 2D measurements and KL grade, indicating that these measurements have no relation to post-operative outcomes and may omit important information. This is corroborated by the findings of de Muinck Keizer et al. 2016 who report that their own novel metric of 3D articular incongruity have only fair correlations with traditional 2D step-off measurements. They show systematic differences between these measures indicating disparate information content.[49] However, their study failed to compare these measures to outcomes and was unable to indicate that addition of 3D information provides clinical value. Other work has attempted to separate 2D measures of articular incongruity into displacement normal to or parallel with the articular surface. Use of these sub-groupings may have proven useful in our analysis, however it was deemed that they would be subject to significant error from fracture lines not aligned to the CT reconstruction planes.

While two-dimensional measurements from CT slices are certainly enticing for their relative ease of use they do not leverage the fully three-dimensional data available from a CT scan. It is easy to imagine a case in which an articular incongruity does not lie fully within the CT acquisition plane, and is incorrectly measured by relying solely on these planes. Although reconstructing the CT volume from a different orientation may be a suitable solution on a case-by-case basis, it is a time consuming process that is not easily generalizable.

The use of 2D tomographic methods as a gold standard for assessment of articular fracture reduction, is unsupported by our results. While the use of these 2D metrics is certainly more reliable and accurate than projective radiography, it does not appear to be strongly predictive of long-term outcomes.[14, 16, 17] The use of more advanced 3D

30

bar

measurement techniques appears to provide an accurate measure that is predictive of long-term patient outcome.

Both of our novel metrics of articular incongruity were significantly correlated with KL grade outcomes, indicating the need for more robust measures of articular incongruity. Despite the small sample size used, the strength of correlation was significantly different between two of the 2D measures vs. contact stress exposure (Table 2). The use of biomechanical metrics instead of purely geometrical measures, may allow for better assessment of how a particular incongruity affects the cartilage mechanical environment. Although the strength of correlation of 3D step-off metrics with KL grade and contact stress exposure with KL grade were not significantly different, it is still apparent the biomechanical metric may provide information missed by a purely geometric measure. This is exemplified by subject 6 (Figure 2.4, top right) where all measures of 2D and 3D step-off were low (25th and 15th percentile, respectively), however contact stress exposure was the 3rd highest exhibited (75th percentile) in the ten cases examined. While well reduced in terms of congruity, the relative angle of the two articular surface fragments was "pinched", altering articulation with the opposing talar dome. This type of malreduction is insidious as, to the best of our knowledge, there is no simple visual indication of its presence. It can occur in seemingly simple fractures and is capable of causing substantial alterations to articular contact stress necessitating biomechanical analysis rather than measurements of articular step-off.

This study was limited by the use of a small number of total subjects. Construction of the finite element mesh and computation of contact stress using FEA, were the main restrictions in using additional subjects. Recent development of expedited computational

techniques for measuring contact stress provides a means of computing contact-stress exposure on a much large number of articular fractures.[50, 64-67] The 3D articular incongruity metric also requires a substantial level of user input to correctly identify and register individual AFRs. In this study, only one rater was used to perform the 3D articular incongruity analysis. Reliability within and between raters, is currently unknown, and future work with these metrics should attempt quantification of these metrics. There are also concerns with the requirement of intact bone geometry to serve as a template for joint displacement. Recent advancements in virtual fracture reconstruction, may serve to eliminate this process and expedite the computation of 3D displacement measures.[68, 69] The main outcome metric, KL grade, is an indication of radiographic OA based on individual clinician rating. While the reliability of KL grade measurement is good, it is not an indication of functional disability or patient pain. Future work could gather other metrics of long-term patient outcomes, to better understand the relationship of articular incongruity and disability.

Computation of reduction quality post-operatively is useful scientifically, but may be of less use clinically. Surgeons are unlikely to re-operate on a patient regardless of any measure of reduction quality due to the cost and risk of repeated surgical operations. In addition, if unable to correctly restore anatomy originally, it seems unlikely re-operation would guarantee success.[14, 70] This highlights the need to provide meaningful metrics of articular reduction quality to surgeons in the intra-operative setting where errors can be immediately analyzed and addressed, in efforts to promote optimal patient outcomes.

All of the metrics used this study are a distillation of the condition of the entire joint surface into a single numerical value. This is certainly convenient for statistical measures

32

and database studies, however on an individual basis it may be an oversimplification. Intra-operatively, it is unclear what specific action should be taken if presented with a single value signifying a "bad" reduction. Such a value represents that the current reduction is insufficient, but offers little insight about a path to improvement. Outside of matching data to a pre-operative plan, development of an assessment which is predictive of long-term outcomes, yet easily interpreted in an actionable manner, remains an area in need of additional investigation.

Intra-operatively, the mental, visual and physical task of assessing, reducing and fixing a complex fracture is challenging, even to experienced orthopaedic surgeons.[47, 58] Calculation and presentation of articular reduction quality metrics to the clinician intra-operatively also adds significant challenge due to time, imaging and instrumentation challenges. This metric must be concise, intuitive and actionable such that a surgeon can quickly determine if a current reduction is adequate, identify a correction, and implement that correction.

In an attempt to achieve this goal, a system has been developed to provide the surgeon with both 3D visualization of an articular fracture and a biomechanical analysis of its contact stress, intra-operatively. In Chapter 3 the design and development of this system is described. In Chapter 4 this system is evaluated in a series of 10 cadaveric tibial plafond fracture surgeries.

CHAPTER 3: INTRA-OPERATIVE BIOMECHANICAL ASSESSMENT

Based on the results presented in Chapter 3, a computer assisted surgery (CAS) system was developed as a means of presenting meaningful metrics of articular reduction quality (beyond the capabilities of 2D modalities), in an intra-operative setting. In the context of this work, the system provides a dynamic 3D visualization of the fracture, and a 3D contact stress distribution indicating the expected biomechanics of the joint. To differentiate this CAS system from existing systems, the term "Biomechanical Guidance System" (BGS), to the best of our knowledge first used in Murphy et al. 2015, has been adopted.[57] Despite the existence of numerous commercially available CAS systems with orthopaedic application, this is the first system to provide biomechanical (contact stress) feedback in the application of articular fractures. This fundamentally new biomechanical information is an important point of differentiation, as it allows potential quantification and prediction of long-term outcomes. Ultimately, the surgeon can shift their concern from an ill-defined and likely unachievable goal of "anatomical reduction" to a more quantifiable "biomechanical reduction".

In brief, surgical implementation of the BGS begins with a technician performing pre-processing on a pre-operative CT scan prior to surgery (1-2 hours required) (Section 3.2.2). Intra-operatively, a small calibration object is placed beneath the fractured anatomy and remains for the duration. Separate from this, the reduction operation proceeds as typical. If at any point the surgeon is unsure of the reduction, or requires confirmation, the fluoroscopy technician obtains two approximately orthogonal fluoroscopy images (shots). The shots are immediately sent to a workstation, (Section 3.1.3) which calibrates the images (Section 3.2.3), identifies the position of bone

fragments (Section 3.2.4), and computes contact stress (Section 3.3). This process is guided by a technician and requires no clinician input (Section 3.2.5). Finally, a three dimensional representation of the fracture and the contact stress pattern, is displayed to the surgeon. The clinician uses this information to determine how to progress with the reduction. This entire process requires ~1-2 minutes depending on the complexity of the fracture and image quality. The BGS can be used at multiple time-points throughout the procedure where the number of uses is primarily limited by time. Only two additional fluoro images are required for every use of the BGS.

The BGS, as with other CAS systems, is a high order computational model of real-world processes which is synchronized with the operation by means of specialized instrumentation. This model provides a means of obtaining information too difficult, destructive, costly or undesirable to measure directly. In the case of the BGS this information is an interactive 3D visualization of the fracture and contact pressure distribution. Counter to many CAS systems in use today, this system was designed to provide functionality with minimal interruption to standard clinical practices and the specialized instrumentation required is minimal.

As is, the current system requires a C-arm fluoroscopy unit with navigation capabilities (available on most new midrange mobile fluoroscopy units), a computer workstation equipped with proprietary software, a large display for administering surgical results, and a specially machined calibration object within the view of the C-arm. The BGS avoids traditional optical trackers, as they are tedious to place, susceptible to loss of registration and particularly ill-suited to use with many small tightly packed bone fragments. Elimination of these trackers eases adoption of this system by clinicians, as its

35

operation does not require their direct input. All operation is handled by technicians, and the surgeon must only learn to incorporate 3D views and contact stress patterns into their lexicon. Instead, the BGS uses images obtained from C-arm fluoroscopy to determine the position of individual bone fragments. While this precludes "real-time" tracking of bone objects, it drastically reduces the hardware complexity of the tracking system. Contrary to many modern CAS systems, the BGS does not force the surgeon to follow a pre-determined pre-operative plan. It attempts to augment the information available to the clinician and thus enhance their decision making ability. This is germane specifically in fractures where idiosyncratic injuries require adaptation during reduction in terms of approach and fixation.

This section outlines the design of the BGS and its implementation. First, the hardware requirements and utilization in the context of the BGS are detailed, including computational resources, imaging hardware and other physical instrumentation. Description of the hardware provides context for details of the software components of the BGS. Data preprocessing, registration of bone fragments, contact stress computation, data visualization and user interface are all specifically detailed here. Following description of the system, behavior of individual components is evaluated and validated using synthetic, experimental, and gold-standard data.

3.1 HARDWARE

There are three main pieces of hardware required in the OR to use the BGS; a computer workstation; a C-arm with navigation capabilities; and a specially machined reference object. (Figure 3.1)
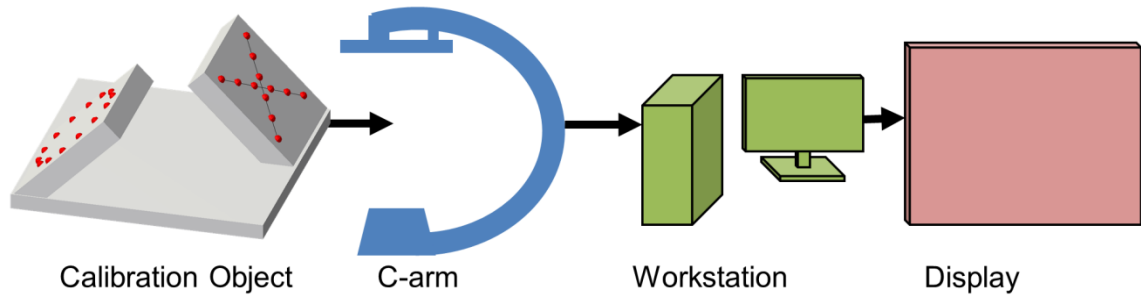
Figure 3.1: Overview of hardware required for operation of the BGS. A calibration object (left) is the only object required within the surgical field. It serves as a references coordinate frame for surrounding objects and is placed within the field of view of the C-arm. Image data from the C-arm is transferred to a computer workstation with BGS software. When results are computed 3D bone models and contact stress distributions are displayed to the surgeon.

3.1.1 FLUOROSCOPY SYSTEM

Use of C-arm fluoroscopy is currently standard of care for articular fracture reduction. It is a form of projection radiography which allows the surgeon to obtain static and dynamic (video) images of the fracture and surgical hardware. These systems are low dosage, enabling many images to be taken over the course of a procedure, and offer a variety of positioning option allowing flexibility according to procedure or surgeon preference.

As C-arm fluoroscopy systems are versatile and common clinical imaging tools, dozens of makes and models are currently available on the commercial market. Despite differences in size, intended use, and technology used, generally they all consist of a gantry in the shape of a "C". There is an X-ray tube on one end of the gantry directed toward a detector on the opposite. The gantry can be moved manually (motorization available on high-end units) to position the system. While a comprehensive discussion of C-arm fluoroscopy is outside the scope of this study, there are several features of importance to note. Fluoroscopy images are formed using two primary types of detectors, image intensifiers (II) or flat panel detectors (FPD).

37

Image intensifiers utilize large vacuum tubes to focus and amplify incident X-ray's, allowing use of low dosage while maintaining image quality.[71] Unfortunately, the use of vacuum tubes introduces significant image distortion which complicates quantitative analysis of these images.[72] First, the relative curvature of the output, and input phosphors on the II are often different, which causes "pincushion distortion". Second, electrons traveling through the vacuum tube are subject to external electromagnetic fields (i.e. motorized equipment, earth) causing distortion which is dependent on the orientation of the C-arm. Pincushion distortion can be corrected in a simple manner; however correction for external magnetic fields is non-trivial.[73, 74] Conversely, FPDs utilize a large solid state amorphous silicon photodiode array to detect incident radiation. This eliminates the large analogue amplification stage used in II's and with it, potential for geometric image distortion. The inherent trade-off of FPDs is increased cost of purchase, reduced flexibility for magnification modes (analogous to digital vs optical zoom in digital photography), and lower image refresh rates (for pulsed imaging). A more detailed analysis of practical trade-offs of II's and FPD's can be found in Nickoloff et al., 2001.[72]

For this study, the position dependent geometrical image distortion inherent to IIs, presented an unnecessary challenge and a FPD-based mobile C-arm was used. The device selected for use with the BGS is a Siemens Cios Fusion (Siemens) mobile C-arm with a 30x30 cm FPD (1536 x 1536 pixels).(Figure 3.2) It is a modern mid-range fluoroscopy unit well within the reach of any substantially sized medical facility. Cost of this unit ranges between $150,000-$250,000 depending on desired features. In the future, there is potential to incorporate fluoroscopy systems which use II's for wider application of the

38

BGS. A significant body of literature exists, detailing correction of II-based geometrical distortion which may be integrated with the BGS.[73-77] As costs come down on FPD systems however, it seems likely that their improved image quality and reduced physical size will sway clinician's preference towards this new technology.
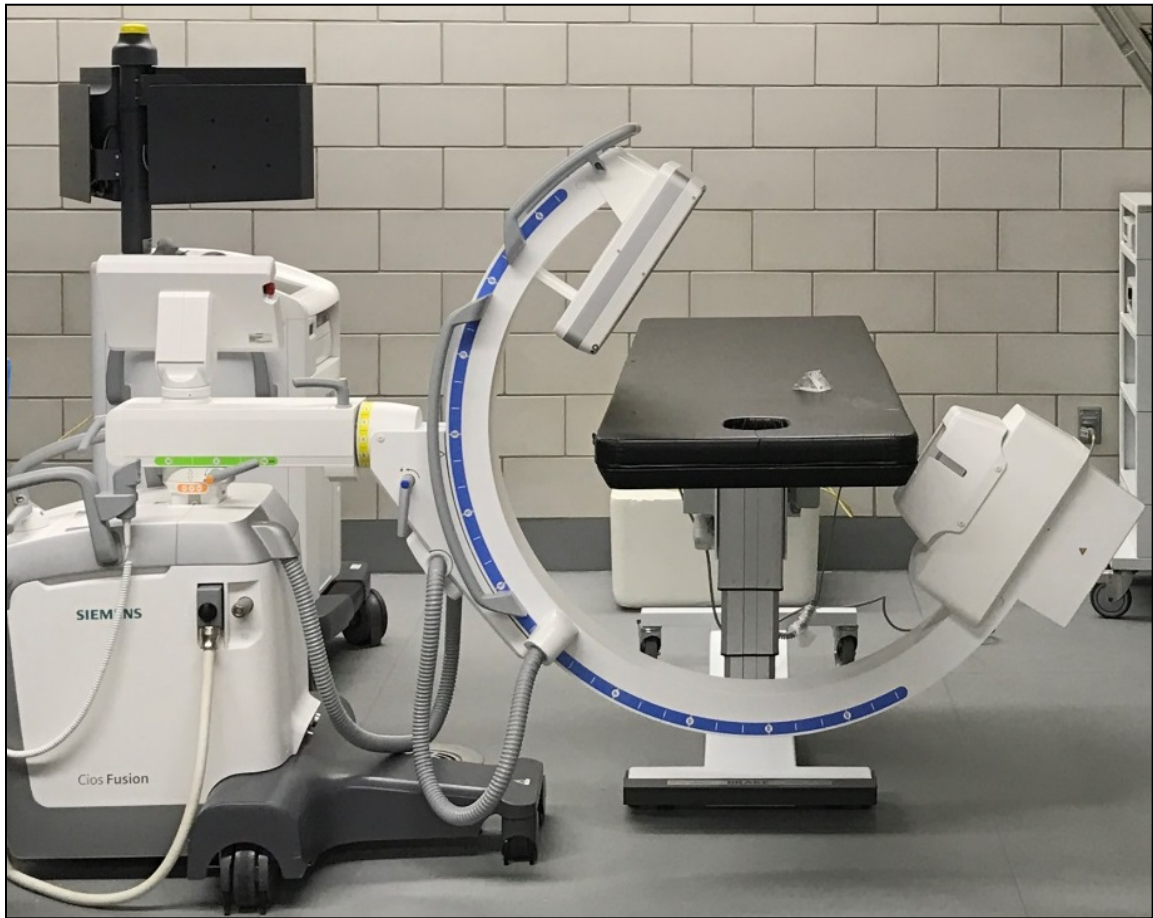
Figure 3.2: Siemens Cios Fusion fluoroscopy system used in BGS. This system has a 30x30 cm flat-panel detector which eliminates distortion common in image intensifiers.

3.1.2 FLUOROSCOPY CALIBRATION

From the perspective of an engineer, the use of C-arm fluoroscopy during surgical reduction could be described as sporadic and uncontrolled, at best. Frequent motions and adjustments of the patient and C-arm position present a significant challenge to accurate registration of bone fragments. Since the imaging hardware moves frequently and the

bone fragments are actively manipulated by the surgeon, it is necessary to define a static "world" coordinate system. For this we turn to the computer vision community and model the C-arm as a projective camera, where the action of the camera on a 3D point, X, is a 3x4 homogeneous transform, P, which maps to x, a homogeneous vector in image coordinates. To find the camera projection matrix, P, a correspondence between a set of 2D points, x, and 3D points, X is required. Full details of this algorithm are given in (Section 3.2.3), however for now it is sufficient to understand that a 3D object with radio-opaque markers at precisely known locations is necessary for performing this task.

A Haas computer numerical controlled (CNC) mill (Haas Automation, Oxnard, CA) was used to construct an acrylic frame for precisely placing 26 stainless steel ball bearings. Stainless steel bearings were selected because of their extremely precise dimensions (0.375±0.0005") and radio-opacity such that they are easily identifiable on fluoroscopy images. The geometry of the frame was selected to fit within the surgical field of view alongside patient anatomy. The object consists of a base with two orthogonal planes affixed at 45° (to the base) containing bearings. In one plane 12 bearings are placed in an "X" pattern and in the opposite 14 bearings are placed in a circle. This presents a distribution of beads where each bead is uniquely, identifiable when viewed from an AP view (orthogonal to the base, 45° to the beads) or a lateral view (parallel to the plane of the base, 45° to the beads). This configuration covers the vast majority of surgical procedures performed, however beads are not uniquely identifiable when viewed approximately parallel to their planes. This presents a degenerate case which is discussed in Section 3.4.1, however this can be easily avoided for practical surgical use, by careful placement of the object.

Although the bearing housings were placed using a precision CNC mill, the bearings were anchored with a press fit. This leaves ambiguity as to their depth in the housing, which could cause imprecision in subsequent image calibration attempts. To account for this error and provide definitive ground truth, a laser scanner was used to digitize surface points on the calibration object (FARO ScanArm® HD, FARO Technologies, UK). Manufacturer specification for this system reports accuracy on the order of ±25μm. Exposed surfaces of each bearing were targeted and digitized with the laser scanner, resulting in ~100 points per bearing. Using Geomagic Design X (3D Systems, Rock Hill, NC, USA) point-sets corresponding to individual bearings were identified and segmented. The included sphere-fitting tool within Geomagic was utilized to determine the 3D sphere center using a least squares fit. Once spheres were identified, the 3D cloud of 26 points, were transformed such that the origin is at the mid-point of spheres in the X and Y planes, and aligned with the bottom sphere in the Z plane (Figure 3.5). These 26 3D point coordinates are stored for later use.

3.1.3 WORKSTATION

A computer workstation, in proximity to the operating room with a network connection to the C-arm is required for operation of the BGS. This system serves as the nucleus for computation regarding the BGS, and is responsible for all data handling. In the current implementation that system is a mid-range desktop personal computer with specifications listed in Table 3.1. The primary consideration for this system is the presence of a CUDA (NVidia, Santa Clara, CA, USA) capable graphics processing unit (GPU). CUDA, originally an acronym for Compute Unified Device Architecture is an application programming interface (API) that allows use of a GPU as a general purpose

41

processing platform. Use of a GPU and CUDA enables the speedup of many image processing algorithms that would otherwise be prohibitively slow for clinical use.

Table 3.1: Specifications of computer workstation used for all BGS computation

BGS Workstation Specifications	
Processor	Intel Core i5 3570k (3.2 GHz)
Memory	32 GB
Graphics Processor	NVidia GTX Titan Black (6 GB)
Software	Windows 7 Enterprise 64-bit
	MATLAB 2014b
	BGS Software
	CUDA v8.0
	Geomagic Design X

3.2 FRAGMENT POSE ESTIMATION

3.2.1 COMPUTATIONAL FRAMEWORK

A computational framework has been developed that models relevant components of the fracture reduction during surgical reduction. Each of these components (i.e. virtual C-arm, CT volume and virtual bone fragment) is treated as a rigid body, with a well-defined local coordinate system, related to the world coordinate system through rigid transformation. (Figure 3.3) This creates a hierarchical system of transformations such that the position of all objects is known regardless of reference frame.[25]
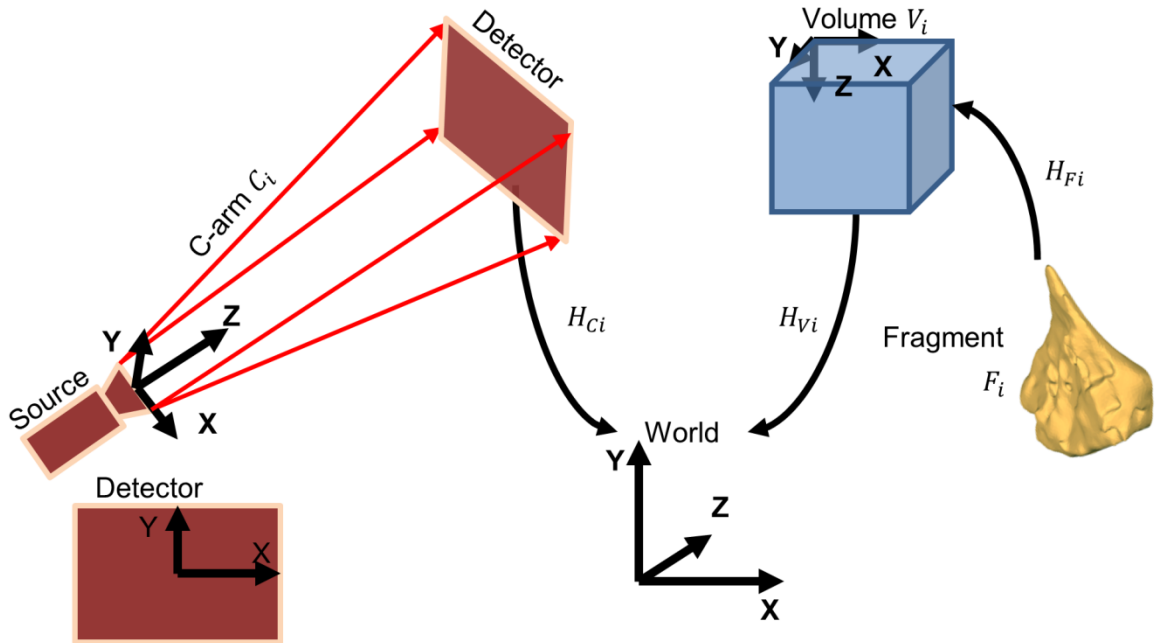
Figure 3.3: Schematic of intra-operative pose estimation framework, shows relationships between three main components of computational system.

A particular issue of importance within this framework is the representation of rigid transformations. In an ideal situation, it is desirable for a given transform, H, to be unique, compact, computationally efficient, intuitive and singularity-free. Euler angles while easy to comprehend were determined to be too computationally expensive and unstable due to their susceptibility to instability ("Gimbal Lock") in specific configurations.[78] Another approach explored, 4x4 homogeneous transform matrices were excluded because they are susceptible to numerical error and require computationally expensive renormalization.[79] They also use 12 parameters to describe a 6 DOF transformation, increasing the complexity of optimization methods. Finally, dual quaternions were selected as the appropriate method for representation of rigid transformation as they are compact (8 parameters vs 12), efficient to normalize, singularity-free and relatively intuitive to work with.[78] A brief description is listed in Appendix A.

43

3.2.1.1 VIRTUAL C-ARM

As the name implies, virtual C-arms, C_i, contain information about the intrinsic and external parameters of an individual C-arm imaging device. This includes detector resolution, pixel spacing, principal point, source-intensifier distance (SID) and spatial orientation. Detector resolution is defined as an integer vector $\langle i, j \rangle$ representing the number of pixels in both dimensions of the detector grid. Pixel spacing is defined as the physical dimension of an individual detector element in mm. This is represented by a real number vector $\langle s_i, s_j \rangle$ indicating the size of pixels both dimensions of the detector. In the case of an FPD C-arm it is assumed that pixels are isotropic and, $s_i = s_j$. Principal point is defined as a point on the detector plane, which is the shortest distance to the camera center (lies on a line intersecting with the focal point, and orthogonal to the detector plane). Source intensifier distance, is define as the Euclidean distance from the camera center, to the principal point. The spatial orientation of the C-arm is defined as the rigid transform mapping points defined in the local coordinate system, to the world coordinate system. This is represented by a dual quaternion, H_{Ci}, and is determined by the camera calibration algorithm detailed in Section 3.2.3. Although the focal point of the X-ray tube has a finite dimension (~0.5 mm) its size is assumed to be negligible compared to the SID of the C-arm (~1020 mm). This pinhole camera model is particularly appropriate for a FPD C-arm system because of the lack of distortion from a lens (optical camera) or II (fluoroscopy).

The local coordinate system of the virtual C-arm is defined such that the focal point of the X-ray tube is located at the origin. The detector lies within the XY plane and is offset along the Z-axis according the source intensifier distance of the imaging system.

44

Ideally, the center of the detector plane is coincident with the Z-axis however in realistic scenarios it may be offset to account for geometric imperfections.

3.2.1.2 VIRTUAL BONE FRAGMENT

Virtual bone fragments, F_i, represent individual units of fractured bone or a whole bone, if no fracture is present. It is assumed that all motion of a F_i is related under a single rigid transform. Information contained within a virtual fragment, includes geometry, bone density, X-ray attenuation, cartilage representation (if any) and spatial orientation. Geometry, bone density and X-ray attenuation are determined from CT segmentation, and are represented by triangular surface mesh (STL) or a voxel grid, $V_{F_i}(i, j, k)$ computed during pre-processing (Section 3.2.2). Cartilage representation is utilized for subsequent biomechanical modeling of the reduction and is determined by extrapolation from CT data, CT arthrogram, or MRI data (Section 3.3). The spatial orientation of the virtual fragment defined as the rigid transform mapping its local coordinate system, to the CT Volume coordinate system. This is represented by a dual quaternion, H_{Fi}^V. The location of a single fragment F_i relative to reference object is H_{Fi}, where $H_{Fi} = H_{Fi}^V * H_V$. The transform H_{Fi}^V is determined using a 2D-3D registration algorithm detailed in Section 3.2.4.

The local coordinate system of a bone fragment is defined in terms of its original CT volume. A bounding box, aligned with the CT image axes, is placed around individual fragment segmentations. The corner of the box closest to the CT origin, corresponds to the fragment origin and the X, Y, Z axes of the CT are translated to the fragment.

45

3.2.1.3 TRANSFORMATION

Using this simple hierarchical framework, the spatial orientation of a C-arm, bone fragment or any related object, can be computed from the desired frame of reference. For example, the orientation of a ray, r, computed in the local coordinate system of a C-arm, could easily be transformed to the local coordinate system of a bone fragment, F_i, where $r^{Fi} = H_{Fi}^{V}{}^{-1} * H_V{}^{-1} * H_{Ci} * r$.

The task of determining the 3D geometry of a fracture reduction now becomes synonymous with the task of finding, H_{Fi}^{V}, for each individual bone fragment.

3.2.2 PRE-PROCESSING

Appropriate and accurate data are required for creation of the aforementioned computational model. Bone fragments, $F_{1:n}$, require a model for 3D x-ray attenuation, 3D surface geometry, and position relative to their adjacent fragments. These data are obtained from pre-operative CT scans as they are routinely acquired days before definitive surgical intervention for difficult IAFs. When properly calibrated, CT voxels provide a density map of the fracture pattern, allowing for modeling fragment geometry, locality, and x-ray attenuation. In the case of fracture reduction, where independent bone fragments are manipulated, image segmentation is performed to separate individual fragments from their surrounding soft tissue and adjacent bone.

3.2.2.1 IMAGE SEGMENTATION

Segmentation of individual fragments is performed using a semi-automated process, designed to minimize required user input while accommodating manual-intervention for idiosyncratic fracture patterns. While the segmentation routine detailed here has served for this application, it was not the focus of this work. A multitude of alternative

46

segmentation techniques could also be utilized to great effect. This section provides a brief overview of the methodology used.

An automated segmentation is performed which uses a simple intensity threshold at conservative image intensity value to separate soft tissue from bone. Cortical bone regions are identified by a second more aggressive intensity threshold, which then serve as markers for marker-based watershed segmentation. This pre-segmentation process serves to provide a preliminary separation of bone from soft-tissue, and individual bone fragments. However, it is well-known that watershed segmentation is biased towards over-segmentation.[80]

To ameliorate the effects of over-segmentation, iterative region merging is performed. First, a region adjacency graph (RAG) is constructed such that each unique region label corresponds to a node on the graph. Connectivity of the graph is determined by identifying adjacent regions in the segmented image. Any region with four or more voxels in contact with another bone region is defined as adjacent, and an edge is constructed between their corresponding nodes.[81] Edges are assigned weights according to the strength of connectivity between these two regions. Properties such as relative image-intensity, image gradient, and size of the interface between the regions (relative to the total region volume) are used to determine this strength.

After construction, nodes on the RAG are iteratively merged to reduce the number of over segmented bone regions. Merging is performed in a naïve manner such that nodes with the highest strength of connectivity are merged first, and then surrounding connectivity costs are recomputed. A user-defined strength of connectivity threshold is used as a termination point for this algorithm. Although this process has been shown to

47

perform well empirically, it fails to completely resolve the over segmentation problem and will merge some regions which correspond to separate bone fragments.

Remaining errors in the segmentation are corrected using a user-guided region editing process. A graphical user interface (GUI) with a 3D model of the current segmentation is presented to the user.[82] Individual fragments can be selected and edited with three functions: delete, merge, and separate. The delete function removes the selected region(s) from the current segmentation. Merge combines selected regions into a single region. Separate attempts to divide the selected region into multiple smaller regions. This function opens a secondary GUI where the user applies new labels to voxels within the selected region, and a graph-cut is performed to find the minimum cost division between each of these new regions.[83-86] Iterative application of each of these three functions allows the user to obtain 3D segmentation of complete individual bone fragments. On occasion errors in the earlier automated steps prohibit achievement of an ideal segmentation. In attempt to counter this, the final editing step utilized is manual segmentation of individual voxels, to remove residual errors. This segmentation process attempts to minimize user-time and the tedious tracing of individual voxels, while providing an accurate and flexible segmentation framework. The output of this process is a label volume, $L(i, j, k)$ of identical dimension to the input CT volume but with integer values according to their segmentation label, where a 0 value corresponds to background and 1…n correspond to the region of interest (ROI) of fragments 1 through n.

3.2.2.2 FRAGMENT PRE-PROCESSING

Once the pre-operative CT image segmentation is complete, each fragment is separated into its own individual volume for subsequent independent manipulation. The

48

ROI for each fragment label (from label volume $L(i, j, k)$) is identified by computing the minimum and maximum coordinate in the $\langle i, j, k \rangle$ volume dimensions (i.e. $\min_{F_i}^i$ and $\max_{F_i}^i$ represent the minimum and maximum extent of fragment F_i in the i dimension of the CT). The fragments sub-volume, V_{F_i}, is defined as subset of the full CT volume, V, contained within the bounds of that fragments label.

$$V_{F_i} = V(min_{F_i}^i \ldots max_{F_i}^i, min_{F_i}^j \ldots max_{F_i}^j, min_{F_i}^k \ldots max_{F_i}^k)$$

The origin of the sub-volume is located at $(\min_{F_i}^i, \min_{F_i}^j, \min_{F_i}^k)$ within the larger CT volume. As it is possible for multiple sub-volumes to overlap, background information is masked such that:

$$V_{F_i}(i, j, k) \begin{cases} V\left(min_{F_i}^i + i, min_{F_i}^j + j, min_{F_i}^k + k\right), & L(i, j, k) = i \\ 0, & L(i, j, k) \neq i \end{cases}$$

The surface geometry of the fragment within each sub-volume is identified by iso-surfacing the segmentation. This generates a triangulated surface model, which is used for visualization (Section 3.2.5) and contact stress assessment (Section 3.3).

For generation of synthetic fluoroscopy images it is more convenient to treat bone density as linear attenuation coefficients (cm⁻¹), which correspond to the apparent x-ray absorption at a given beam energy. This conversion is performed from data presented by Brown et al. 2008.[87]

3.2.3 FLUOROSCOPY CALIBRATION

Due to the frequent movements and adjustments of a mobile C-arm over the course of a fracture reduction, it is necessary to continuously monitor its position. While other

49

studies have utilized external mechanisms (optical tracking or an instrumented C-arm), we have opted for using an internal calibration. The positioning of the device is determined using measurements taken directly from the clinical images. Effectively this process solves for the transform from the virtual C-arm to the reference coordinate system (H_{Ci}). (Figure 3.4)
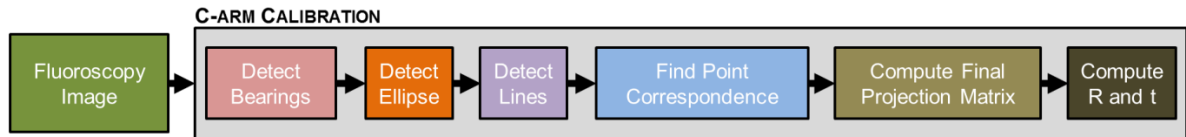
Figure 3.4: Overview of C-arm calibration process begins with a C-arm fluoroscopy image of the calibration object. The location of individual bearings are detected, and then bearings which belong to the ellipse and lines are found. These are used to compute 2D-3D point correspondences, and then to compute a projection matrix. The projection matrix can be decomposed to estimate the external rotation and translation of the C-arm.

The fluoroscopy system is modeled as a projective camera with pinhole geometry. This is essentially a linear transform (P) which maps three dimensional homogeneous coordinates, X, to points, x, which lie on a two dimensional projective plane.[88]

$$x = PX$$

The projective transform, P, can be further decomposed using QR decomposition to identify specific, physically meaningful properties of the camera.[88, 89]

$$P = K[R|t]$$

P is a 3x4 projective transform, K, are the intrinsic camera parameters, R, is the external rotation of the camera, and t is the external translation of the camera. The intrinsic parameters of the camera, K, can be further broken into meaningful values.

$$K = \begin{bmatrix} a_x & s & x_o \\ & a_y & y_o \\ & & 1 \end{bmatrix}$$

50

Where a_x and a_y represent the size and aspect ratio of the x and y pixels, x_o and y_o represent the offset of the principal point on the projective plane and s represents the aspect ratio of the pixels. Further, if the detector elements are isotropic (which they are) it is expected that $s = 0$ and $a_x = a_y$. Focal length of the camera is represented by the ratio of the source-intensifier distance (SID), and the pixel width a_x. On a FPD fluoroscopy system it is expected that this parameters remain largely unchanged (assuming strain of the C-arm gantry is negligible) throughout the course of the operation. Thus, once the intrinsic parameter matrix, K, is known, it is unnecessary to be recomputed.

The projective transform, P, is solved using the gold-standard algorithm presented by Hartley and Zisserman, using correspondences between known 3D coordinates and image points. In short, this algorithm normalizes input 2D points $\tilde{x} = Tx$, and 3D points $\tilde{X} = UX$ to ensure numerical stability, where T, and U are similarity transforms. A direct linear transform (DLT) is used to compute an estimate of camera projection matrix, $\tilde{P}$. The estimate of $\tilde{P}$ is then refined by minimizing geometric re-projection error.[88, 90]

$$\sum_i \|x_i, PX_i\|$$

Finally $\tilde{P}$ is de-normalized to find the final estimate of the camera projection matrix. In general this algorithm works well, however if intrinsic parameters of the camera are known, it can be further refined using the restricted camera estimation algorithm from the same authors. This is an iterative optimization, which begins with a preliminary estimate of the camera projection matrix, P, and known properties of the intrinsic parameter matrix. In the case of an FPD C-arm the skew of the pixels is known to be 0, therefore

51

$s = 0$ and $a_x = a_y$. The principal point is known to be at the center of the detector $x_o = y_o = 0.5$ in normalized coordinates for the image domain (range 0-1). These known features are introduced as soft constraints to the geometric error cost function where ω is the weight. These values are slowly drawn to their known values by increasing ω as the optimization progresses.

$$\sum_i \|x_i, PX_i\| + \omega s^2 + \omega(a_x - a_y)^2 + \omega(x_0 - 0.5)^2 + \omega(y_0 - 0.5)^2$$

To solve for P, a set of known point correspondences between image and world are required. The calibration object (Section 3.1.2) is the critical component for this process, as the 3D coordinates of the points are precisely known from laser scanning, and the image coordinates of the points can be determined automatically.

The ball bearings embedded within the calibration object, present a well-defined circle when imaged radiographically. The precise location of these circles on the image, are identified with a circular Hough transform. Once the image coordinates of these circles are identified, it is necessary to determine each circles correspondence to a 3D point. A naïve brute force method for pairing 26 bearings requires testing 26! combinations and is intractable. Instead their known geometrical arrangement is leveraged as a means of reducing the possible number of solutions. As described in Section 3.1.2, the bearings are arranged in two lines (6 bearings each) and one circle (14 bearings). Under projective geometry, it is known that a line projects to a line, and a circle maps to an ellipse (include line and circle as a special case of the ellipse)[88]. Detection of these 2D primitives on the fluoroscopy image is based upon a random sample consensus (RANSAC) algorithm.[91]

In short, the RANSCAC algorithm fits model data to a set of observations in an iterative manner that is robust to outliers. A model is fit to a randomly sampled subset of data on every iteration of the algorithm. This tentative model is tested against the full dataset and points within an error value (ε) of the model are reported as inliers. The number of inliers is recorded and upon completion of the algorithm, the model with the highest number of inliers (one which has reached a "consensus") is selected. This RANSAC method has been applied in many disciplines with a multitude of variations to improve its speed and robustness.[92] In this application, the RANSAC algorithm is used to find both line and ellipse geometries formed by bearings on the 2D fluoroscopy images.
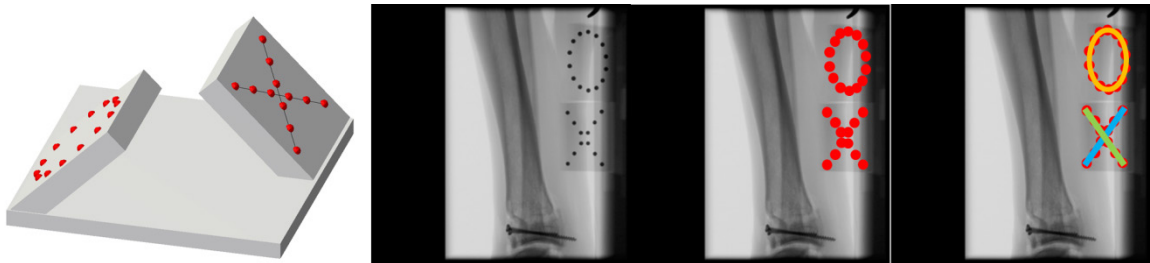
Figure 3.5: Calibration object (left) consists of 26 steel bearings fixed in an acrylic shell. Beads are detected on fluoroscopy image of calibration object (middle right). Ellipse and lines are fit to these detected beads through the use of a RANSAC algorithm (right).

The ellipse is detected first as it contains the largest number of beads (14 vs 6) when compared to the lines. Ellipses are fit in a least squares manner, according to the method presented by Halii and Flusser, 1998 using randomly sampled subsets of 4 beads.[93] This algorithm performs 1000 iterations but if any model is found to have 12 inliers (2 fewer than the total number of beads) the iterations are terminated. Once a consensus set is found, the model is re-fit to all points within the set. Upon completion of ellipse detection, all ellipse inliers are removed from the set of bearings and lines are detected.

Lines are detected in a similar manner to the ellipses. A line is fit to a randomly sampled subset of two bearings. Iterations are performed until they reach the specified maximum of 1000 or a model is found with 6 inliers. The line is re-fit in a least squares manner to the total set of inliers once a consensus set is found. Since there are two lines present in the calibration object, upon detection of the first line, the inliers are removed from the total set and line detection is repeated.

Once the bearing points are partitioned as ellipse or line inliers further information still remains to be extracted. Ordering of points along these primitives is also preserved under projection.[88] Accordingly, points on the lines and ellipses are sorted in linear or polar coordinates, respectively.

The task of categorizing and sorting the 2D bearings has now substantially reduced the number of possible pairings between 2D and 3D point sets. Assuming all bearings have been properly detected and categorized in the lines, there are only four possible permutations. Similarly for the ellipse there are 28 possible permutations (14 rotations and 1 mirroring). Combining these leaves the possibility of 112 permutations of pairings, which could easily be computed in a brute-force method. The brute-force method fails however, once bearings are not detected, or are incorrectly categorized. As such the RANSAC method is used again to find camera model, P, which best fits the input set of pairings.

In this algorithm a candidate set of 26 pairings is computed based on bead categorization and ordering (2D lines can only be paired to 3D lines, ellipse points can only be paired to ellipse points, etc.), 11 of these pairings are selected randomly. The previously discussed gold-standard calibration algorithm from Hartley and Zisserman is

54

used to compute P from this candidate point set. The full set of 3D points is then projected onto the projection plane using this candidate P. Two-dimensional distance between the projection points and detected location of the bearings is used to determine the number of inliers. If a candidate projection model, P, is found to have 24 inliers then it is selected as the correct model, and pairings are re-selected according to re-projection distance. This set of paired coordinates is then used to compute the final camera model with the method previously described. Ultimately, this provides the rigid transformation which describes the orientation of the C-arm relative to the calibration object. Pseudo code for these algorithms is outlined in Appendix B.

3.2.4 2D-3D REGISTRATION

The second and perhaps most important synchronization in the biomechanical guidance system, is determination of bone fragment pose from calibrated fluoroscopy images. This is performed through 2D-3D registration, which matches computer generated radiographic images, called digitally reconstructed radiographs (DRRs), to intra-operative fluoroscopy images, by varying the positioning of virtual bone fragments. (Figure 3.6)
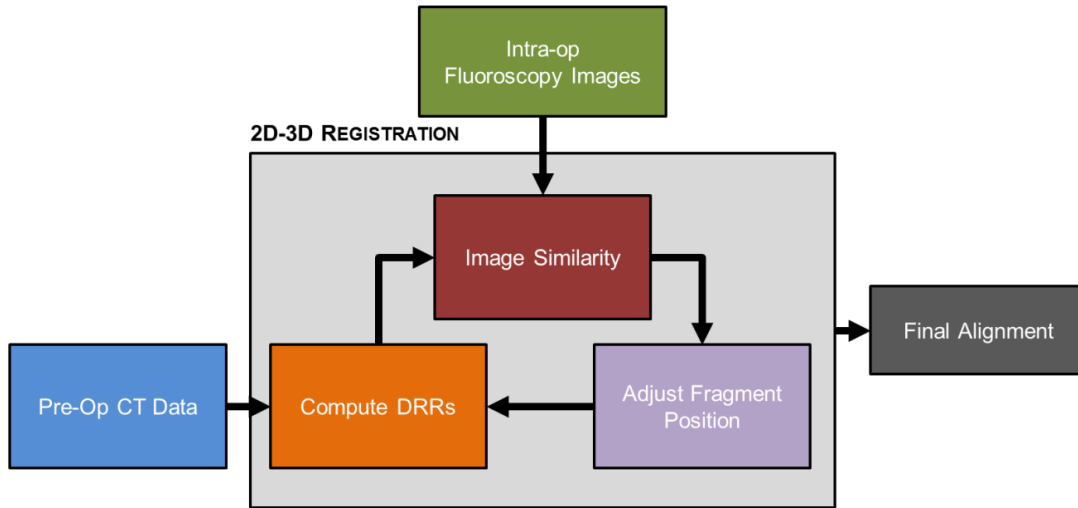
Figure 3.6: 2D-3D registration operates by computing DRRs of fragments with the computer model (orange). DRRs are compared to intra-operative fluoroscopy images by computing image similarity comparison (red). Optimization adjusts the positioning of bone fragments in attempt to maximize the similarity between DRRs and fluoroscopy images (lavender).

3.2.4.1 DRR GENERATION

Digitally reconstructed radiographs (DRRs) are a simulation of projective x-ray images. The fundamental process modeled when computing a DRR is the attenuation of ionizing radiation, along the path the source to each detector element. Efforts have been made to develop DRRs of high fidelity that very closely simulate X-ray behavior.[94] DRR generation for 2D-3D registration typically emphasizes computational speed over image quality and uses a simple approximation of the image formation process.

Assuming an effective monoenergetic radiation source, the apparent brightness of any pixel is a function of the path length of the beam, the x-ray attenuation along the path of the beam, and error from scattering of photons. If scattering effects are assumed to be negligible (supported by use of a detector grid), the intensity of an individual pixel on the image detector can be modeled by:[71]

$$I = I_o exp^{-\int_s^D \mu(x)dx}$$

56

Where I is the apparent X-ray intensity at the corresponding voxel, I_o is the initial source intensity, and μ is the attenuation co-efficient at the effective beam energy along the path from source to detector.

Although it is difficult to know the exact x-ray attenuation along a given source to detector path, the voxel grid of a virtual fracture fragment ($V_{F_i}(i, j, k)$) serves as a reasonable approximation. When applied to a discrete grid, the previous equation can be approximated:

$$I = I_o exp^{\Sigma - \mu(i,j,k)x(i,j,k)}$$

where $\mu(i, j, k)$, is the attenuation coefficient of voxel at (i, j, k) and $x(i, j, k)$ is the path length of ray intersection with that voxel.[95] This is applied over the domain of an entire image detector ((x,y) pixel indices).

$$I(x, y) = I_o(x, y) exp^{\Sigma - \mu(i,j,k)x(i,j,k)}$$

The attenuation along any given path from the source to the detector is clearly a function of the position of the bone fragment, relative to the C-arm. From Section 3.2.1 the position the C-arm relative to the virtual bone fragment can be found by $H = {H_{Fi}^V}^{-1} * {H_V}^{-1} * H_{Ci}$. Image intensity is a function H, the relative positioning of the C-arm and the bone fragment.

$$I(x, y, H) = I_o(x, y) exp^{\Sigma - \mu(i,j,k)x(i,j,k)}$$

Algorithms have been developed which offer exact solutions to this ray traversal problem over a uniform voxel grid.[96, 97] Although these offer reasonable algorithmic

complexity and computational performance, there is evidence that even faster solutions can be used with little to no detriment to registration accuracy.[25]

Instead a tri-linear sampling approach is used, where the ray is sampled at a fixed distance interval (Δx) over the total length of intersection with the volume. (Figure 3.7) Tri-linear interpolation of nearby voxels is performed at each sample point to approximate the intensity of the image.

$$I(x, y, H) = I_o(x, y)exp^{\Sigma - \mu(i,j,k)\Delta x}$$
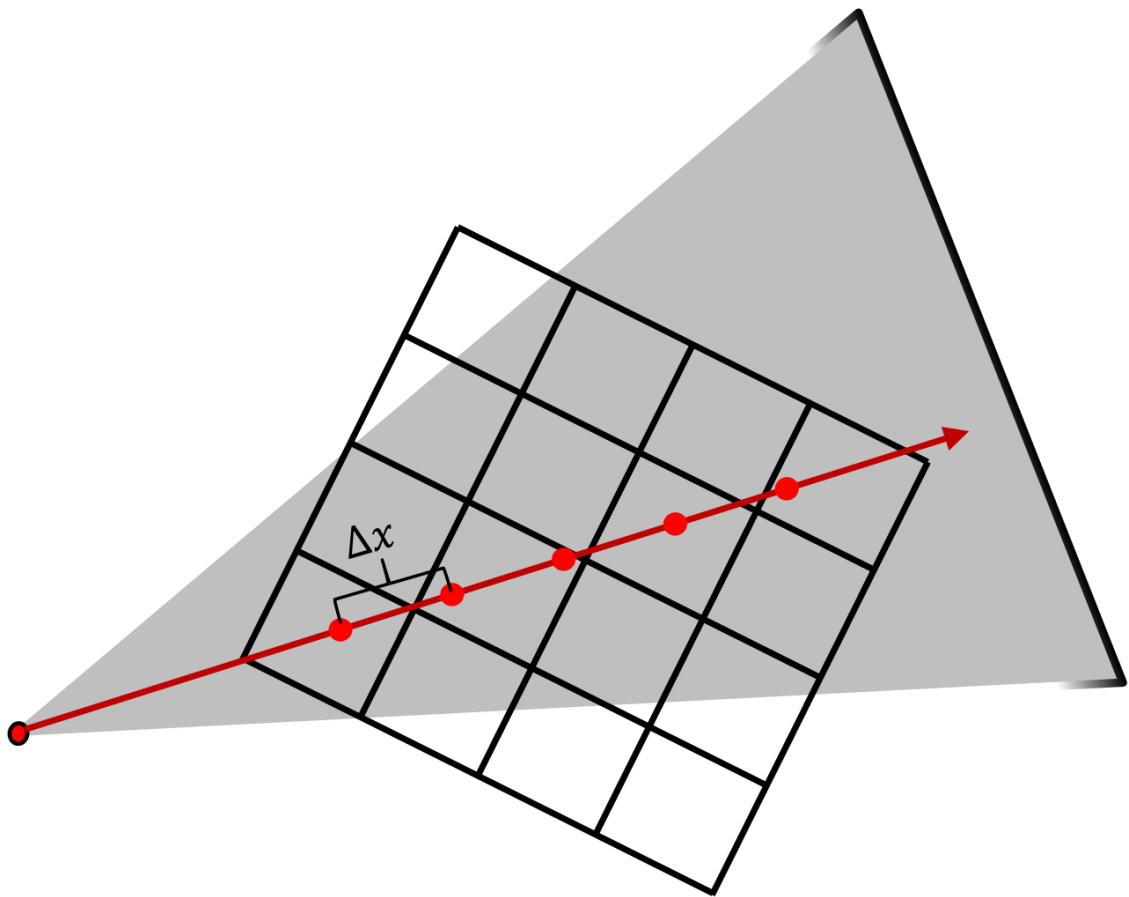
Figure 3.7: Trilinear sampling computes DRR by sampling the voxel grid at uniform step-sizes (Δx).

It is unrealistic to expect a DRR of a single bone fragment to effectively match an intra-operative fluoroscopy image. The intra-op image contains attenuation of multiple

bone fragments, soft-tissue, surgical hardware, image noise, and other extraneous material.[27] From Haque et al. 2013, the concept of the multi-bone DRR (MDRR) (Figure 3.8) is used where an MDRR contains attenuation from multiple overlapping bone fragments:

$$I(x,y,H)_{MDRR} = I_o(x,y)exp^{-\sum \mu(fragment\ 1)\Delta x + \mu(fragment\ 2)\Delta x + \cdots \mu(fragment\ n)\Delta x}$$
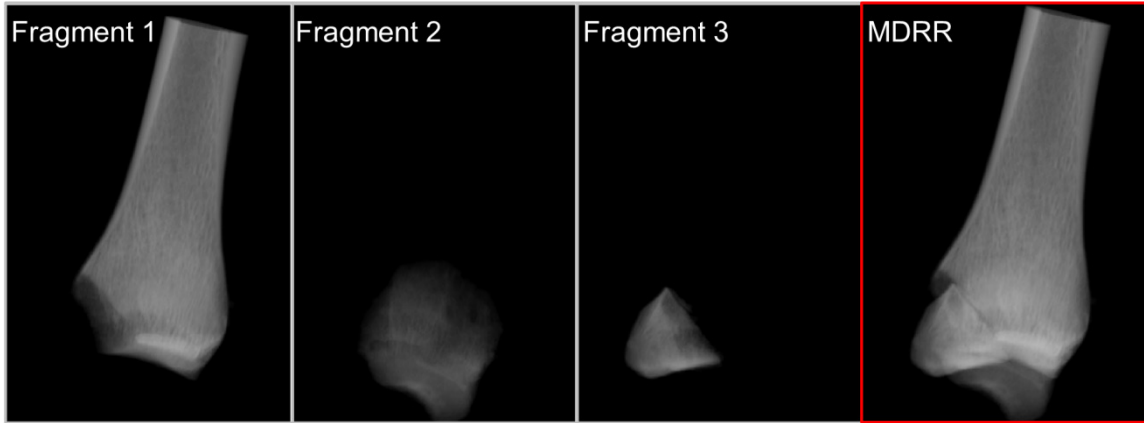
Figure 3.8: Generation of MDRRs uses multiple bone fragment DRRs to generate a final composite image.

3.2.4.2 IMAGE COMPARISON

Once DRRs of a bone fracture have been obtained, an image similarity metric is used to quantify matching between a DRR image and its corresponding fluoroscopy image. This similarity value serves as the merit function for the subsequent optimization of fragment position. As such it must be smooth, relatively free of local minima, robust to noise and rapid to compute. Image comparison in the BGS uses multiple-scales and multiple views simultaneously in attempt to find a robust comparison between the DRR image, I_{drr}, and the reference fluoroscopy image, I_{ref}. (Figure 3.9) "Scale" of the images is controlled through the use of Gaussian smoothing, with smoothing kernel:

$$G(x,y,\sigma) = \frac{1}{2\pi\sigma^2}e^{-\frac{x^2+y^2}{2\sigma^2}}$$

59

The kernel is convolved with the image I, where σ represents the standard deviation of the distribution.

$$I^{Gauss} = G(x, y, \sigma) * I(x, y)$$

Then, borrowing from the concept of scale-space filtering, σ is varied, to adjust the scale of the comparison which is performed.[92, 98]

Since DRR images in the BGS model only bone fragments, it is unexpected for the similarity between I_{drr}, and I_{ref} to be valid over their entire domain. In practice, only DRR regions which contain non-zero data are utilized in the comparison. This new domain, s, is used for all subsequent image comparison, where $s = \{(x, y) : I_{drr}^{Gauss}(x, y) > 0\}$. Normalized cross correlation (NCC) is then used to compare the DRR and fluoroscopy image over the domain s:

$$NCC_{Gauss} = \frac{1}{n} \sum_{i=0}^{n} \frac{\left(I_{drr}^{Gauss}(i) - \mu_{drr}\right) \left(I_{ref}^{Gauss}(i) - \mu_{ref}\right)}{\sigma_{drr} \sigma_{ref}}$$

Where $\{i \dots n\}$ represent all values in s, μ represents the mean of the image in domain s and σ represents the standard deviation of the image in s. While correlation of image intensity works well in general, image gradients are also useful for robust image comparison metrics.[99] Partial derivatives of the Gaussian smoothed images are also computed.

$$I^{Dx}(x, y) = \frac{I^{Gauss}(x,y)}{dx} \qquad\qquad I^{Dy}(x, y) = \frac{I^{Gauss}(x,y)}{dy}$$

Similarly to NCC_{Gauss} the NCC of the gradient images, NCC_{Dx} and NCC_{Dy}, are over domain s.

60
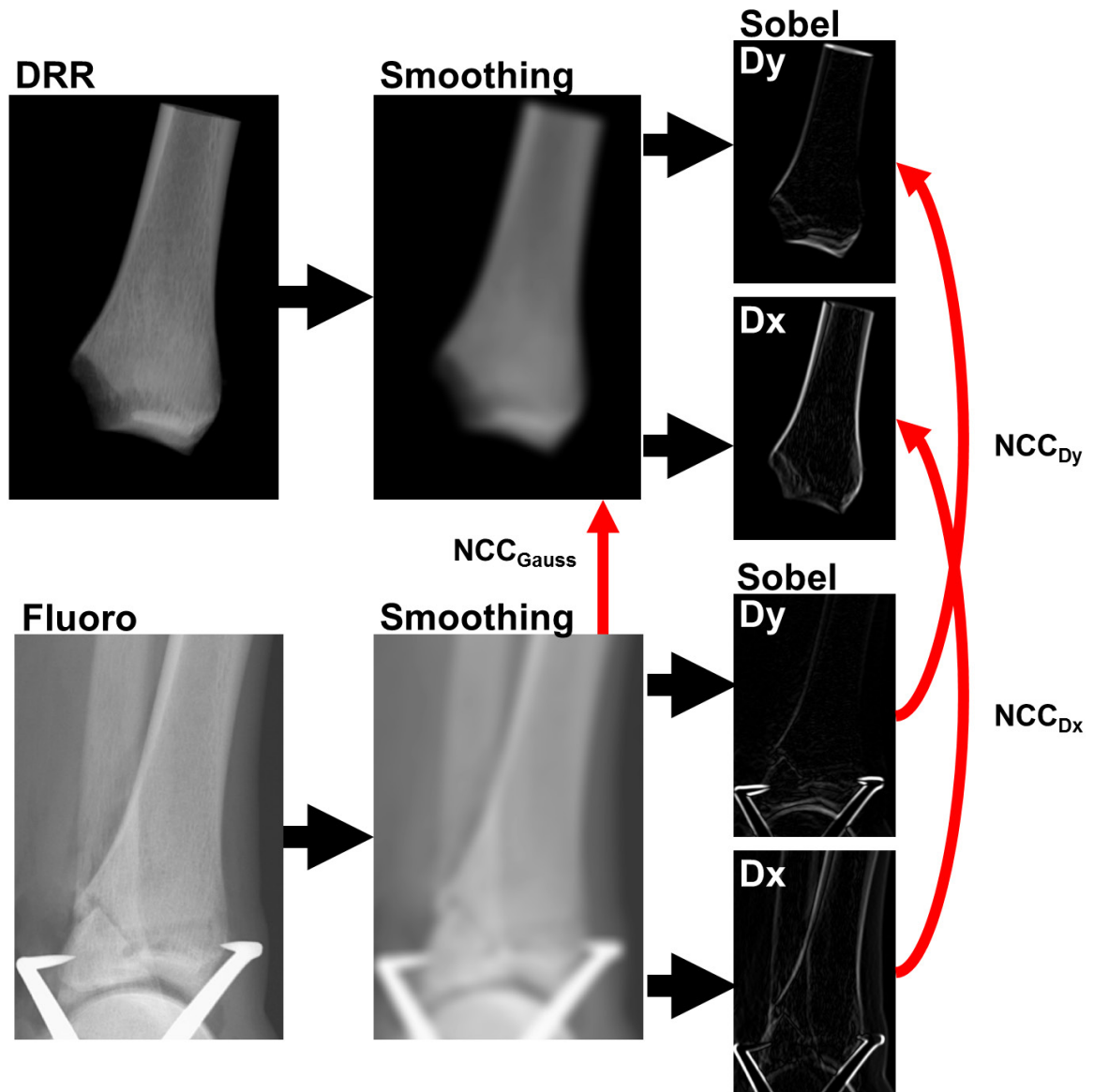
Figure 3.9: Similarity between a DRR image (top) and reference fluoroscopy image (bottom) is computed performed with three correlations. Correlation between Gaussian smoothed images (center), and their partial derivatives (right) are used. Correlation is computed only on the region on which the DRR image contains information (non-zero values).

These three correlations are then combined into a final similarity metric:

$$Similarity = \frac{NCC_{Dx} + NCC_{Dy}}{2} NCC_{Gauss}$$

61

The BGS uses multiple images simultaneously, and similarity is computed for each image (Figure 3.10). Similarity values for single imaging views are combined by computing the product of the similarity for n fluoroscopy images:

$$Similarity = \prod_{i=0}^{n} Similarity_i$$
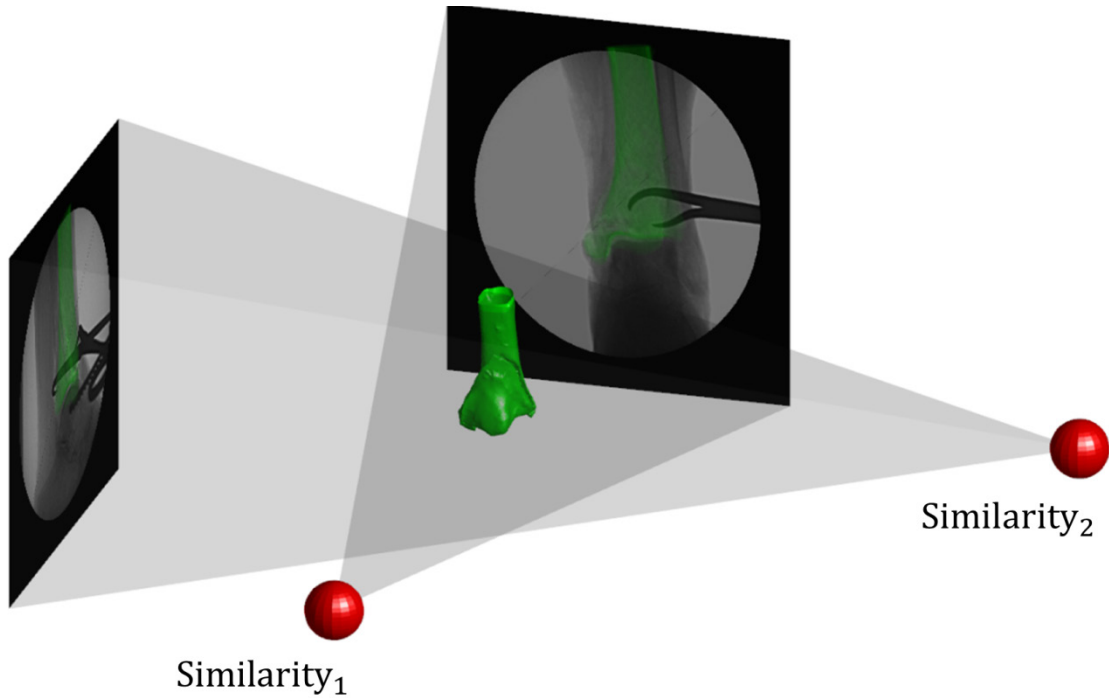
Figure 3.10: Similarity is computed on multiple views simultaneously and the product of all similarities are used.

DRRs, as discussed in the previous section are a function of the relative position of the C-arm and bone fragment. Accordingly, the image similarity is a function of both scale and fragment orientation such that:

$$Similarity(\sigma, H) = \prod_{i=0}^{n} Similarity_i(\sigma, H)$$

Where σ represents the Gaussian smoothing scale, and H represents the relative orientation the bone fragments to the C-arm. In cases which use multiple (n) views and multiple (m) fragments a unique transform is required for every fragment-to-C-arm pairing. Therefore H can be presented as:

$$\begin{bmatrix} H_{C_1}^{F_1} & \cdots & H_{C_1}^{F_m} \\ \vdots & \ddots & \vdots \\ H_{C_n}^{F_1} & \cdots & H_{C_n}^{F_m} \end{bmatrix}$$

Where each element of H, $H_{C_j}^{F_i}$, represents the transformation from C-arm j to fragment i. Of course in typical usage, this is simplified if only fragment is manipulated, and the C-arms are considered to be static.

3.2.4.3 OPTIMIZATION

To achieve an optimal matching between DRR images and fluoroscopy images the positions of bone fragments are varied *in silico* until the similarity between the two systems is maximized. A hierarchical optimization scheme has been developed to perform robust, automated registration of bone fragments. This seeks to maximize the similarity function at a set of defined fixed scales:

$$\underset{H}{\mathrm{argmax}} \ \ Similarity(\sigma, H)$$

In this case the initial position of the fragment H_0, is determined by prior manual registration, or automated registration steps. In attempt to improve the capture region of the optimization, a multi-start strategy was used where H_0, was perturbed by a fixed offset of $\pm\Delta mm/rad$ in each translation and rotational degree of freedom. (Figure 3.11) In translation the offset was set to the scaling value ($\Delta = \sigma\ mm$) and in rotation the

63

offset was set to $\Delta = \sigma/20$ rad. For each scale, these twelve offsets are applied to independent optimizations:

$$
\begin{bmatrix}
\Delta & 0 & 0 & 0 & 0 & 0 \\
-\Delta & 0 & 0 & 0 & 0 & 0 \\
0 & \Delta & 0 & 0 & 0 & 0 \\
& & & \vdots & & \\
0 & 0 & 0 & 0 & 0 & -\Delta
\end{bmatrix}
$$

The final transform, H, is selected as the maximum similarity from all 12 starting positions.

$$
\max_{H,\ i = 0\dots11} \quad \underset{H}{\text{argmax}} \quad Similarity(\sigma, H + offset_i)
$$

A local optimization may also be performed which does not use the multi-start strategy. This is performed in three possible ways, first is with optimization on the full transformation (x,y,z translation and rotation), the next two are over half of the transformation where the fragment is limited to pure translation or rotation. While the latter two methods are not used in automated alignment, they have proven useful when the user performs manual manipulation or adjustment of fragments. These are offered as options on the graphical user interface. (Section 3.2.5.1)

Figure 3.11: Graphical representation of the multi-start optimization strategy shown on a medial articular fragment (green). Translations from the initial start point are shown, while rotations are not displayed.

64

While a wide variety of different optimization algorithms have been used in 2D-3D registration, bound-optimization by quadratic approximation (BOBYQA) and Nelder Mead downhill-simplex (Simplex), have been selected for computational speed and convergence properties.[25, 100, 101] These are derivative-free optimization techniques, chosen because the gradient of the similarity function cannot be computed analytically and is too expensive to compute numerically. BOBYQA, is a trust-region optimization algorithm which approximates a quadratic model of the cost function through interpolation of a population of sample points. It has been shown to have excellent performance in wide array of optimization problems extending to tens or hundreds of dimensions.[100] Downhill-Simplex samples an n-dimensional cost function by forming an n+1 polytope (simplex) distributed about an initial estimate. A set of rules is then used to reflect, expand or contract this simplex within the space of the cost function.[101-103] When viewed graphically, the simplex appears to be crawling across the space similarly to an amoeba on a culture dish, leading to its common nick-name as the "amoeba" algorithm.

The overall optimization strategy uses two multi-start steps large and small scale, computed with BOBYQA, this is followed by a local 6 DOF optimization performed by downhill simplex. (Figure 3.12)

65
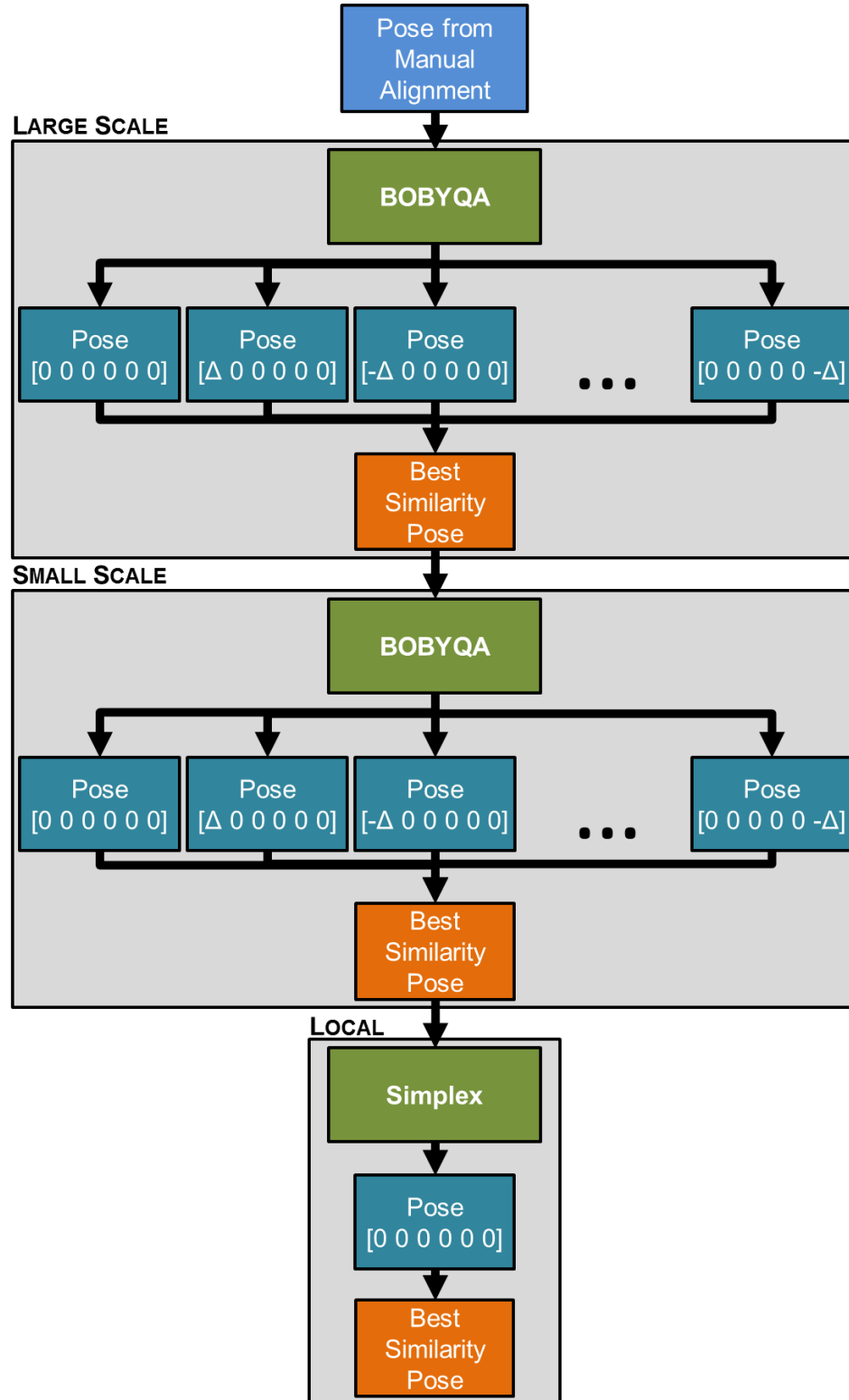
Figure 3.12: Multi-scale optimization strategy begins with a large-scale multi-start optimization performed with BOBYQA from 12 different initial positions. This is followed by a small scale multi-start optimization and a subsequent local optimization performed with a downhill simplex algorithm.

66

3.2.5 IMPLEMENTATION AND INTERFACE

A provisional interface for the BGS has been developed to be used by a technician intra-operatively. In addition, there are several important features to note regarding the implementation of both camera calibration and 2D-3D registration

3.2.5.1 USER INTERFACE

A graphical user interface (GUI), implemented in MATLAB is used to operate the BGS software. The GUI provides for basic functionality such as: manual alignment, fragment optimization, loading/saving data, communication with the C-arm, and contact stress computation. It consists of four separate windows which control functionality the BGS, 3D visualization, image I/O, and C-arm calibration. The BGS display facilitates control of the 2D-3D registration as well as contact stress computation. It consists of two main fluoroscopy views, with a colored overlay representing the corresponding DRR. The position and orientation of fragments in the DRR can be manipulated using mouse motions, allowing for manual alignment of fragments.[104] Optimization of individual and multiple fragments can also be triggered from this interface (Figure 3.13). 3D models of the fracture reduction are displayed on a 3D view window which in typical usage is presented on a large display in the operating room. Data on this window can be rotated and manipulated by mouse and keyboard. Contact stress results are displayed and manipulated in the same manner. No accommodations have been made to allow surgeons to manipulate the 3D display. Instead all manipulation and control of the GUI is to be performed by a trained technician.

www.manaraa.com
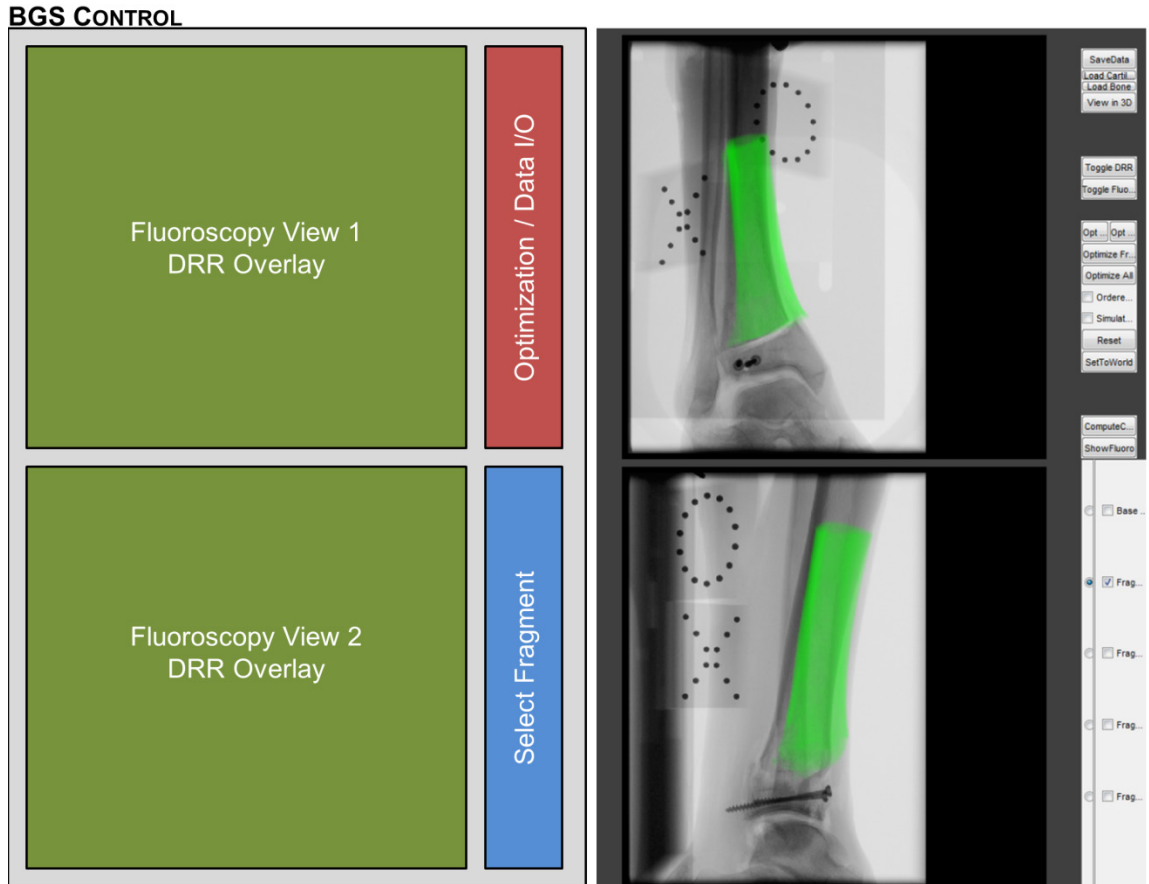
Figure 3.13: BGS control GUI shown as schematic diagram (left) and computer screenshot (right). Provides display of bi-plane fluoro views with overlay of bone fragment DRR (right, green). Mouse and keyboard input can be used to manipulate alignment of fragment on DRRs. Additional controls are available for automated alignment, and selection of specific bone fragments (red and blue).

The image control interface manages communication with the C-arm, calibration of the C-arm, and transfer of data to the main BGS software. (Figure 3.14) The technician is able to scroll forward/backward through the operation to review previous results if necessary. It also provides ability to load new fluoroscopy views, while the operating on the "current" step of the surgery. While C-arm calibration is largely automated, in a real operation it may be necessary to manually manipulate results. An interface was developed to allow the technician to view a set of 2D bearings, and their known 3D coordinates. Two dimensional bearing locations can be added, deleted or modified, and correspondences between 2D and 3D bearings can be manually assigned. (Figure 3.15)

68
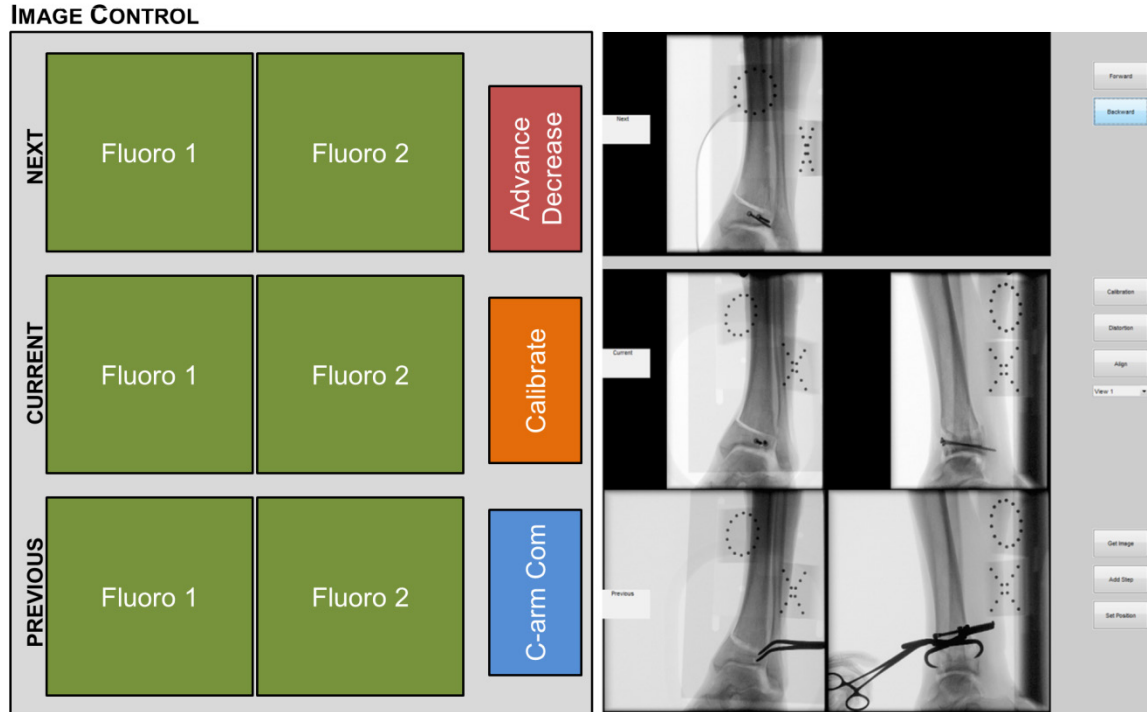
Figure 3.14: Image control GUI shown as schematic diagram (left) and computer screenshot (right). Provides display of all usages of BGS over course of operation, and allows review of previous results (red). The interface controls communication with the C-arm (blue) as well as initiation of image calibration (orange).

The overall intended usage pattern of the BGS is diagrammed in Figure 3.16. In general, the automated alignment does not have sufficient capture region compute the initial registration or registration following large displacement of bone fragments. Manual manipulation of bone fragments is required to initialize system. Subsequent registrations rely more closely on automated registration processes.
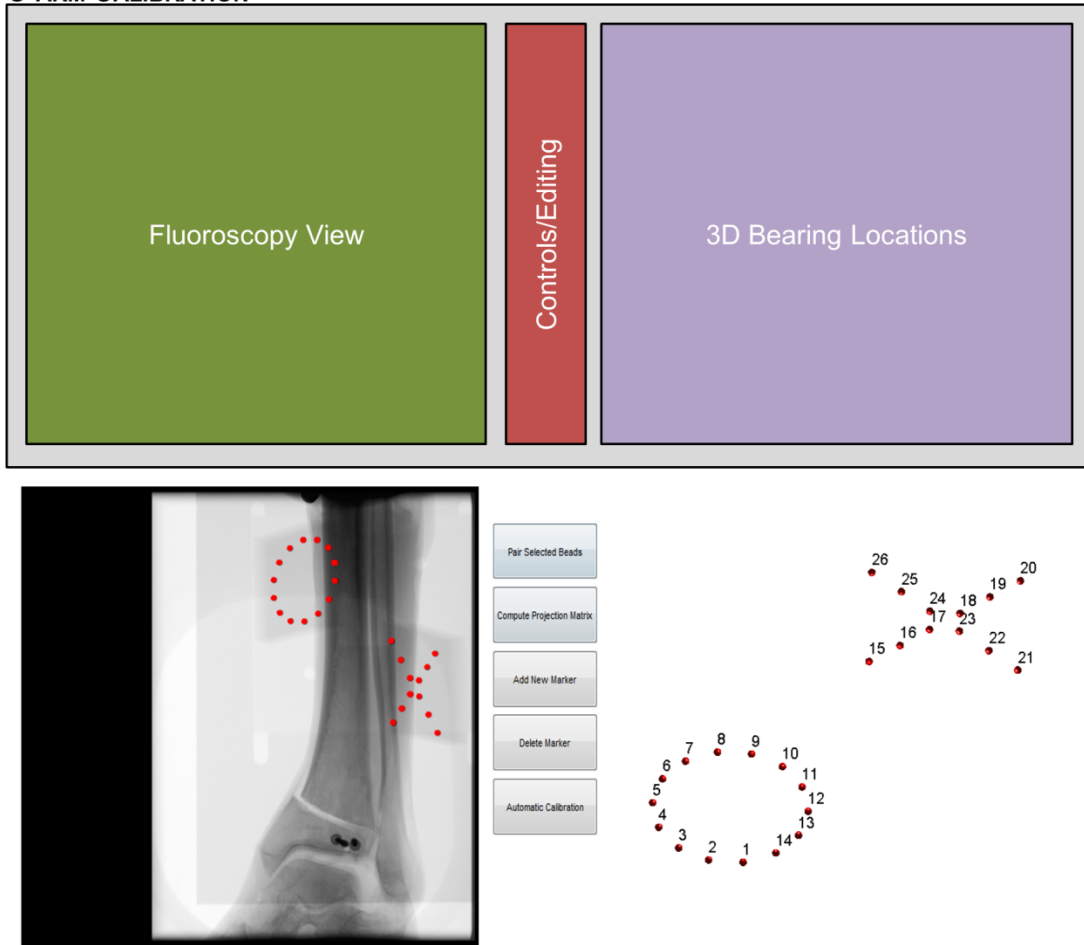
Figure 3.15: C-arm calibration GUI shown as schematic diagram (top) and computer screenshot (bottom). Although calibration is typically fully automated, in the case of failure this interface provides ability to manually select 2D-3D correspondences. Displays 3D model of bearings (right) controls for interface (center) and 2D fluoroscopy image with detected bearing centers (left).
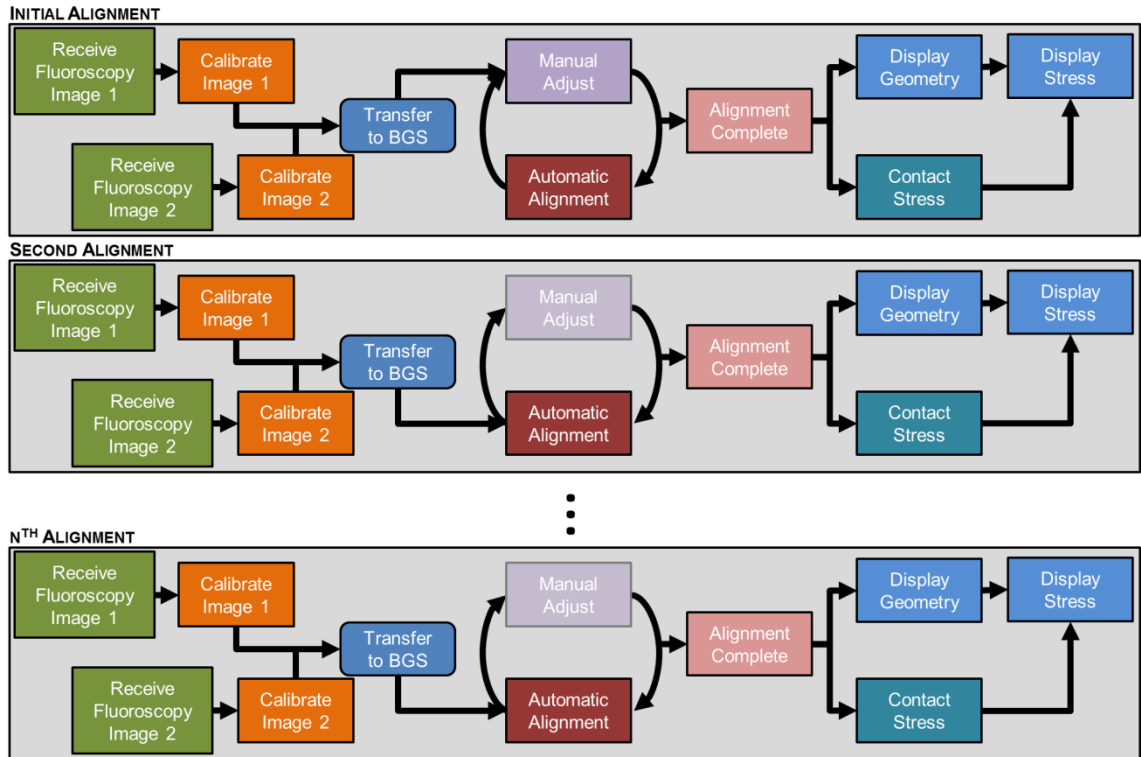
Figure 3.16: Overall usage of BGS system, describing steps required by software and technician required to computed 3D display as well as contact stress result. Initial alignment (top) requires significant manual intervention. Subsequent steps rely primarily on automated alignment with manual supervision (bottom).

3.2.5.2 FRAGMENT PRE-PROCESSING

This system has been implemented in MATLAB 2014a with C++ MEX functions used for graph-cuts and VTK visualization, and ITK-snap software used for manual editing. Polygon surface models of individual bone fragments (STL format .stl) and a 3D label volume (NIFTI format .nii) are outputs.

3.2.5.3 CUDA

Execution of 2D-3D registration intra-operatively, places emphasis on excellent computational performance. Even small speed differences within subroutines computed thousands of times have a large impact on the overall perception of a navigation system, particularly in the case of DRR generation and image comparison. When performing optimization, thousands of DRRs and image comparisons are required for a single

71

alignment. Although these methods are relatively simple to implement naïvely, they are computationally expensive. Fortunately, these algorithms lend themselves to straightforward parallelization. Multi-core and multi-threaded CPUs have become quite common, even in household desktop computers, tablets, and smartphones. These CPUs however, are optimized for general purpose computing tasks and are outperformed by more purpose built, graphics processing units (GPUs). Originally little more than fixed-pipeline co-processing units, GPUs have evolved into robust, programmable, massively parallel vector processing units. While modern CPUs are capable of executing 2-64 threads simultaneously, high end GPUs are on the order of ~4000 simultaneous threads.[105] This increased execution ability increased the need for memory throughput and GPUs have many times higher memory bandwidth.

CUDA is an API developed by NVidia which allows GPU functions (kernels) to be called from software executed on the CPU. While a comprehensive description of CUDA and general purpose GPU (GPGPU) programming is well outside of the scope of this document, there are several important items to note regarding implementation.

CUDA organizes execution of threads in a hierarchical manner beginning with groupings of 32 threads called "warps". Each thread in a warp executes in lock-step and divergence within a warp is not possible (all 32 threads execute the same operation simultaneously, regardless of the number of threads which use the result). Warps are organized into blocks (up to 1024 threads on current hardware), which are further organized into grids. NVidia GPUs are organized into modular arrays of streaming multiprocessors (SM), which handle many threads concurrently (called single instruction

multiple thread architecture, SIMT).[105] One block is meant to reside on a single SM (an SM can handle many blocks simultaneously).[105]

This hierarchical architecture, while necessary for organizing data and thread execution, is complex and sometimes difficult to achieve full utilization of the hardware within a single CUDA kernel. Streams are a mechanism used to improve this, as they allow execution of multiple independent kernels simultaneously. A single stream executes commands in serial; however there is no guarantee about the ordering of execution of different threads. This must be enforced with explicit synchronization of streams. In subsequent details of BGS implementation, hardware utilization is maximized, in part, by performing kernel execution on multiple separate streams.

Just as the execution hierarchy of CUDA software is complex, so also is the memory hierarchy. The memory used in GPUs achieves high bandwidth by accessing multiple adjacent addresses simultaneously (32, 64 or 128 bytes). If the order of memory access is "aligned" with a warp then a single memory access can populate data for multiple threads simultaneously. If memory access is not aligned (offset, or random) multiple accesses are required for each warp. Since all threads in a warp must run in lock-step, the entire warp stalls when waiting for these serial memory accesses. Improper implementation of memory access in CUDA clearly can result in large performance degradation. This is manageable in most situations, however ray-casting through a volume typically relies on accessing unaligned memory addresses within a warp. Fortunately modern GPUs contain a texture cache, which utilizes the spatial relationship between pixels or voxels to organize cache accesses. Three dimensional textures in CUDA allow much higher

73

throughput access to volume information, and proved ability to perform interpolation of these values for very little additional overhead.

A final consideration regarding CUDA is latency with regards to data transfer and kernel execution. Data transfer between the CPU and GPU incurs a specific latency penalty and it is desirable to limit the size and frequency of communication. In the BGS data transfer latency is mitigated mostly through pre-allocation and transfer of GPU data, in normal operation of the system very few images need to be transferred.

Further reading about the CUDA programming model, architecture and API details can be found by consulting the CUDA Programming Guide (NVidia Corp, Santa Clara, CA).[105]

Figure 3.17: Implementation of DRR generation and memory transfer between host and GPU device. Both image DRR images and image similarity are computed on the GPU with no CPU requirement. During optimization only small pieces of data are transferred.

3.2.5.4 FRAGMENT POSE ESTIMATION

To accelerate processing of DRR and image similarity results, time sensitive portions of the fragment pose estimation has been implemented in C++ and CUDA. MATLAB is used for less computationally intensive portions of the framework, such as implementation of the optimizer or visualization. All file I/O, and control of the system is

controlled via a MATLAB interface. This software is designed such that C-arm information, fragment volumes, and transforms are allocated to GPU memory a single time. To achieve high speed optimization results, images are not transferred from GPU to host memory, instead image similarity is computed directly on the GPU device and a single 32-bit floating point value is transferred to the host, indicating the matching between fluoroscopy and DRR.[95] (Figure 3.17)

3.2.5.5 DRR GENERATION

DRR generation is implemented in CUDA, where multiple DRRs are computed simultaneously for separate C-arms. A DRR is generated for each bone fragment on separate CUDA streams, and then composited to form a final MDRR. (Figure 3.18) Commonly, when performing manual manipulation of fragments or optimization, only a single fragment is being moved. In this case, DRRs of other fragments are unexpected to change. Fragment DRRs are cached in GPU memory such that if a fragments position is unchanged relative to the C-arm, it is not recomputed.

Sampling of the fragment volume is performed using GPU 3D texture cache. This is a high bandwidth cache that uses the spatial locality of texture (voxel) data to maintain cache coherency.[25, 105]
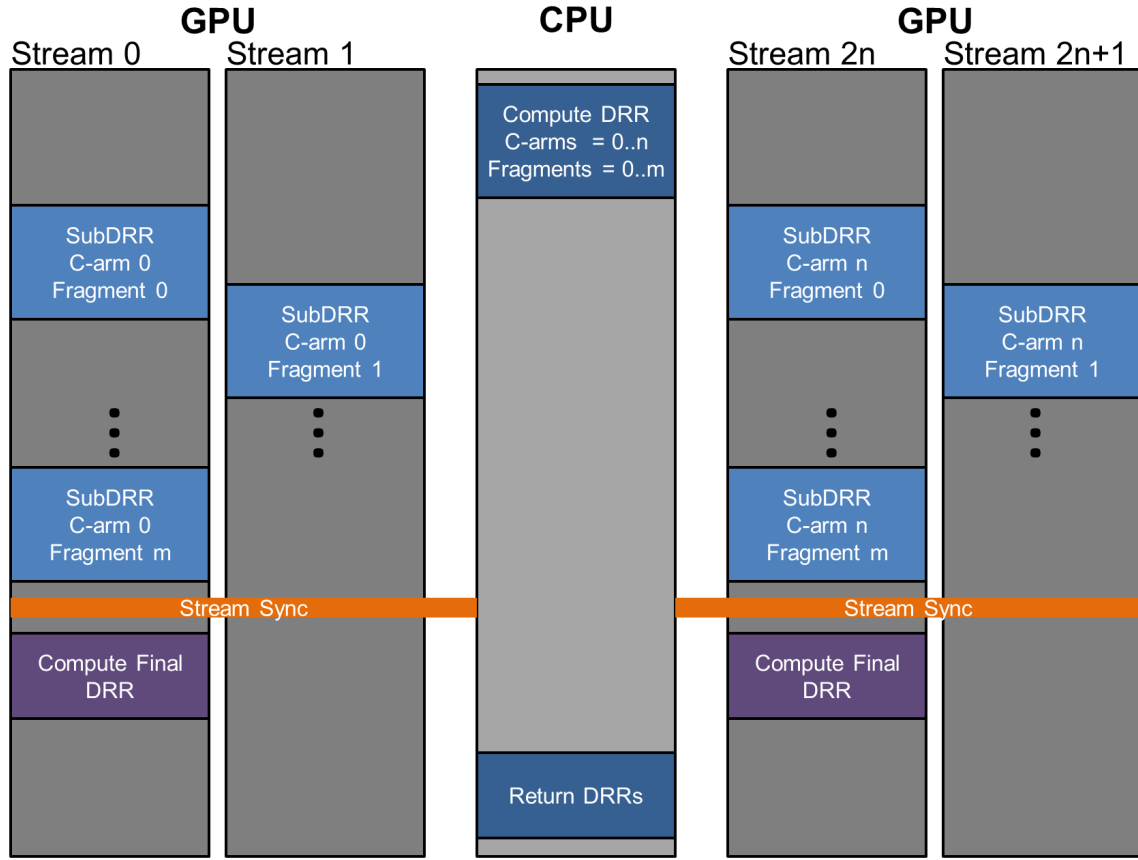
Figure 3.18: Organization of DRR generation implementation. Each C-arm is assigned two CUDA streams, which are used to compute subDRRs. Synchronization is performed then final MDRR is composited. This scales across multiple C-arms simultaneously.

3.2.5.6 IMAGE COMPARISON

Image comparison is implemented in CUDA, using a multi-threaded/multi-stream implementation. There are three discrete kernel functions, used in this implementation: Gaussian smoothing, normalized cross correlation, and derivative calculation.

The smoothing kernel uses Deriche's recursive Gaussian blur method, which is advantageous as its execution time is independent of the width of smoothing.[106] The implementation is based on and modified from the code sample included with the CUDA v8.0 documentation.[107]

Normalized cross correlation typically requires pre-computation of global statistics such as the mean, and standard deviation of compared image regions, prior to correlation computation. In CUDA, this is problematic as it requires, additional kernel launches causing increased latency and overall reduced performance. Instead cross correlation, previously defined as:

$$NCC = \frac{1}{n} \sum_{i=0}^{n} \frac{(I_{drr}(i) - \mu_{drr})(I_{ref}(i) - \mu_{ref})}{\sigma_{drr}\sigma_{ref}}$$

can be rearranged to:

$$NCC = \frac{n \sum I_{drr}(i)I_{ref}(i) - \sum I_{drr}(i) \sum I_{ref}(i)}{\sqrt{n \sum I_{drr}(i)^2 - \left(\sum I_{drrf}(i)\right)^2} \sqrt{n \sum I_{ref}(i)^2 - \left(\sum I_{ref}(i)\right)^2}}$$

such that each individual term is computed separately within a single pass. While this technique is susceptible to numerical instability, the use of normalized image values and double precision floating point variables mitigate this concern.

Partial derivatives of the smoothed images are computed using a Sobel operator implemented in CUDA.[92]

As computation of the image similarity metric requires multiple kernel launches, and many of these have execution dependencies, special care was taken in their implementation. Each image comparison uses two CUDA streams, in attempt to mask kernel launch latency and to maximize GPU resource utilization. A schematic diagram of this can be found in Figure 3.19.
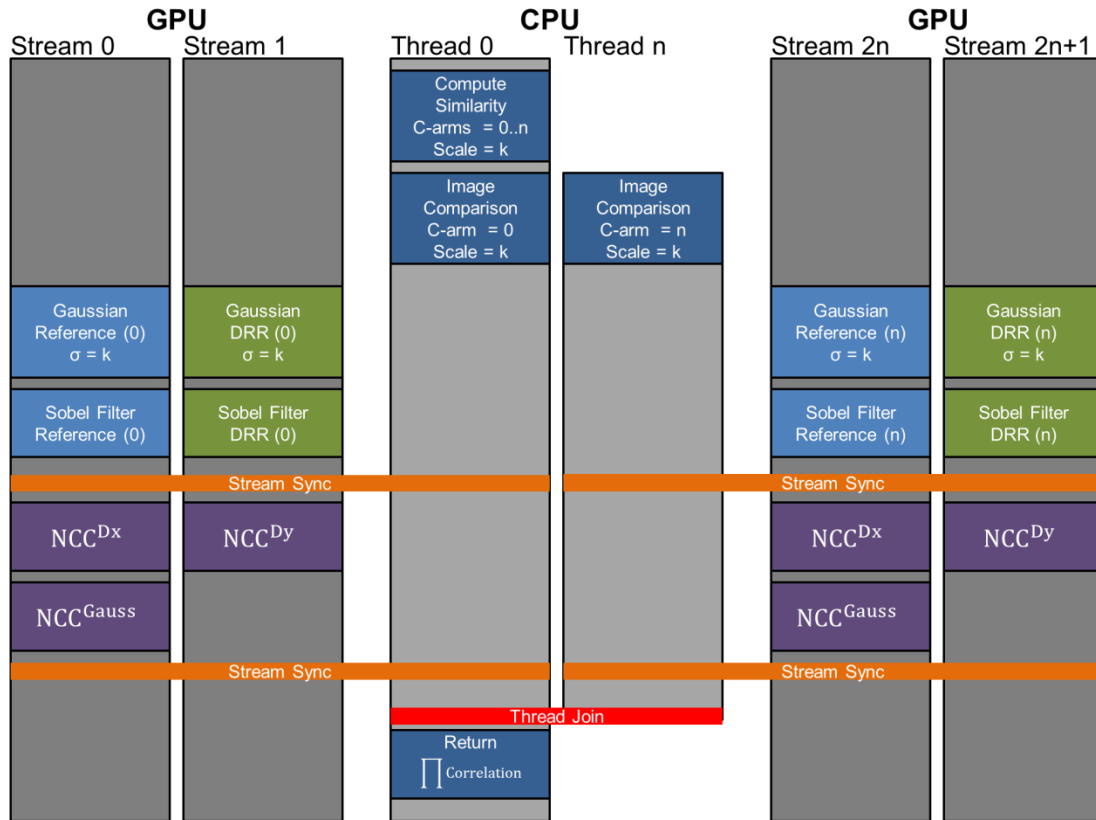
Figure 3.19: Organization schematic of image similarity computation. Image similarity for n views is called. Image comparison is performed on n CPU threads, one for each view. Each image comparison uses two CUDA streams, run independent components of execution. Each block represents a function or kernel execution.

Image similarity is often performed on multiple fluoroscopy views simultaneously. Outside of tabulating the final result, similarity computations for these views are entirely independent. Each image similarity computation is executed on a separate CPU thread, in attempt to maximize parallelism.

3.2.5.7 OPTIMIZATION

Multi-scale optimization is performed with a scales selected for σ at 10 and 3 for the large and small scale optimization, respectively. The optimization algorithms used are implemented in the NLopt library (http://ab-initio.mit.edu/nlopt), an open source library

78

which implements a wide variety of optimization algorithms.[108] Their included MEX wrapper is used to call optimization functions from within MATLAB.

3.2.5.8 FLUOROSCOPY SYSTEM COMMUNICATION

Images are transferred from the fluoroscopy system to the BGS workstation through a DICOM Service Class Provider implemented with DCMTK (OFFIS e.V. Oldenburg, Germany). DCMTK is a collection of open source libraries, which provides a host, of DICOM transfer, query, and other communication functionality.[109] This allows rapid transfer of fluoroscopy images and header data with no quality degradation. It is a custom implementation, which is optimized to cache and query of DICOM information within system memory (files are also archived in storage) to reduce data access latency. This allows access of data from other C++ functions, as well as MATLAB, through the use of a MEX wrapper.

3.3 CONTACT STRESS COMPUTATION

While determination of the 3D bone fragment positions, serves as a pathway to enhanced geometrical assessment, this information can also be leveraged for biomechanical assessment. As the transformation for each virtual fragment, H_{Fi}^V, is calculated through 2D-3D registration it is assumed to be rigidly fixed relative to other bone fragments. A provisional 3D articular surface is then created from the union of all articular fragments in the registration where:

$$FullSurface = \bigcup_{i=1}^{n} H_{Fi}^V F_i$$

79

The assumption that all bone fragments are fixed relative to one another (i.e. the surgeon has achieved perfect fixation) is a necessary simplification to achieve fast and reliable contact stress results. This provisional surface is then used as input to a discrete element analysis algorithm, for the computation of contact stress. (Figure 3.20)
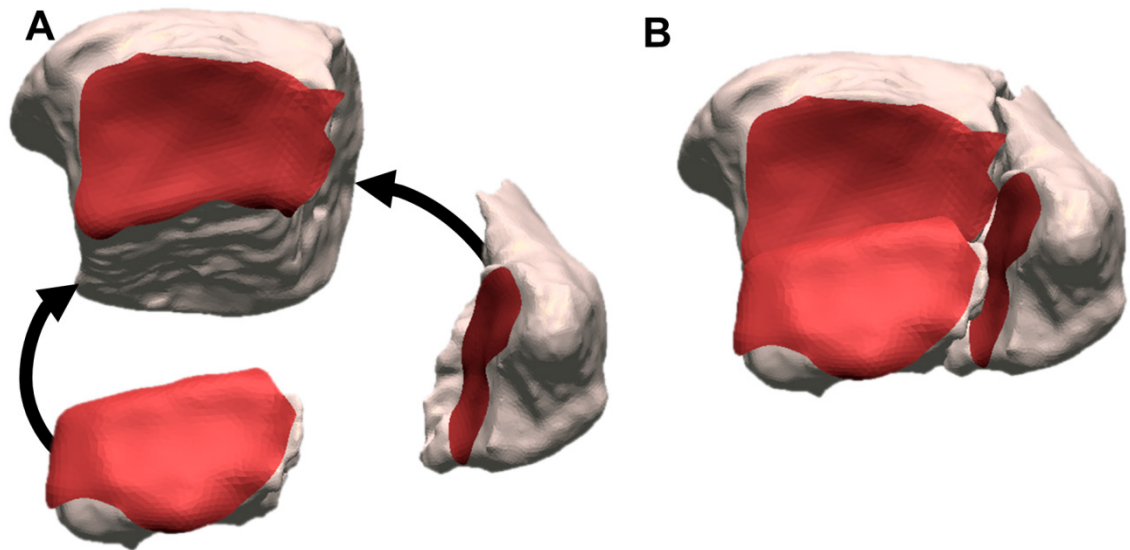
Figure 3.20: Surface geometry for contact stress models is obtained from pre-operative CT segmentation. As an articular fracture consists of multiple independent bone fragments (A, salmon), the relative positions of these are computed with 2D-3D registration. The cartilage surfaces (red), uniformly extruded from fragment subchondral bone regions, are merged to form a final, rigid articular surface model (B) It is assumed that the articular fragments are rigidly fixed.

The articular surface of the opposite side of the joint, the talus obtained from segmentation of the pre-operative CT, is aligned manually aligned in pre-processing to a neutral weight bearing orientation. The fibula is not explicitly modeled in this simulation.

3.3.1 DISCRETE ELEMENT ANALYSIS

Contact stress assessment is performed using discrete element analysis (DEA), which has been previously validated in the human ankle joint.[65] DEA is a simple, contact stress only computational modeling technique that treats cartilage as an array of independent springs (Figure 3.21).[110, 111] It uses a simple relationship between elastic

80

modulus, E, and poisons ratio, v, to compute spring constants, k, derived from uniaxial plane strain.[112]

$$k = \frac{(1-v)E}{(1+v)(1-2v)h}$$

Where h, is the thickness of the cartilage layer. In the case of a triangulated surface model, springs are assigned to each vertex of the surface, extending along the surface normal. When two apposed surfaces are in contact, their overlap is used to approximate strain (δ). Contact stress is computed for each spring:

$$\sigma = k\delta$$

Force is computed as the product of an area associated with each spring and its contact stress. This is ultimately a function of the relative position of the contacting surfaces. A Newton's method solver can be used to estimate the articular surface pose which matches force and displacement boundary conditions.[65, 66]
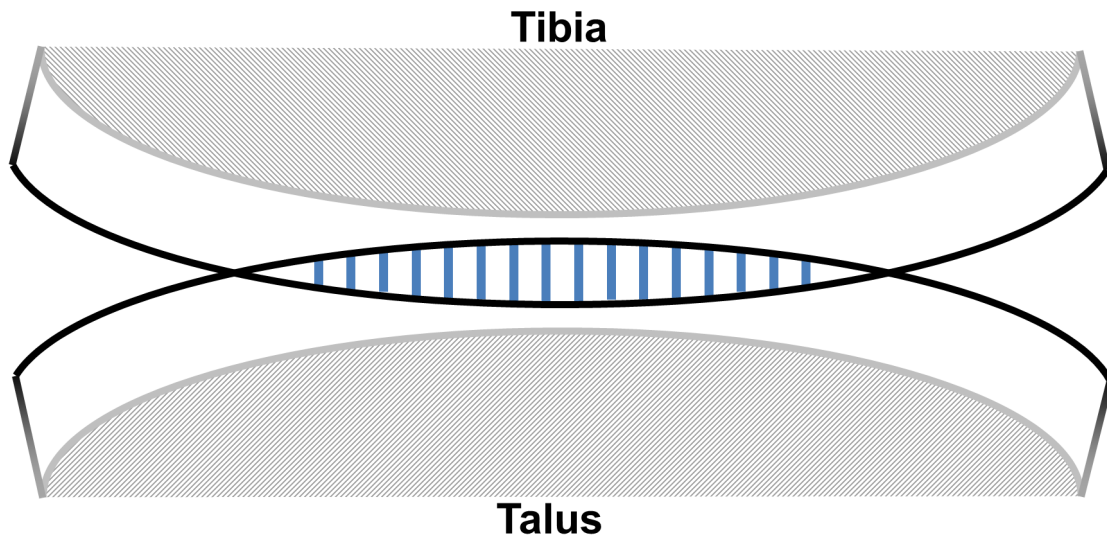
Figure 3.21: Discrete element analysis models bone surfaces (grey) as rigid. Contact is computed where opposing articular cartilage surfaces (black) have penetrated. An array of springs (blue) is used to model articular contact pressure.

This simplified methodology precludes computation of internal stress, disregards effects of shear, and has difficulty modeling time-dependent features limiting its general utility in orthopaedic biomechanics. Simplicity is an advantage for ease of modeling, numerical stability, and execution time (on the order of seconds). This ease of modeling and speed of computation have caused DEA to see niche but consistent use within orthopaedic biomechanics over the last three decades.[65, 66, 113]

3.3.2 Boundary conditions

For tibial plafond fractures, a simple loading regime is used based on methods in Li et al. 2006.[8] Contact stress is computed in a single static pose using load control, with a primary load of 1000N applied down the long axis of the tibia. A second load of 100N is applied in the lateral direction on the tibia mean to represent the stabilization of the fibula. The talus is constrained in superior-inferior and medial lateral translation, but is allowed to equilibrate in the anterior-posterior direction. Similarly, flexion-extension on the talus is constrained, it is free to equilibrate with all other rotations. For this early implementation of the BGS, a simple loading regime was chosen to improve computation time of the system and ensure successful execution. Future development, could include modeling of the full gait cycle, as well as application of patient-scaled loadings. Implementation of patient specific kinematics is intractable due difficulty measuring gait on trauma patients.

3.3.3 Implementation

The discrete element analysis algorithm is implemented in MATLAB according to methods outlined in Kern and Anderson 2015.[65] This is a validated algorithm for intact

human ankle joints. It has been integrated with the 3D visualization of the BGS such that contact stress results are overlaid on the bone fragments upon completion of execution.

3.4 EXPERIMENTAL EVALUATION

Prior to assessment of the BGS as a whole, individual components of this system were evaluated for accuracy and usability.

3.4.1 FLUOROSCOPY CALIBRATION

The process of fluoroscopy calibration was evaluated on a series of 16 images of a static cadaveric ankle and calibration object. Between acquisitions of each image, the gantry was rotated by ~10°. This was done to determine the performance of the calibration algorithm on real images, as a function of clinically applicable view angles.(Figure 3.22)

Figure 3.22: Evaluation of calibration methodology was performed by taking 16 images spaced at 10 degree rotations about the gantry.

Calibration was performed on each image, success rate, execution time, and

reprojection error (RE) of each ball bearing were computed.

$$RE = \frac{1}{n}\sum_{i=0}^{n}|x_i - PX_i|$$

where RE is the Euclidean distance between reprojection of the known 3D point coordinates (X_i) with computed projection matrix, P, and the coordinates of the bearing centers directly from the image.

In a realistic clinical scenario, it is likely that bearings are occasionally occluded by surgical instrumentation. To account for this, a single bearing was synthetically removed from each image and this same analysis was completed. This was repeated 26 times (removal of each bead systematically) to represent the occlusion of any single bead. This same process was again repeated but for the occlusion of two beads. These results are reported in Table 3.2.

Table 3.2: Reliability, accuracy and computation time of calibration algorithm with all bearings present, 25 bearings present and 24 bearings present.

Rotation (degrees)	All Bearings (26)			25 Bearings			24 Bearings		
	Success (%)	RE (pixels)	Time (seconds)	Success (%)	RE (pixels)	Time (seconds)	Success (%)	RE (pixels)	Time (seconds)
0	100%	0.04	0.49	100%	0.04	0.56	91%	0.04	1.99
10	100%	0.02	0.43	88%	0.02	0.47	81%	0.02	1.49
20	100%	0.02	0.36	100%	0.02	0.53	89%	0.02	1.91
30	100%	0.03	0.33	100%	0.03	0.57	90%	0.03	1.80
40	100%	0.03	0.37	100%	0.03	0.56	91%	0.03	1.84
50	100%	0.10	0.35	100%	0.10	0.45	91%	0.10	1.41
60	0%	-	-	0%	-	-	0%	-	-
70	0%	-	-	0%	-	-	0%	-	-
80	0%	-	-	0%	-	-	0%	-	-
90	100%	0.03	0.35	96%	0.03	0.47	83%	0.03	1.49
100	100%	0.02	0.35	100%	0.02	0.45	89%	0.02	1.46
110	100%	0.02	0.37	100%	0.02	0.47	91%	0.02	1.41
120	100%	0.04	0.36	100%	0.04	0.47	91%	0.04	1.40
130	100%	0.05	0.40	100%	0.05	0.61	91%	0.05	1.89
140	100%	0.04	0.38	100%	0.04	0.61	91%	0.04	1.88
150	100%	0.05	0.39	100%	0.05	0.60	90%	0.05	1.91

Overall, the calibration has excellent performance when sufficient beads are detected. The low computation time, (~0.3 - 2.0 seconds) is suitable for intra-operative use, and the high success rate generally means that there is little requirement for manual adjustment. The complete failure of the algorithm in 60-80° view angles is a result of the degeneracy of the calibration object from that viewpoint. When looking down this view, one of the planes of the beads is unidentifiable. (Figure 3.22, 70°) Future development of new object geometries or calibration techniques may solve this problem. In the current usage of the BGS however, careful positioning of the calibration device will prevent this failure from occurring.

Perhaps, more important to discuss is the high combinatorial complexity of this algorithm with regards to missing bearings. In practice this algorithm is intolerant of >4 missing bearings. This is a subject of future work and algorithmic improvement for the success of the BGS in a general clinical setting.

3.4.2 DRR GENERATION

The relative accuracy of DRR generation was provisionally examined through the comparison of line-profiles of intensities taken from both the DRR and a corresponding fluoroscopy image of a tibial plafond fracture. This was first performed to verify the importance and influence of multiple occluding bone fragments on the similarity of two images. Second, this was performed with the full DRR image (all fragments) to compare multiple line profiles. The results shown in Figure 3.23 and Figure 3.24, demonstrate the importance of modeling multiple overlying bone fragments as well as provide confirmation of the accuracy of the DRR generation algorithm.
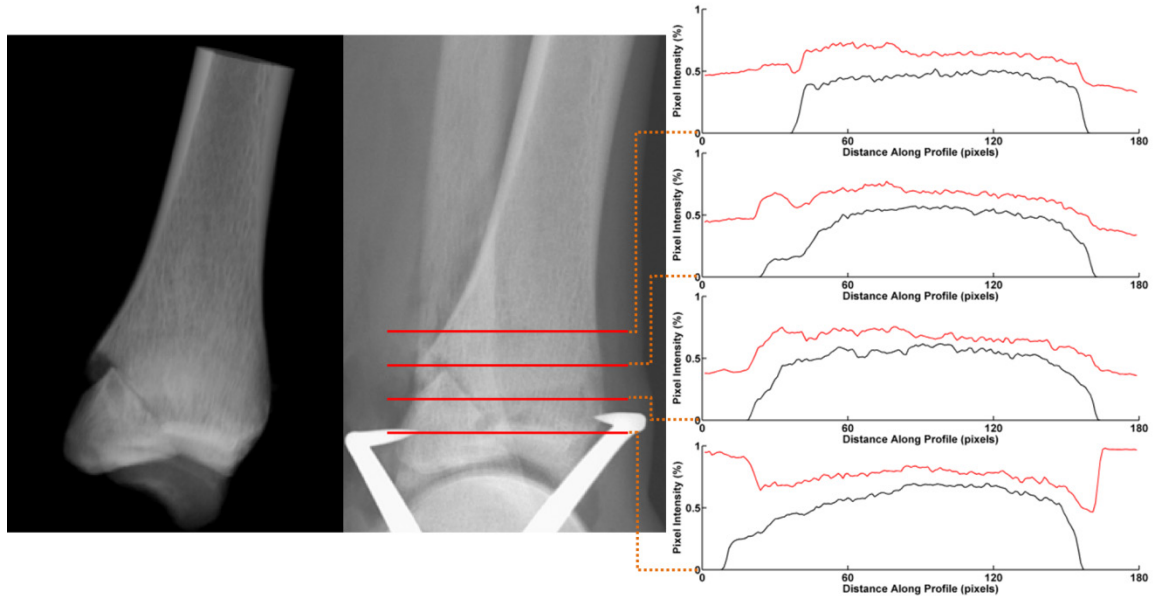
Figure 3.23: Line profiles (right) through MDRR (left) show similarity with fluoroscopy image (middle).

Results shown from these line profiles demonstrate that the DRRs computed for the BGS present a very similar intensity profile, to the fluoroscopy images, albeit with lower absolute attenuation. This is likely due to the lack of soft-tissue, fibula and surgical hardware in the DRR.[27] The conversion between CT Hounsfield units and linear attenuation may have also caused minor inaccuracies as this was interpolated from literature data. Additionally, the importance of MDRRs is shown for matching image intensities. The gestalt of fracture fragments, presents a much greater similarity to the reference image than any of the individual fragments. The findings of Haque et al. 2013, support this by showing that inclusion of adjacent bone fragments, improves the reliability and accuracy of registration results.[27] Although this is a very cursory comparison between DRR and fluoroscopy imaging, we feel that it is sufficient based on current alignment accuracy results. If additional alignment accuracy is needed this may be a topic for further evaluation and improvement.

87
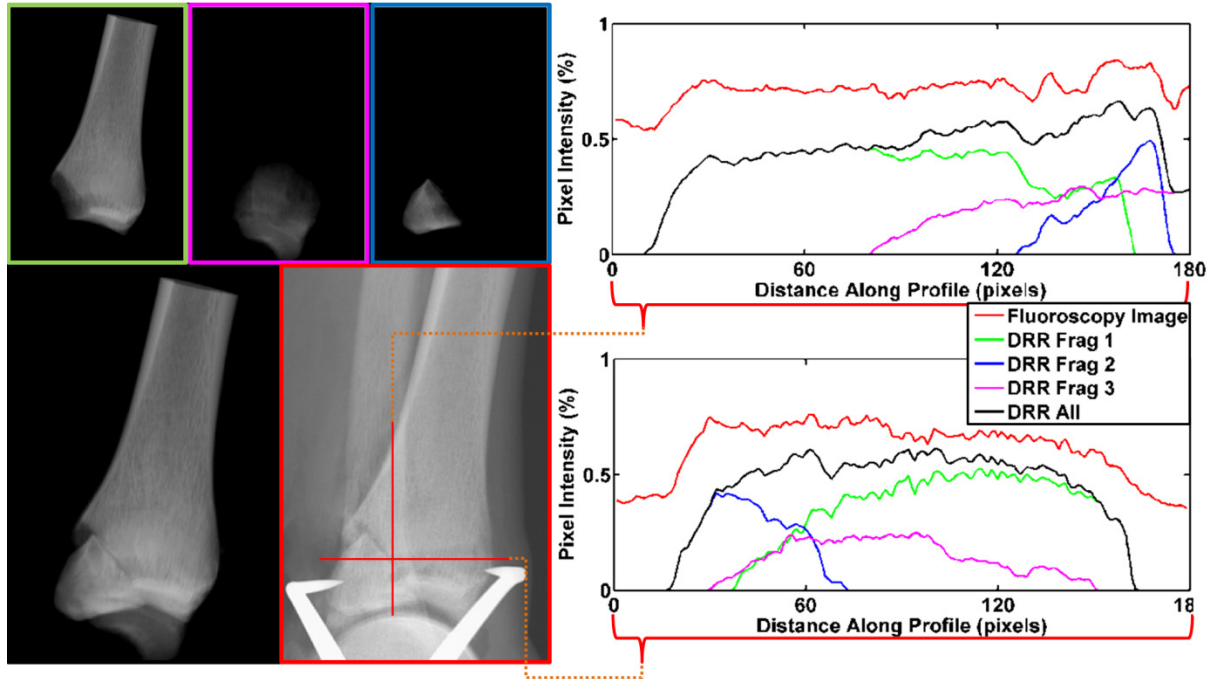
Figure 3.24: Evaluation of importance of MDRR. Individual fragment DRRs shown (top) and final MDRR (middle left) with fluoroscopy image (middle right) which has been inverted. Line profile of pixel intensity relationship shows contribution of individual bone fragment to comparison with real image (bottom).

3.4.3 IMAGE COMPARISON

The image comparison metric was evaluated using CT and fluoroscopy data from a real cadaveric tibia fracture. The BGS software and manual intervention was used to find the optimal transformation which brings the virtual and real bone fragment into registration. This was used as "ground truth". The position of the virtual fragment was then systematically varied in all 6 DOFs in increments of 0.1 mm or 0.2° ranging from [-20mm, 20mm] and [-50°, 50°]. Scale of the comparisons was also performed by varying the Gaussian smoothing σ value from [1, 15] in increments of 1. Results of this, shown in Figure 3.25 and Figure 3.26 display an excellent relationship between alignment error as well as the effect of scaling on smoothness of the similarity function. It is desirable that at large scales (high σ values) the similarity function is relatively smooth, providing a wide capture range for optimization. At low values, a distinct minimum, at the appropriate

alignment location is required for rapid and unambiguous convergence of the

optimization routine.
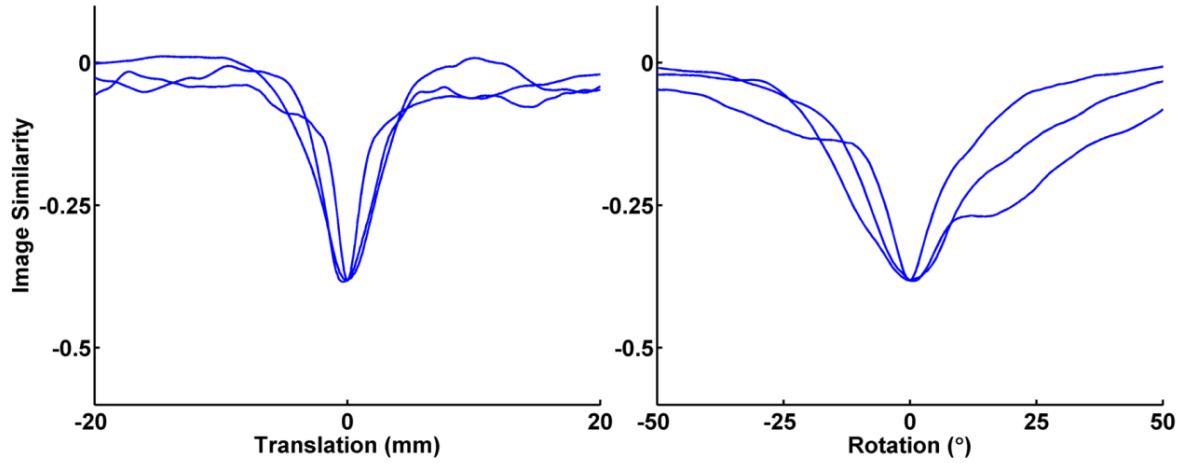
Figure 3.25: Image similarity of between fluoroscopy and DRR image as virtual bone fragment is translated (left) and rotated (right) from ideal alignment. Similarity computed at a smoothing level $\sigma = 1$. Transformations are performed in (x, y, z) dimensions independently.

89
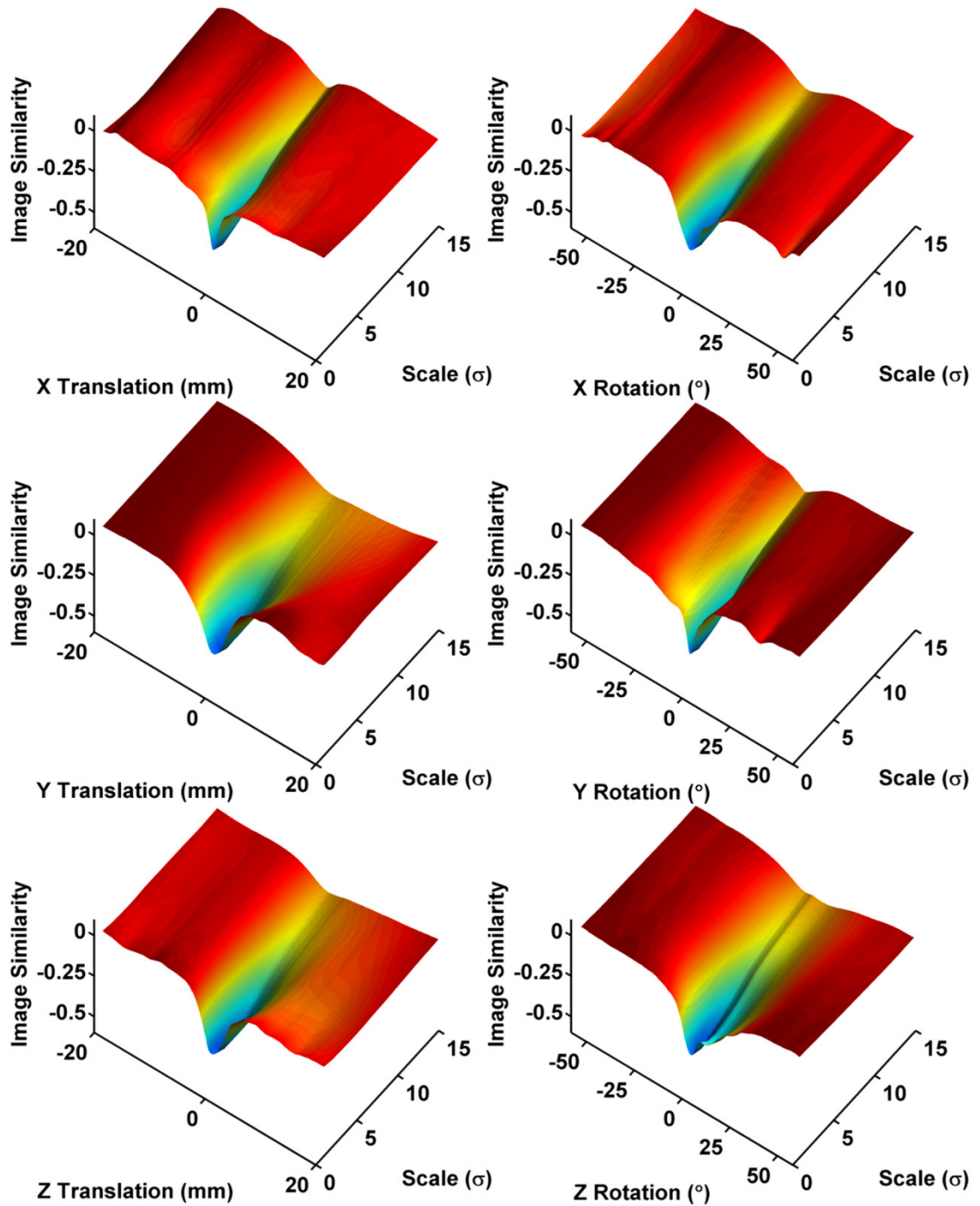
Figure 3.26: Multi-scale image similarity between fluoroscopy image and DRR computed on all 6 DOFs. Similarity plotted as virtual fragment is transformed from ideal alignment position. Image scale ranges from 1-15.

3.4.4 FRAGMENT POSE ESTIMATION

The accuracy of fragment post-estimation was tested using a publicly available gold-standard dataset. This dataset, described in Tomazivec et al. 2003, provides CT images, 2D fluoroscopic images and a set of gold-standard registrations for a human cadaver lumbar spine.[114, 115] (Figure 3.28) Registrations are performed on the C1-C5 vertebrae using their included methodology. Registration accuracy is calculated as target registration error (TRE) and registration angle error (θ). (Figure 3.27) Where TRE is 3D Euclidian distance between a test point (on the registered object) transformed with the gold standard registration (H_{GS}) and with the estimated registration (H_R).

$$TRE \ = \ |pH_{GS} - pH_R|$$

Similarly, registration angle error computes the angle between a unit vector transformed with the gold standard and estimated registrations.

$$\theta = \ \cos^{-1}(vH_{GS} \cdot vH_R)$$

While not a direct analogue for the task of fracture reduction, lumbar spine alignment shares many similarities. The vertebrae have varying geometry, and exhibit similar bone density distribution to tibial plafond fracture. They are also closely apposed, and have many over-lapping structures similar to an articular fracture. Results using this methodology are displayed in Figure 3.29 and Figure 3.30

Registration accuracy on this gold standard dataset compare favorably with other studies to utilize this data on all vertebrae except L5. The registration used in the BGS had difficulty dealing with initial registrations off the edge of the image. This dataset is also limited by the presence of four large seams dividing the fluoroscopy images into

91

quadrants. This is presumably because at the time of data collection ~2000, technology

for large FPDs was unavailable or prohibitively expensive. Since our similarity metric is

based both on image intensity and gradient, it is likely more sensitive to these

abnormalities than a purely gradient-based technique. A median filter was used in all

results in attempt to remove this artifact.
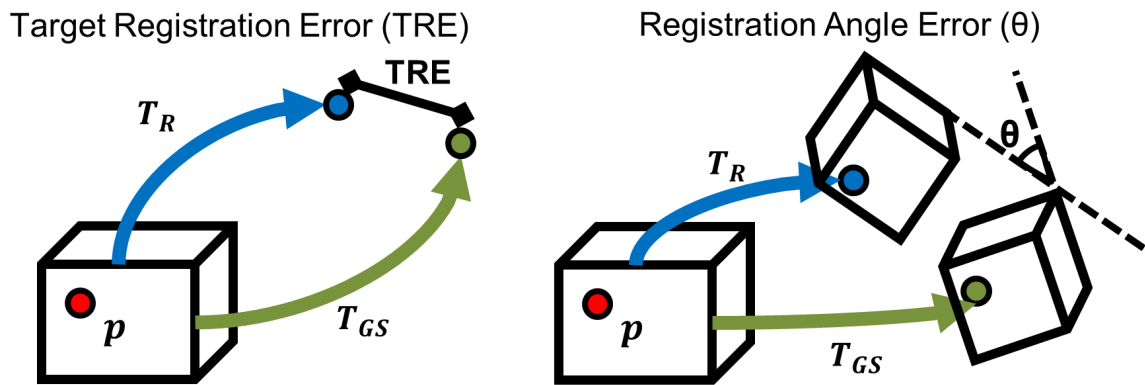
Figure 3.27: Illustration of target registration error (TRE) and registration angle error (θ) used to quantify registration accuracy of BGS.

The accuracy displayed by this system, is sufficient for use by the BGS, as it is likely

in excess of what a surgeon can physically achieve. Future work is required (Chapter 4)

to determine if the accuracy of the BGS has a significant effect on the reliability of

contact stress computation. More of an issue, however, is the presence of failures in the

2D-3D alignment on this dataset. Although it is unrealistic to expect perfect accuracy, a

higher success rate, and larger capture regions were anticipated. This may partly be

explained by the manner in which the vertebrae were perturbed prior to registration. The

included set of translations and rotations seemed to be biased to very large rotational

error vs translation. Although it is understandable that the original authors were

attempting to rigorously sample the entirety of the state-space it seems unrealistic that a

pre-alignment would start at such a high rotational error.

Future work is needed to improve the convergence and capture region of the BGS, as well as implementation of means to detect failure of registration automatically.
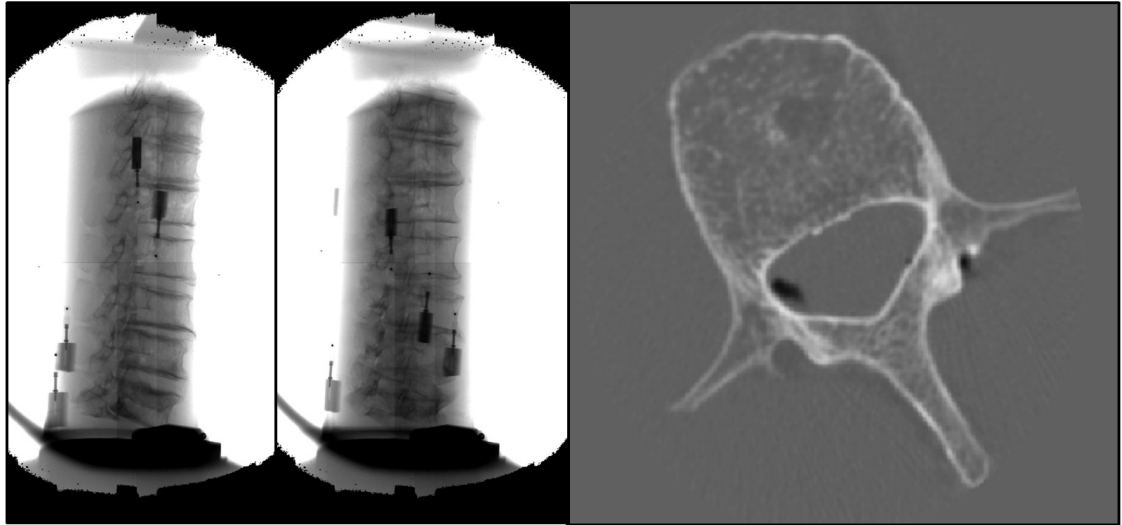
Figure 3.28: Example of images from gold standard dataset show fluoroscopy images (left) and CT cross section (right) of lumbar spine.
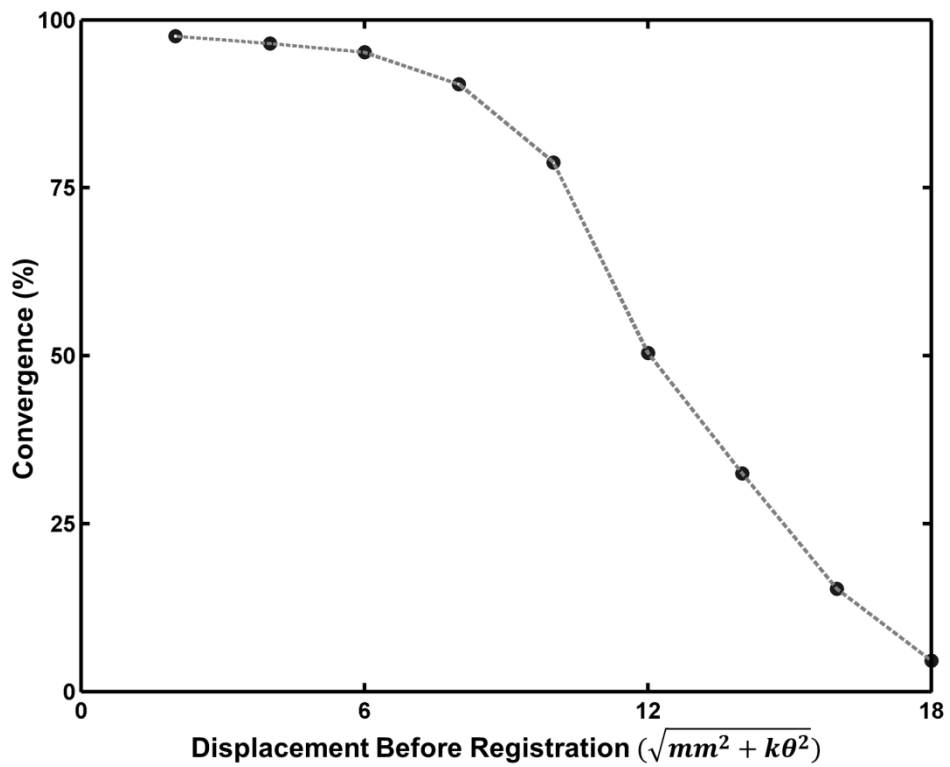
Figure 3.29: Registration accuracy (% completion) as a function of initial displacement on gold standard dataset.

Table 3.3: Registration error, and registration success as a function of pre-alignment error. Computed on gold standard dataset from Tomazivec et al. 2003.

	Before Registration				After Registration				Successful Registration (%)		
	RMS(TRE) Max(TRE) (mm)		RMS(θ) (°)	Max(θ)	RMS(TRE) Max(TRE) (mm)		RMS(θ) (°)	Max(θ)	0-6mm 0-17.2°	6-12mm 17.2-34.4.2°	0-6mm 34.4-51.7°
L1	6.7	20.8	16.4	51.6	0.5	1.1	0.7	1.2	0.99	0.77	0.24
L2	6.4	19.8	14.8	37.4	0.3	0.7	0.4	0.8	1.00	0.79	0.16
L3	6.5	18.7	15.1	37.7	0.3	1.0	0.3	1.6	1.00	0.73	0.18
L4	6.6	20.2	14.4	34.2	0.3	0.5	0.4	0.8	0.93	0.65	0.15
L5	7.2	23.2	15.3	40.9	0.6	1.0	0.5	1.3	0.89	0.71	0.18
All	6.7	23.2	15.3	51.6	0.4	1.1	0.5	1.6	0.96	0.73	0.18
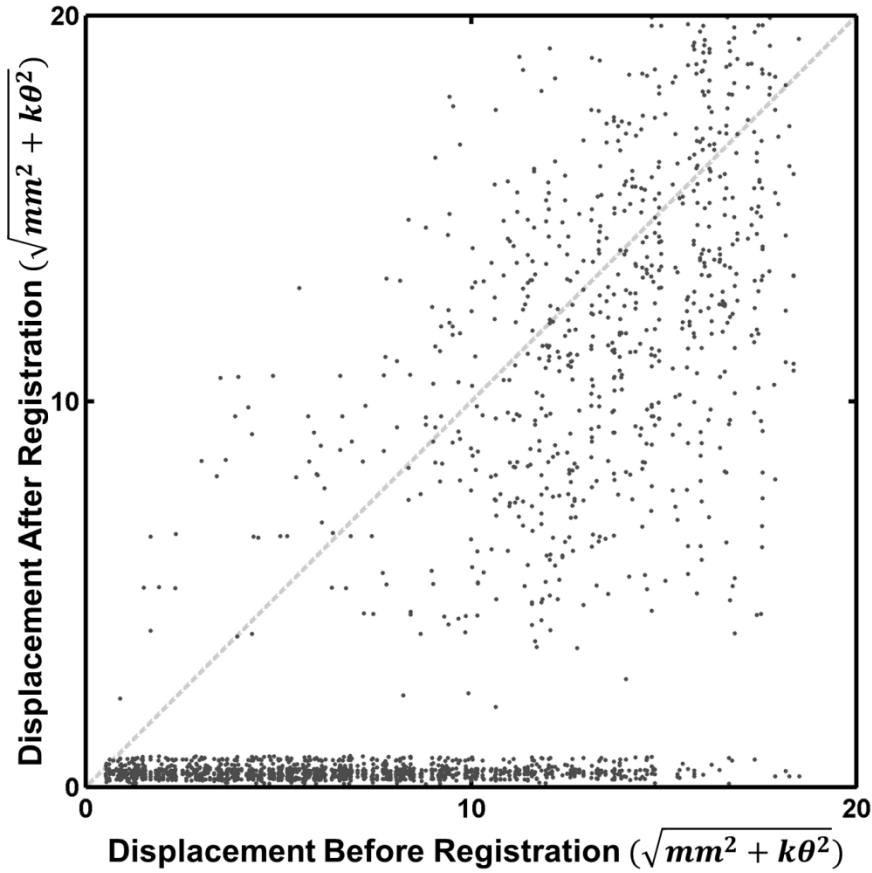
Figure 3.30: Registration accuracy (TRE) from as a function of initial displacement on gold standard dataset.

CHAPTER 4: OPERATIVE EVALUATION OF BIOMECHANICAL ASSESSMENT

Surgical reduction of intra-articular fractures (IAFs) is a physically and mentally challenging procedure. During the surgery, clinicians attempt to restore the fractured joint surface to anatomical (<2mm articular step-off), by physically manipulating individual bone fragments.[1, 2, 116] Whether performed through direct or fluoroscopic visualization, anatomical reduction requires acute understanding of joint morphology and refined spatial-visual skills.[70] This is particularly true during percutaneous reduction where visualization of the fracture is performed solely through fluoroscopy. Percutaneous reductions are favorable because they limit soft tissue damage, infection risk and soft tissue breakdown caused by extensile plating techniques.[117] Despite the noted benefits, there are also limitations to percutaneous reductions, notably the difficulty of interpretation of a complex 3D scene (fracture, soft tissue and surgical hardware) through a 2D projective image.

The achievement of anatomical articular reduction is recognized as an important factor in long-term outcomes, particularly for prevention of PTOA.[2, 31] There is little evidence however, that articular congruity can be assessed reliably or accurately intra-operatively.[14, 16-18, 48] Measurement of articular step-off as an assessment of articular congruity has long been the standard for determining the quality of a reduction. Although step-off is "simple" to measure and intuitive, it may be that more advanced measurement techniques are necessary for achieving improved outcomes.[118] The need for improved, and advanced measures is understandable as PTOA onset and progression is thought to have biomechanical origins both through acute cartilage injury and chronic

overloading.[119] Chapter 2 highlights the comparison of several metrics, such as 3D geometry and joint contact stress which may be more indicative of long-term outcomes.

In an attempt to provide enhanced geometrical and biomechanical assessment of fracture reductions intra-operatively, a biomechanical guidance system (BGS) has been developed (Chapter 3). This system is capable of providing information about the 3D positioning of bone fragments, as well as computational contact stress assessment. This system is designed to be used multiple times throughout the fracture reduction to further inform the surgeon, and check the quality of the reduction. (Figure 4.1) The BGS is unique in that it requires little additional hardware, is able to compute 3D fragment positioning using only two fluoroscopy images, and provides biomechanical information to the surgeon. Although the design and accuracy of the BGS has been previously detailed, its use has not been evaluated in a realistic surgical scenario.
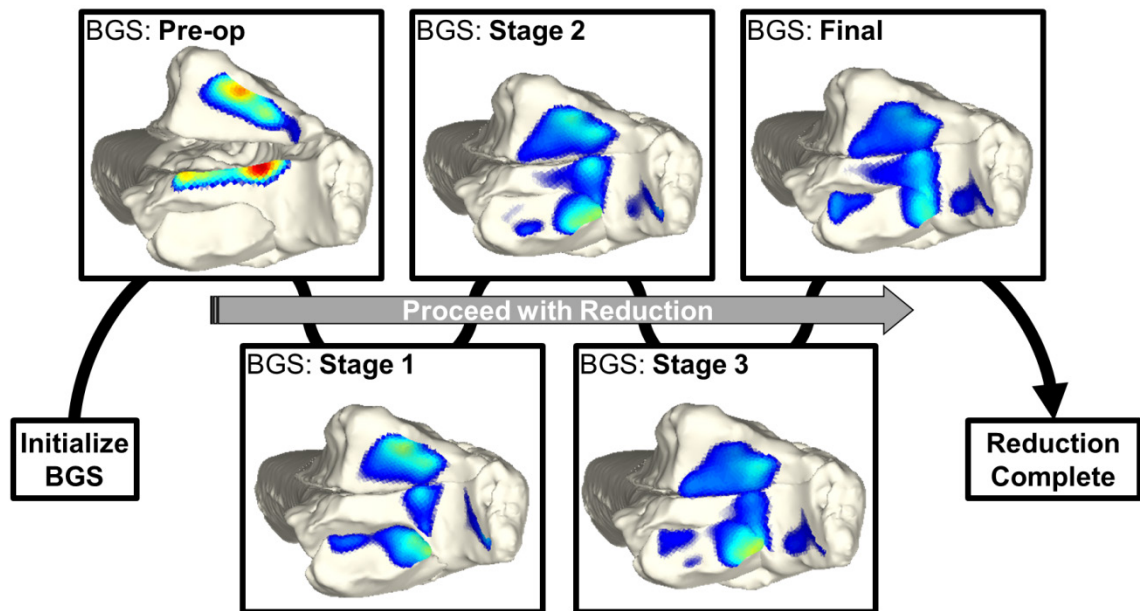
Figure 4.1: General procedure and workflow of BGS system. In surgical prep the BGS technician initializes the system and loads pre-op CT data. Immediately prior to reduction the BGS is run once to provide 3D display to the clinician. The clinician then proceeds with the operation as normal. If at any point additional information is desired, the BGS is run (Steps 1-3) and displayed to the surgeon. Upon definitive fixation the BGS is run to verify reduction quality.

96

The newly designed BGS is assessed for feasibility in a realistic setting, utility in terms of contact stress reduction, as well as accuracy of results in a surgical setting. This is performed on cadaveric tibial plafond fractures in a series of 10 percutaneous reduction surgeries. Tibial plafond fractures were selected because they are small, easily manageable joints that offer limited obstruction from surrounding tissues and clinically are particularly at risk for poor outcomes following joint fracture.[31, 58]

4.1 METHODOLOGY

Five human cadaver ankles (Figure 4.2) collected from the University of Iowa Deeded Body Program were selected for the presence of good to fair bone quality, and the absence of any noticeable morphological abnormalities radiographically. The proximal end of the tibia was debrided and potted with poly methyl methacrylate bone cement, for subsequent fixation. The distal tibia was exposed by performing direct medial (2 ankles) or posterior lateral (3 ankles) incision. A mallet and osteotome were used to create a 2-, 3-, or 4-fragment pilon fracture as seen in Figure 4.2. A pre-operative CT scan was acquired of each ankle (Siemens SOMATOM Force) with in-plane resolution of 0.23x0.23mm and slice spacing of 0.75 mm. Segmentations of each fracture were performed with the semi-automated method described in Section 3.2.2. Triangulated surface models of the 3D bone morphology were created from these segmentations. Cartilage was unable to be segmented directly from CT, so this surface was extrapolated as a uniform thickness offset from the subchondral bone surface. Using Geomagic Studio software (3D Systems, Rock Hill, SC, USA), subchondral bone region was identified on each fracture fragment by an expert technician. The uniform offset tool offset this selection by 1.4 mm to simulate the articular cartilage thickness in the human ankle joint.

97

This is similar to the procedure performed in Kern and Anderson, 2015, which validated this assumption using DEA in the intact ankle.[65] Hounsfield units from the original CT scan, were converted into linear attenuation coefficients (Section 3.2.2.2) for later processing.[87]
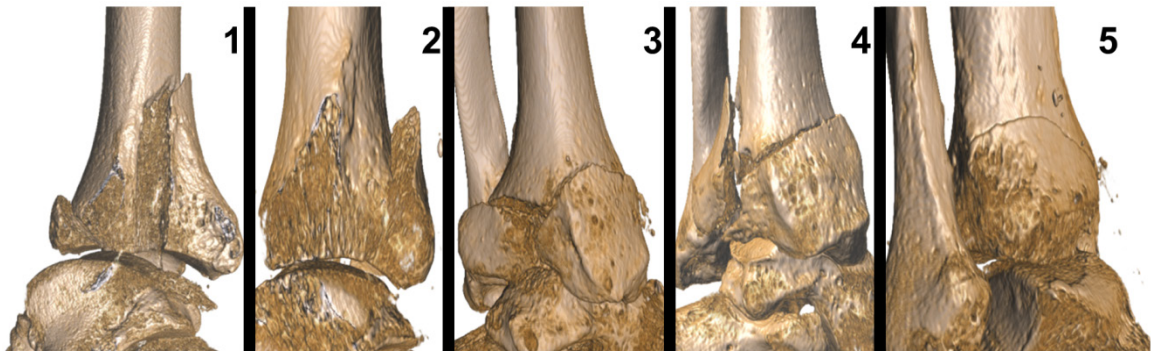
Figure 4.2: Volume renderings of five fractured cadaver ankles. Two, three and four fragment fractures were created with an osteotome and mallet. Case four has complete separation of the articular surface from the diaphysis of the tibia. Renderings performed with ImageVis3D[120].

The cadaver ankles used were amputated mid tibia, and present a different challenge than a clinical case in a live human. Primarily, the amputated shank can easily be rotated to positions which are physically impossible with actual patients. To account for this, a fixation device was created to simulate attachment to a leg as well as hold the calibration device (Section 3.1.2) in registration with the ankle. This fixation device (Figure 4.3) consists of a base plate, an L-shaped offset, and a ball mount connected to the offset. The base is a machined Delrin® (DuPont, USA) plate machined with a socket which receives the calibration object and a grid of threaded anchor points for the offset. The offset is an L-shaped piece of aluminum which lifts the ankle ~10 cm off of the surgical table. It slides superiorly or inferiorly relative to the base to accommodate multiple limb lengths. The ball mount connected to the offset, is a repurposed camera tripod mount that allows the limb a limited range of motion (~40°) simulating attachment to a leg. The end of this

98

tripod mount contains a potting fixture which receives and anchors the proximal end of the potted limb.
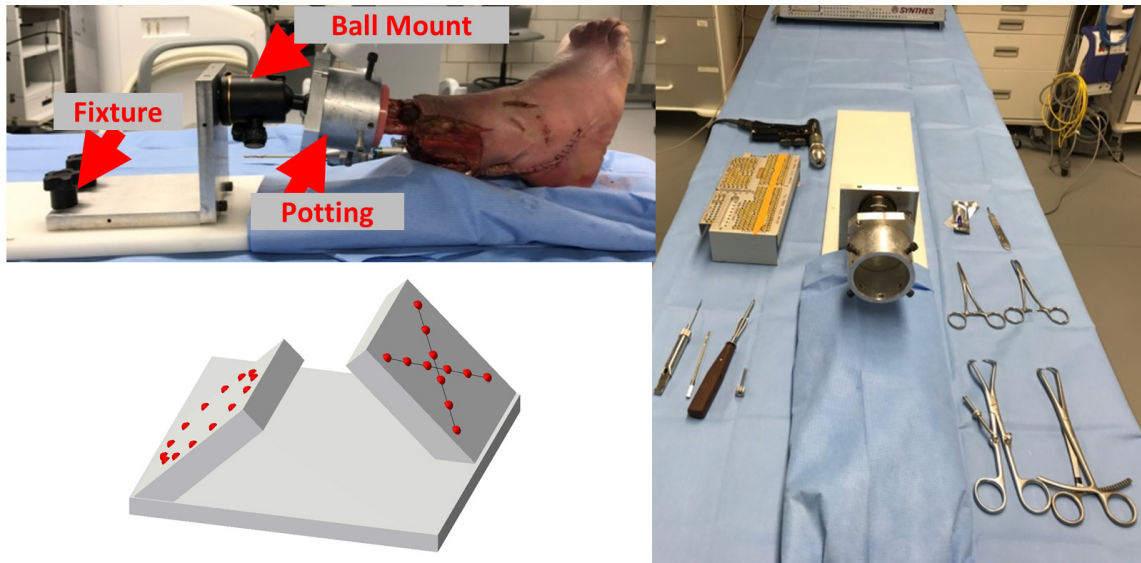
Figure 4.3: Ankle fixture (top left) designed to simulate leg. Calibration device (bottom left) placed within surgical field. Layout and surgical hardware used for percutaneous reduction.

The BGS described in chapter 4 is a computer assisted surgery tool that provides near real-time images of 3D fracture geometry and contact stress distributions. This is performed with minimal disruption to current clinical workflow and low requirements for additional hardware. A small calibration object is the only additional hardware required within the surgical field. A C-arm (Siemens, Cios Fusion) with network communication capabilities, computer workstation with BGS software and a large screen display for presentation of results is also required. (Figure 4.4)
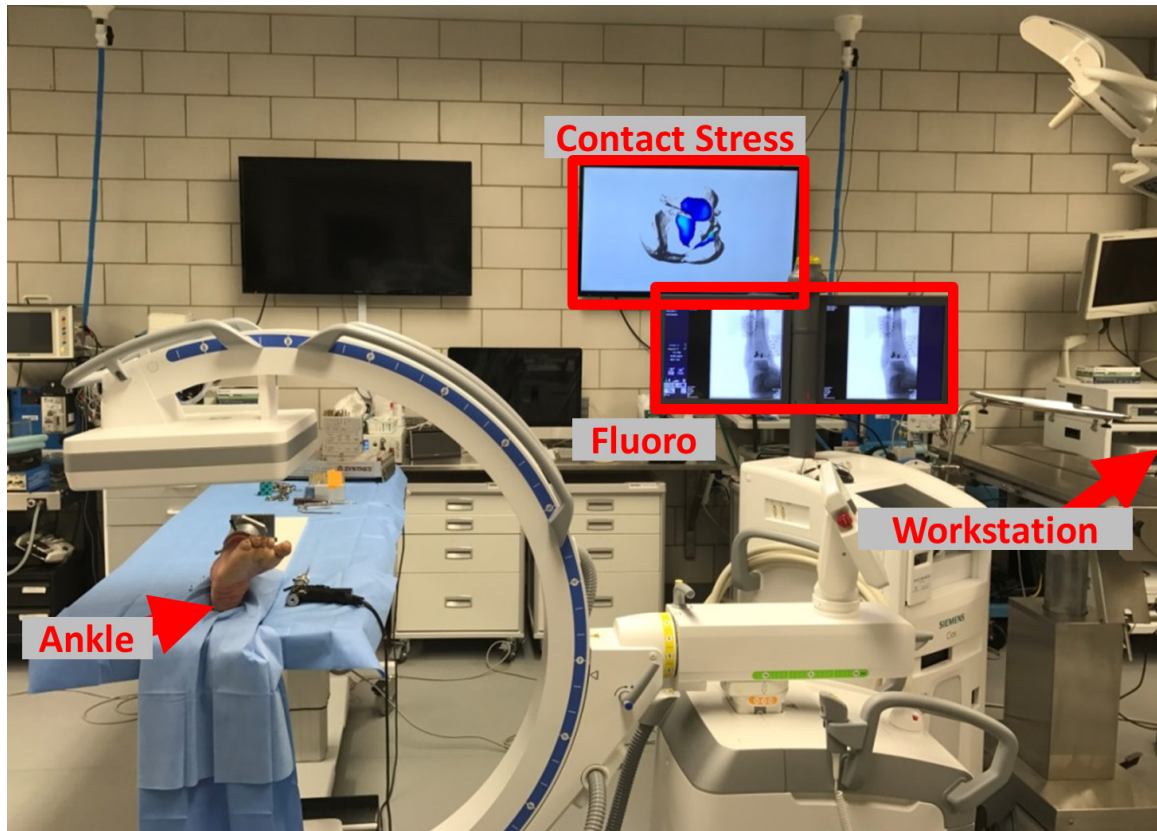
Figure 4.4: Layout of the operating room attempting to recreate a realistic surgical scenario. Ankle is mounted to fixator and imaged with C-arm. A workstation (not pictured) is used to compute BGS results and display 3D geometry and contact stress results on a large screen display.

When the BGS is used, the fluoroscopy tech obtains two images, separated by at least 30°.[121] In our experience, standard AP and lateral views of the ankle have proven to be the most practical. These images are transferred to the computer workstation and the BGS software computes the 3D positioning of individual fracture fragments. The 3D model of these fragments is displayed to the surgeon. During this display a subsequent biomechanical analysis is run to estimate articular contact stress under a standardized loading challenge. Upon completion these data are also presented to the surgeon. (Figure 4.5)
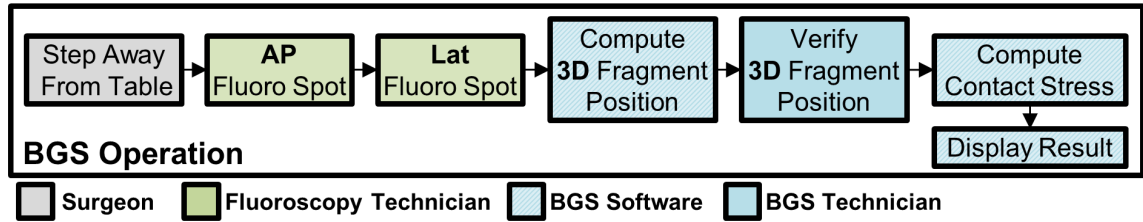
Figure 4.5: Sequence of events when BGS system is run. The operating surgeon indicates desire for additional data and steps-back from the patient to ensure no motion occurs between AP and lateral fluoro shots. When bi-plane images are taken, the BGS technician proceeds with automated alignment of 3D fragment positions. This is verified manually and semi-automated corrections are performed by the technician. Contact stress is then computed automatically by the BGS software and results are displayed to the surgeon.

Percutaneous reductions on the five fractured ankles were performed by a fellowship trained orthopaedic trauma surgeon using standard surgical fixation hardware (Figure 4.3, right). Two trials were performed with each ankle, one with BGS information display, and one without. The BGS system was used during both trials, regardless of output to the surgeon. These trials were separated by at least 48 hours, between which fixation was removed and soft tissue incisions sutured. In all cases, the system was run once prior to the surgery, to provide pre-operative information. Throughout the course of the reduction, whenever the surgeon felt the need for additional information, the BGS system was run to display both 3D geometry and contact stress. This was performed as requested by the surgeon. Following completion of reduction the fracture was definitively fixed, and the BGS system was run a final time to obtain post-op results. Three dimensional geometry and contact stress results were, only shown on one of the two trials for each surgery. The ordering of display/no display trials was randomized in attempt to mitigate training effects. Post-op CT scans were performed following each fracture reduction to serve as a gold standard for fragment positioning and contact stress distributions.

The two trials were compared in terms of number of fluoroscopy shots, surgical time, post-op fracture geometry and post-op contact stress distributions. Geometrical and

101

contact stress results of the BGS system were compared with results from a post-op CT scan. Post-op scans were segmented in the same manner as the pre-op scans where individual fracture fragments were identified.

Geomagic Studio was used to align post-op CT segmentations to the post-op BGS results. In order to bring CT and BGS data into a common reference frame, a rigid transformation aligning the CT diaphyseal fragment to the BGS diaphyseal fragment was applied to all CT bone fragments. Each post-op CT fragment was then aligned to its corresponding BGS fragment. The translation and rotation needed to bring these two geometries into alignment was recorded. In addition, contact stress results were computed using the post-op CT data, and the contact stress distributions were compared to the BGS data in terms of mean stress, max stress and contact area.

To determine spatial correspondence between gold standard (CT) and BGS contact stress distributions, the articular surface of each case was parameterized. A 10x10 cell grid lying in the transverse plane (orthogonal to the long axis of the tibia), was fit to the articular surface of each case. Contact stress distributions were projected to this parametric grid and the mean value within each cell was recorded. (Figure 4.6) Differences between corresponding cells within the grid are compared between gold standard and BGS cases. A Pearson correlation was used to compare contact stress values within each of these parameterized grids, where a correlation was computed for each of the ten surgical trials.
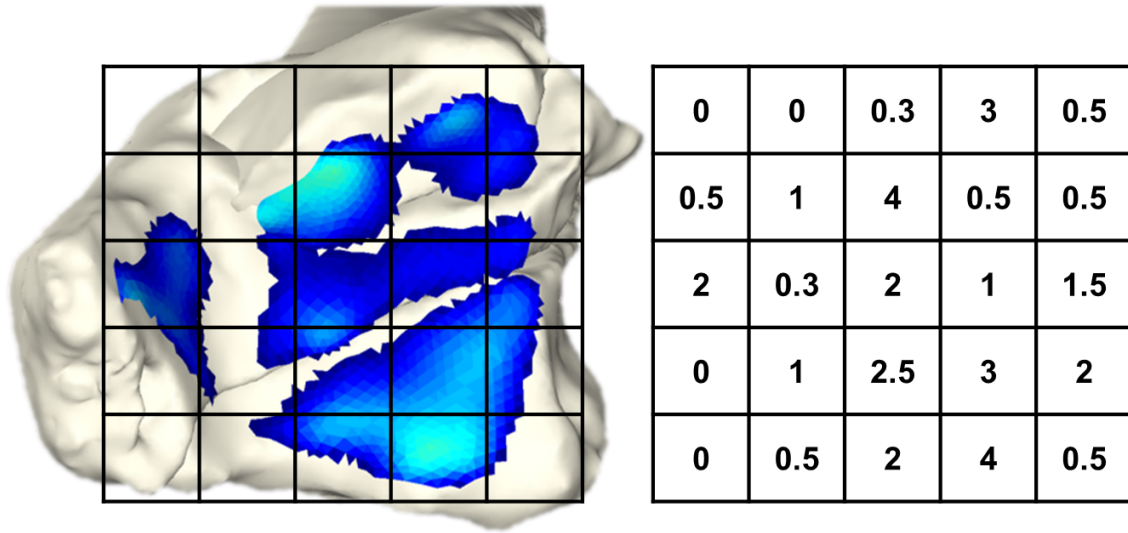
Figure 4.6: Gold standard (from CT) and navigation based (BGS) contact stress distributions were compared by parameterizing the articular surface. Contact stress was projected to a 10x10 grid and mean stress within the cell is recorded. For display purposes, 5x5 grid is shown, stress values are illustrative only.

4.2 RESULTS

When compared to the post-op CT segmentations, it was found that alignment error of the BGS was 0.45±0.57 mm in translation and 2.0±2.5° in rotation. BGS and gold standard contact stress distributions compare well visually. (Figure 4.7) Quantitatively, the difference between BGS and gold standard global mean and maximum contact stress were 0.45±0.36 MPa and 1.0±0.97 MPa, respectively. Comparison of spatial contact stress distributions, found that 89.1% and 96.1% of the grid cells had a contact stress difference < 1.0 MPa and <2.0MPa, respectively. Correlation between grid cells ranged from [0.39 to 0.97] (all correlations have p <0.001) with a median of 0.8250.

www.manaraa.com
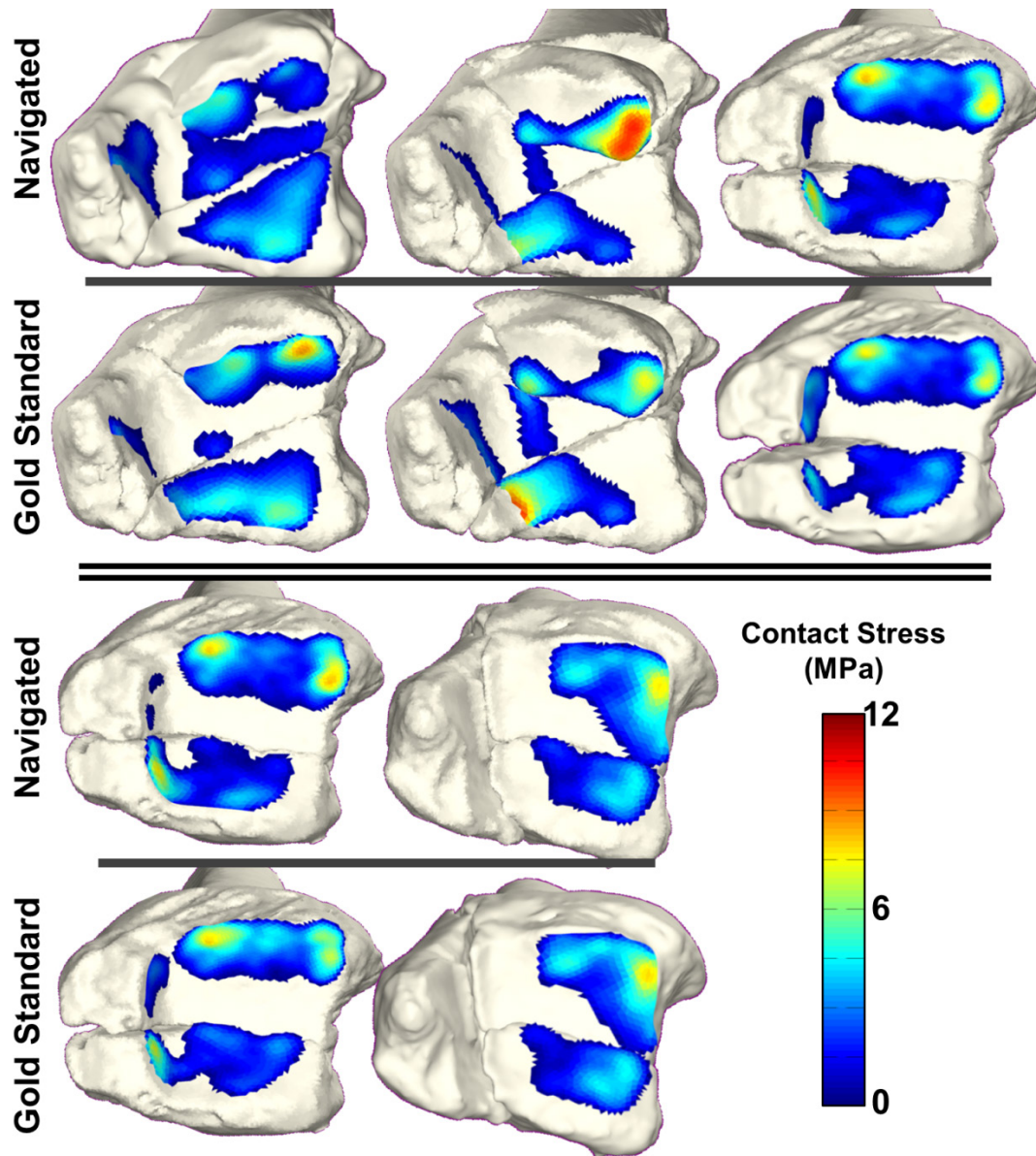
Figure 4.7: Contact stress distribution of post-op CT (Gold Standard) and BGS (Navigated) results following definitive fixation. Includes cases both with/without BGS display to the surgeon. Visually contact stress results compare well between the BGS system and gold standard.
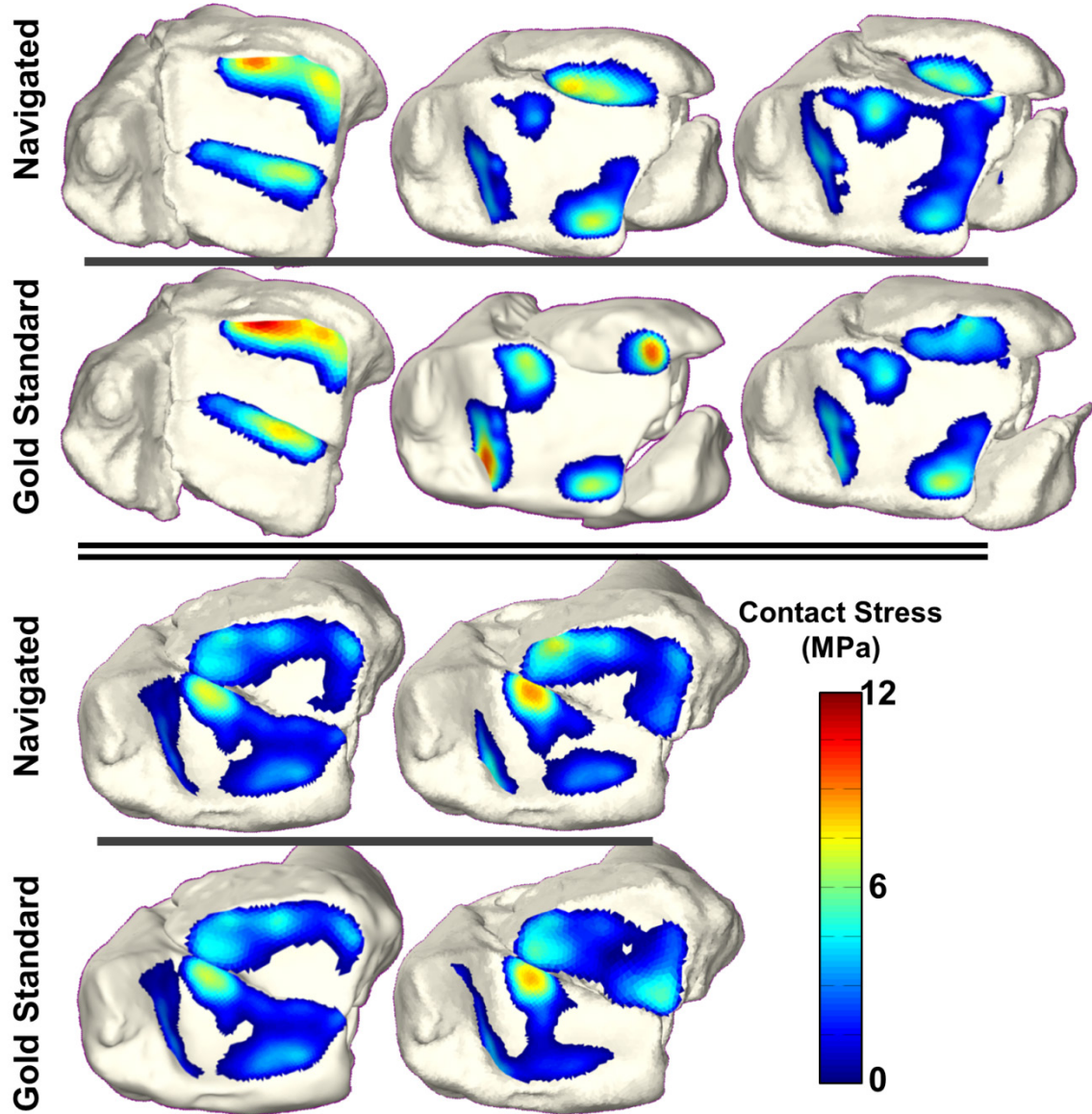
Figure 4.8: Contact stress distribution of post-op CT (Gold Standard) and BGS (Navigated) results following definitive fixation. Includes cases both with/without BGS display to the surgeon. Visually contact stress results compare well between the BGS system and gold standard.

Guidance   **No Guidance**

Contact Stress (MPa)

0   6   12
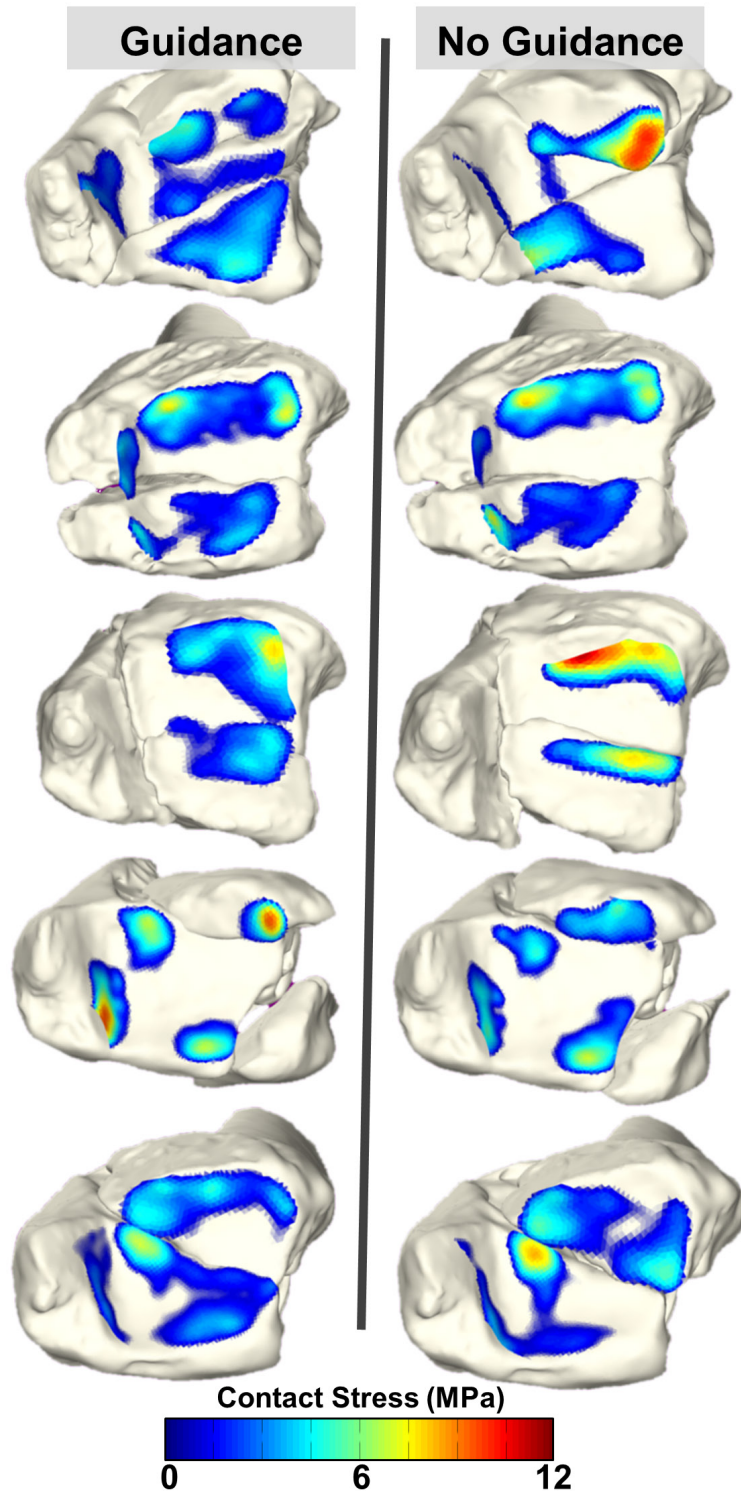
Figure 4.9: Final contact stress distributions of all five cases with (left) and without (right) BGS visualization.

Definitive reduction and fixation was completed successfully for all ten trials. The BGS system was used on average 4.8±1.3 times per procedure. BGS visualization increased the required surgical time by an average of 10 minutes (39% increase) and the number of fluoroscopy shots by 31.2 (17% increase). Use of BGS visualization showed mean and maximum contact stress was reduced by 0.7 and 1.5 MPa, respectively. (Figure 4.10) The contact stress area-engagement histogram presented in Figure 4.11 shows that cases using the BGS had lower contact areas at higher contact stress magnitudes.
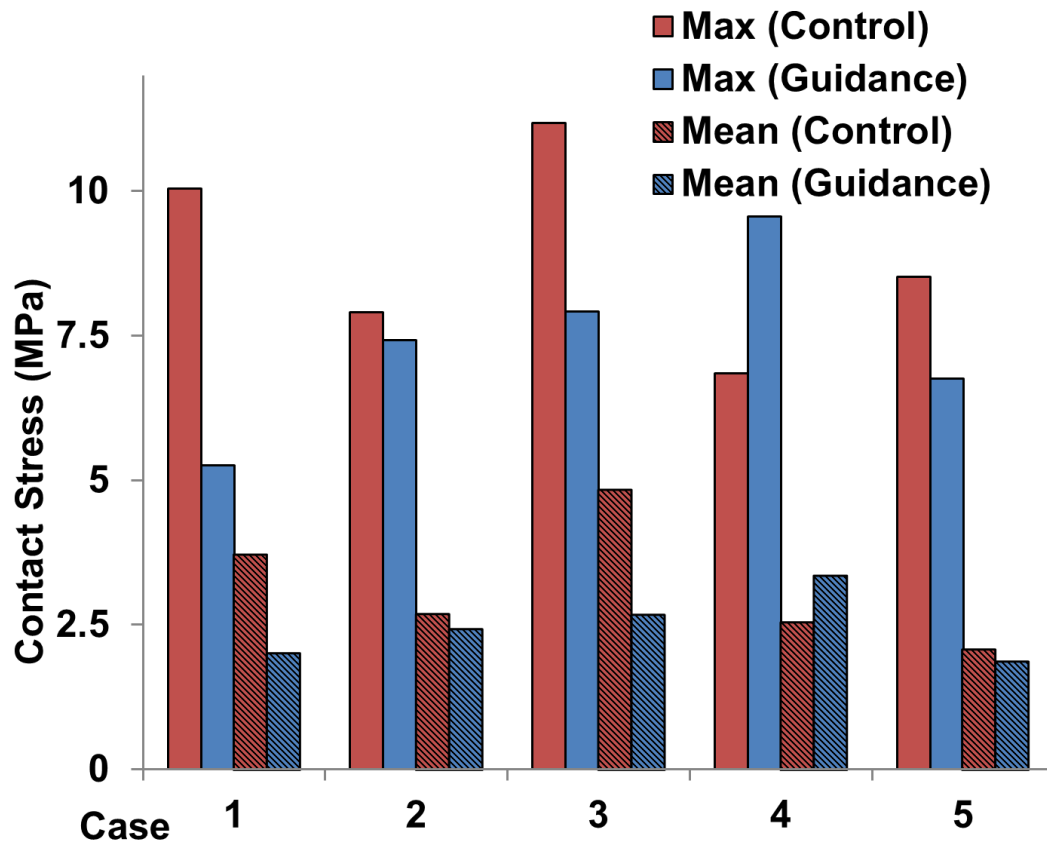
Figure 4.10: Final contact stress metrics with/without use of BGS guidance Mean and maximum contact stress were reduced with BGS in four of five cases.
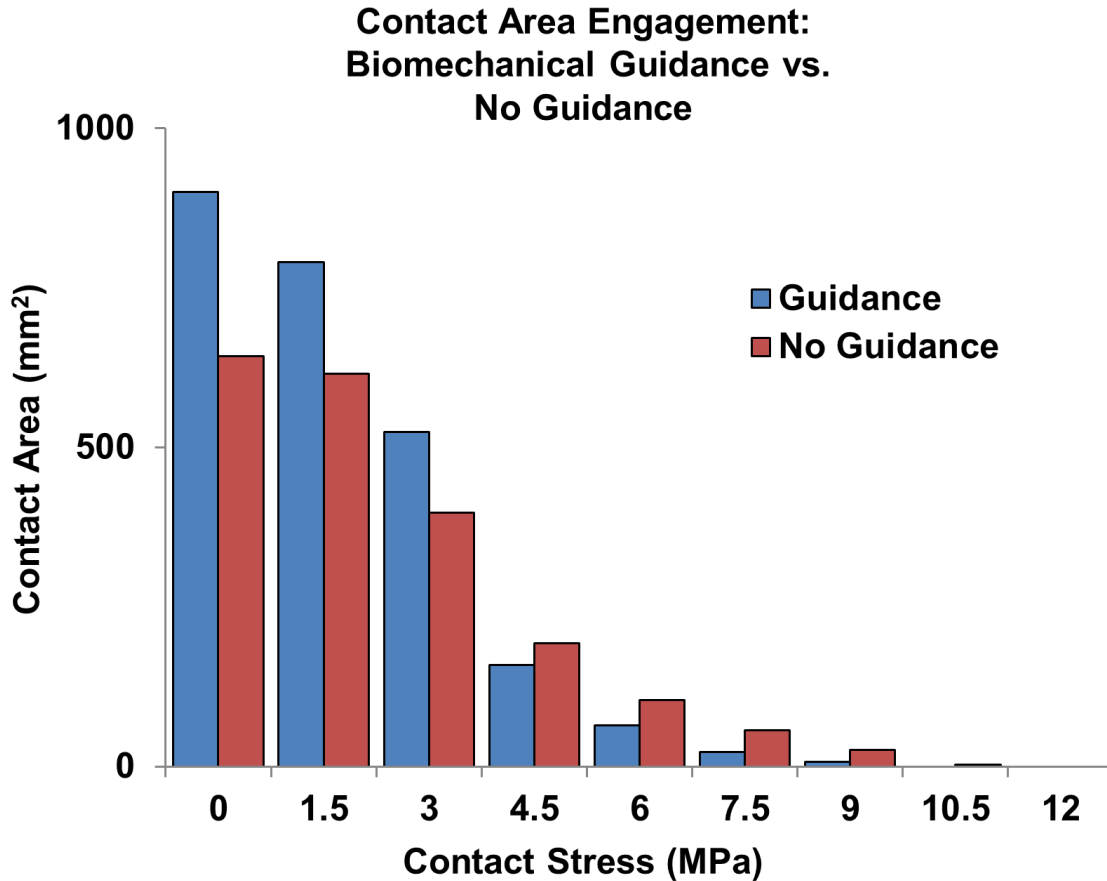
Figure 4.11: Contact area engagement of all cases with BGS display vs without. Cases which received display have lower contact area at contact stress magnitudes known to be deleterious.

4.3 DISCUSSION

The BGS, as presented here, performs well in practice. It minimized alteration to current clinical workflow and allowed the surgeon to maintain agency over the procedure. The small increase in required operative time (10 min) is acceptable within the context of a fracture reduction surgery. It is perhaps expected that surgical time will increase, if advanced measurement techniques are put in place. When using the BGS, a reduction which appears acceptable on fluoroscopy, may now appear problematic with biomechanical data causing the surgeon to continue operation, thus extending operation time. This is supported by the increased number of fluoroscopy shots, as it indicates the surgeon is using the BGS to further analyze and manipulate the fracture rather than

simply taking longer to interpret information. It is unlikely that operation of the BGS (computation time or shots taken for registration) had an effect on surgical time or fluoroscopy images, as the BGS system was used in both trials (guided and unguided). While the increased number of fluoroscopy images does represent an increased level of radiation exposure (17% on average), it is unlikely to be realized in any significant clinical effect. With usage of pulsed fluoroscopy, this represents less than one additional second of exposure time and additional dose area product less than $1 \, dGy * cm^2$. This slight increase in exposure must also be tempered against possible improvement in long-term outcomes. Prevention or delay of PTOA will reduce radiation exposure, disability, and operative cost introduced by future joint arthroplasty or arthrodesis.

Usage of this BGS, compares favorably with that of other computer assisted surgery techniques aimed at articular fractures and joint contact stress. Murphy et al. 2014, who to the best of our knowledge coined the term "Biomechanical Guidance System", demonstrated their system in a series of 19 periacetabular osteotomy cases.[57] While it presents both biomechanical and geometrical results, their system relies upon placement of optical fiducial markers necessitating a significant alteration of current practice. They do not report surgical times. Dagnino et al. 2017, report usage of a robotic system for fracture reduction, in a series of simple distal femur fractures they report surgical times on the order of 100 minutes (~ 40 minutes longer than our longest surgery).[56] This system utilizes a hybrid of optical tracking with 2D-3D registration to perform fragment positioning and requires anchoring of a large metallic implant in each fragment. Such an approach may scale poorly with large numbers of fragments, or small fragment size. Their use of robotic manipulation of fragments vastly alters the role of the orthopaedic

109

surgeon and it is unclear how easily manual intervention could be performed if the robotic system fails.

Fracture fragment registration accuracy of our system compared to post-operative CT is also acceptable. Accuracy of the system in surgical use suffers compared to publicly available gold-standard data (Section 3.4.4), likely due to the presence of surgical hardware, image noise and accumulation of error due to small motions of the fracture (between bi-plane shots). There was also an appreciable amount of time between fixation of the fracture, and acquisition of post-op CT, during which the positioning of bone fragments may have drifted. While every effort was taken to prevent this error, it cannot be guaranteed that small motions did not occur. These findings are mirrored when compared to other guidance systems, where in general systems defined for pure "research" use report accuracy in excess of the BGS system (typically on the order of 0.2 mm and 0.5°).[23, 122] Systems such as this typically have the luxury of using a more controlled setup, with carefully selected view angles and long registration times (sometimes >1 hour for one registration). When compared to systems used in a clinical "intra-operative" scenario, the BGS compares quite well. Again, Dagnino et al. 2017 has reported registration accuracy on the order of 1.0±0.5 mm with their robotic surgical system.[56] This is reported as surface target registration error (sTRE) which measures surface deviations instead of rigid body motion so it is not directly comparable. It is also worth noting that their system requires between 26 and 52 minutes to perform one image-based registration intraoperatively. Murphy et al. 2014, reported registration accuracy on the order of 1.4mm and 1.0° using their optical-tracking-based biomechanical system.[57]

When using biomechanical guidance, it is important to understand not only the registration accuracy of fragments, but the impact that registration error has on biomechanical results. The discrete element analysis (DEA) algorithm used to compute articular contact stress has been previously validated in the human ankle, however the impact subtle motions of the articular surface are unknown.[65] Comparison of the CT-based gold-standard with the BGS contact stress distributions is favorable. Despite this, one case (case 4) was an outlier compared to the other four fractures. Case four is the only fracture with a complete articular separation from the diaphysis of the tibia. While the articular block (three distal fragments) was securely reduced and fixed, it was not plated to the tibial shaft. During biomechanical analysis, the primary loading axis is aligned with the long axis of the tibia. Without rigid fixation between the articular surface and the tibial shaft it is possible that there was a large shift between completion of surgery and CT acquisition. This may significantly change articular loading and contact stress patterns. If case four is treated as an outlier and removed from the results, there spatial correlation between BGS and gold standard is improved to [0.61 to 0.97] with a median of 0.84 (R - value). Removal of case four changes global measures such that the difference in mean and maximum contact stress is 0.39 and 0.95 MPa, respectively.

On average, trials where BGS information was displayed showed a decrease in global contact stress vs cases without BGS information. This trend was consistent across all cases except for case 4 (again likely due to complete articular fracture). Cases which received biomechanical guidance, also showed reduced contact area engaged at high levels of contact stress previously shown to be deleterious (>4.5 MPa)[40]; Overall, contact area above this level was shown to reduce contact area by 44% compared to cases

111

without guidance. This evidence is overall indicative that the BGS system may improve fracture reduction outcomes. The current test serves as a preliminary exploration of this methodology and is insufficiently powered to determine long-term efficacy. A primary limitation of this study is the small sample size of ankle fractures examined (n = 5). This study was intended to be a proof-of-concept exploration of the BGS system to provide motivation for further work and insight to potential improvements. As such no robust statistical efficacy outcomes can be drawn.

During use of the BGS, many observations were made about potential improvements and limitations of the BGS. Since two fluoroscopy images are required for 2D-3D registration, a single C-arm must be manually adjusted to obtain these images. Within this interval any motion of the surgical field must be avoided to maintain registration accuracy. In practice it requires a ~30 second delay as the C-arm is rotated to obtain a second image. The calibration object must also be fully visible within both fluoroscopy images, and its placement may be difficult depending on the specific usage of this system. These constraints, while tangible, seem insignificant compared to the complexity of instrumentation involved with other similar systems. In the future, a second C-arm could be utilized to obtain truly bi-plane images to mitigate a portion of this limitation. While registration of individual bone-fragments is largely automated, the chance of registration failure is always present, particularly when bone fragments are faintly present or occluded by surgical hardware. Currently, detection and remediation of failed registration, is dependent on the vigilance of the technician operating the BGS software. This process while not particularly time-consuming is likely subject to the skill and experience of the given software operator. Difficulty in automating detection of a "good"

112

registration from a "failed" registration is inherent to the methodology used. Despite this, several recent publications have shown promising results with automating registration verification.[52, 53] Future development of the BGS may adapt and implement some of these methods for more robust automation. Biomechanical results computed with this system assume that all of the fracture fragments are rigidly fixed in space. Currently, there are no plans to address this limitation as ultimately the success of a reduction relies on the surgeon achieving stable definitive fixation. Contact stress in the BGS is currently computed in a single static pose, and as such contact stress-time exposure reported in previous studies (Section 2.1.3) is unable to be computed.[8-10, 65] This is primarily a constraint of computation time, and future optimization of the DEA algorithm may allow simulation of a full gait cycle (stance phase).

These ten surgeries represent the initial usage of this system in a clinically realistic scenario. Operation of the BGS software and hardware in such a scenario requires proficiency from the technician. As additional experience is gained and the BGS system is modified to improve usability it is expected that results will likely improve as well. This is also the first exposure of the orthopaedic surgeon to the BGS, or even the concept of intra-operative biomechanical feedback. A significant learning curve is also expected for the clinician where surgical time, fluoroscopy usage, and biomechanical results will further improve. Only one clinician performed the fracture reductions in this study, further exploration is required to determine how additional surgeons perform with the BGS.

CHAPTER 5: SUMMARY

This work attempts to address a significant shortcoming in surgical reduction of intra-articular fractures: accurate assessment of reduction of the articular surface. Currently, assessment is performed by measuring articular step-off through direct visualization, digital manipulation or fluoroscopic imaging. The accuracy and reliability of these methods, particularly fluoroscopic imaging, have been drawn into question. Failure to achieve a high quality fracture reduction, places the joint at increased risk for development of post-traumatic osteoarthritis and subsequent joint arthroplasty or arthrodesis.

Contributions of this work include: novel metrics for assessment of articular fracture reduction quality, development of a biomechanical guidance system which assesses reduction quality intra-operatively and surgical evaluation of the BGS to establish its usability and efficacy.

5.1 ARTICULAR FRACTURE REDUCTION METRICS

- Cohort of 10 post-op fracture reductions were used to examine seven metrics of articular reduction quality.
    - Three 2D CT measurements to represent "best case" clinical evaluation, performed by a clinician.
    - Three novel 3D metrics from CT segmentation, performed by a trained technician.
    - One biomechanical measurement, contact stress-time exposure obtained from previous FEA study.
- Clinical CT-based metrics, did not show significant correlation with 2 year post-op KL-Grade, while 3D and biomechanical metrics.
- Contact stress-time exposure had highest correlation with KL grade- and displayed a statistically significantly stronger correlation than 2D measures.

الﻣنارة للاستشارات

www.manaraa.com

5.2 BIOMECHANICAL GUIDANCE SYSTEM

- A biomechanical guidance system was developed to provide 3D fracture geometry and contact stress assessment in the operating room.
  - BGS requires a C-arm fluoroscopy system, a calibration object, and a workstation equipped with BGS software.
  - Minimal modification to current practice.
  - Performed multiple times per procedure with limited additional radiation dosage.

5.3 SURGICAL EVALUATION OF BGS

- BGS was tested on five cadaveric ankle fractures in a clinically realistic scenario.
  - Alignment accuracy comparable to similar systems.
  - Alterations in contact stress as result of registration errors, is relatively small.
- Use of the BGS was successful in all trials (guided and unguided)
  - Reduction of mean and maximum contact stress using BGS.
  - Reduction of contact area at high levels of contact stress.
  - Increased surgical time and radiation exposure.
- Results from preliminary study suggest BGS may facilitate improved fracture reduction and long-term outcomes.

5.4 FUTURE DIRECTION

Although this work represents progress towards improvement of fracture reduction assessment, it only lays the groundwork for future exploration. Additional surgeries need to be performed in the tibial plafond, to build upon existing data and provide statistical power. Improvements to the BGS software are required, ease of use, computation speed, and increased automation all will improve the eventual clinical viability of such a system.

This work can also be extended to additional joints and surgeries. Joint re-alignment osteotomies, such as periacetabular osteotomy are of particular interest. These are highly invasive procedures, where the clinician attempts to improve joint biomechanics. Currently, this is done freehand largely through gestalt intuition of the surgeon. Actual

115

quantitative biomechanical assessment of these operations seems to be a perfect application of this technology.

Ultimately, after significant refinement and verification of this technology, the goal is translation into the patient OR. Hopefully, this work or new methods derived from this work, will facilitate improved long-term outcomes in standard clinical practice.

REFERENCES

1. Heim, U., *The pilon tibial fracture : classification, surgical techniques, results*. **1995**, Philadelphia: W.B. Saunders. xiii, 337 p.

2. Yablon, I.G., Segal, D., and Leach, R.E., *Ankle injuries*. **1983**, New York: Churchill Livingstone. ix, 268 p.

3. Bernstein, J., *Musculoskeletal medicine*. 1st ed. **2003**, Rosemont, Ill.: American Academy of Orthopaedic Surgeons. xxiv, 490 p., 44 p. of plates.

4. Brown, T.D., Johnston, R.C., Saltzman, C.L., Marsh, J.L., and Buckwalter, J.A., *Posttraumatic osteoarthritis: a first estimate of incidence, prevalence, and burden of disease*. **J Orthop Trauma**, **2006**. 20(10): p. 739-44.

5. Saltzman, C.L., et al., *Impact of comorbidities on the measurement of health in patients with ankle osteoarthritis*. **J Bone Joint Surg Am**, **2006**. 88(11): p. 2366-72.

6. Marsh, J.L., et al., *Articular fractures: does an anatomic reduction really change the result?* **J Bone Joint Surg Am**, **2002**. 84-A(7): p. 1259-71.

7. Furman, B.D., Olson, S.A., and Guilak, F., *The development of posttraumatic arthritis after articular fracture*. **J Orthop Trauma**, **2006**. 20(10): p. 719-25.

8. Li, W., Anderson, D.D., Goldsworthy, J.K., Marsh, J.L., and Brown, T.D., *Patient-specific finite element analysis of chronic contact stress exposure after intraarticular fracture of the tibial plafond*. **J Orthop Res**, **2008**. 26(8): p. 1039-45.

9. Anderson, D.D., Van Hofwegen, C., Marsh, J.L., and Brown, T.D., *Is elevated contact stress predictive of post-traumatic osteoarthritis for imprecisely reduced tibial plafond fractures?* **J Orthop Res**, **2011**. 29(1): p. 33-9.

10. Anderson, D.D., et al., *Post-traumatic osteoarthritis: improved understanding and opportunities for early intervention*. **J Orthop Res**, **2011**. 29(6): p. 802-9.

11. Crist, B.D., Khazzam, M., Murtha, Y.M., and Della Rocca, G.J., *Pilon fractures: advances in surgical management*. **J Am Acad Orthop Surg**, **2011**. 19(10): p. 612-22.

12. Salton, H.L., Rush, S., and Schuberth, J., *Tibial plafond fractures: limited incision reduction with percutaneous fixation*. **J Foot Ankle Surg**, **2007**. 46(4): p. 261-9.

13. McKinley, T.O., Borrelli, J., Jr., D'Lima, D.D., Furman, B.D., and Giannoudis, P.V., *Basic science of intra-articular fractures and posttraumatic osteoarthritis*. **J Orthop Trauma**, **2010**. 24(9): p. 567-70.

14. Garner, M.R., et al., *Standard perioperative imaging modalities are unreliable in assessing articular congruity of ankle fractures*. **J Orthop Trauma**, **2015**. 29(4): p. e161-5.

15. Ebraheim, N., Sabry, F.F., and Mehalik, J.N., *Intraoperative imaging of the tibial plafond fracture: a potential pitfall*. **Foot Ankle Int**, **2000**. 21(1): p. 67-72.

16. Borrelli, J., Jr., Goldfarb, C., Catalano, L., and Evanoff, B.A., *Assessment of articular fragment displacement in acetabular fractures: a comparison of computerized tomography and plain radiographs*. **J Orthop Trauma**, **2002**. 16(7): p. 449-56; discussion 456-7.

17. Buchler, L., Tannast, M., Bonel, H.M., and Weber, M., *Reliability of radiologic assessment of the fracture anatomy at the posterior tibial plafond in malleolar fractures*. **J Orthop Trauma**, **2009**. 23(3): p. 208-12.

18. Capo, J.T., Kinchelow, T., Orillaza, N.S., and Rossy, W., *Accuracy of fluoroscopy in closed reduction and percutaneous fixation of simulated Bennett's fracture*. **J Hand Surg Am**, **2009**. 34(4): p. 637-41.

19. Nelson, E.M., Monazzam, S.M., Kim, K.D., Seibert, J.A., and Klineberg, E.O., *Intraoperative fluoroscopy, portable X-ray, and CT: patient and operating room personnel radiation exposure in spinal surgery*. **Spine J**, **2014**. 14(12): p. 2985-91.

20. Berris, T., Gupta, R., and Rehani, M.M., *Radiation dose from cone-beam CT in neuroradiology applications*. **AJR Am J Roentgenol**, **2013**. 200(4): p. 755-61.

21. Stiehl, J.B., Konermann, W.H., Haaker, R.G., and III, A.M.D., *Navigation and MIS in Orthopaedic Surgery*, **2007**, Springer-Verlag: Berlin. p. 608.

22. Davis, E.T., et al., *A comparison of registration errors with imageless computer navigation during MIS total knee arthroplasty versus standard incision total knee arthroplasty: a cadaveric study*. **Comput Aided Surg**, **2015**. 20(1): p. 7-13.

23. Markelj, P., Tomazevic, D., Likar, B., and Pernus, F., *A review of 3D/2D registration methods for image-guided interventions*. **Med Image Anal**, **2010**.

24. Uneri, A., et al., *Known-Component 3D-2D Registration for Image Guidance and Quality Assurance in Spine Surgery Pedicle Screw Placement*. **Proc SPIE Int Soc Opt Eng**, **2015**. 9415.

25. Otake, Y., et al., *Intraoperative image-based multiview 2D/3D registration for image-guided orthopaedic surgery: incorporation of fiducial-based C-arm tracking and GPU-acceleration*. **IEEE Trans Med Imaging**, **2012**. 31(4): p. 948-62.

26.   Ma, B., Stewart, J., Pichora, D., Ellis, R., and Abolmaesumi, P., *2D/3D registration of multiple bones.* **Conf Proc IEEE Eng Med Biol Soc**, **2007**. 2007: p. 860-3.

27.   Haque, M.A., Anderst, W., Tashman, S., and Marai, G.E., *Hierarchical model-based tracking of cervical vertebrae from dynamic biplane radiographs.* **Med Eng Phys**, **2013**. 35(7): p. 994-1004.

28.   Gong, R.H., Stewart, J., and Abolmaesumi, P., *Multiple-object 2-D-3-D registration for noninvasive pose identification of fracture fragments.* **IEEE Trans Biomed Eng**, **2011**. 58(6): p. 1592-601.

29.   Valderrabano, V., Horisberger, M., Russell, I., Dougall, H., and Hintermann, B., *Etiology of ankle osteoarthritis.* **Clin Orthop Relat Res**, **2009**. 467(7): p. 1800-6.

30.   Saltzman, C.L., et al., *Epidemiology of ankle arthritis: report of a consecutive series of 639 patients from a tertiary orthopaedic center.* **Iowa Orthop J**, **2005**. 25: p. 44-6.

31.   Stufkens, S.A.S., van den Bekerom, M.P.J., Kerkhoffs, G.M.M.J., Hintermann, B., and van Dijk, C.N., *Long-term outcome after 1822 operatively treated ankle fractures: A systematic review of the literature.* **Injury-International Journal of the Care of the Injured**, **2011**. 42(2): p. 119-127.

32.   Berkes, M.B., et al., *Articular congruity is associated with short-term clinical outcomes of operatively treated SER IV ankle fractures.* **J Bone Joint Surg Am**, **2013**. 95(19): p. 1769-75.

33.   DeCoster, T.A., et al., *Rank order analysis of tibial plafond fractures: does injury or reduction predict outcome?* **Foot Ankle Int**, **1999**. 20(1): p. 44-9.

34.   Williams, T.M., et al., *Factors affecting outcome in tibial plafond fractures.* **Clin Orthop Relat Res**, **2004**(423): p. 93-8.

35.   Wyrsch, B., et al., *Operative treatment of fractures of the tibial plafond. A randomized, prospective study.* **J Bone Joint Surg Am**, **1996**. 78(11): p. 1646-57.

36.   Lubbeke, A., et al., *Risk factors for post-traumatic osteoarthritis of the ankle: an eighteen year follow-up study.* **Int Orthop**, **2012**. 36(7): p. 1403-10.

37.   Horisberger, M., Valderrabano, V., and Hintermann, B., *Posttraumatic ankle osteoarthritis after ankle-related fractures.* **J Orthop Trauma**, **2009**. 23(1): p. 60-7.

38.   Anderson, D.D., et al., *Quantifying tibial plafond fracture severity: absorbed energy and fragment displacement agree with clinical rank ordering.* **J Orthop Res**, **2008**. 26(8): p. 1046-52.

119

39. Thomas, T.P., et al., *Objective CT-based metrics of articular fracture severity to assess risk for posttraumatic osteoarthritis.* **J Orthop Trauma**, **2010**. 24(12): p. 764-9.

40. Anderson, D.D., Van Hofwegen, C., Marsh, J.L., and Brown, T.D., *Is elevated contact stress predictive of post-traumatic osteoarthritis for imprecisely reduced tibial plafond fractures?* **J Orthop Res**, **2010**.

41. Buckwalter, J.A., Anderson, D.D., Brown, T.D., Tochigi, Y., and Martin, J.A., *The Roles of Mechanical Stresses in the Pathogenesis of Osteoarthritis: Implications for Treatment of Joint Injuries.* **Cartilage**, **2013**. 4(4): p. 286-294.

42. Fitzpatrick, D.C., Otto, J.K., McKinley, T.O., Marsh, J.L., and Brown, T.D., *Kinematic and contact stress analysis of posterior malleolus fractures of the ankle.* **J Orthop Trauma**, **2004**. 18(5): p. 271-8.

43. Hak, D.J., Hamel, A.J., Bay, B.K., Sharkey, N.A., and Olson, S.A., *Consequences of transverse acetabular fracture malreduction on load transmission across the hip joint.* **J Orthop Trauma**, **1998**. 12(2): p. 90-100.

44. Miller, A.N., et al., *Direct visualization for syndesmotic stabilization of ankle fractures.* **Foot Ankle Int**, **2009**. 30(5): p. 419-26.

45. Liu, Z. and Stasko, J.T., *Mental models, visual reasoning and interaction in information visualization: a top-down perspective.* **IEEE Trans Vis Comput Graph**, **2010**. 16(6): p. 999-1008.

46. Hu, C.H., Kundel, H.L., Nodine, C.F., Krupinski, E.A., and Toto, L.C., *Searching for bone fractures: a comparison with pulmonary nodule search.* **Acad Radiol**, **1994**. 1(1): p. 25-32.

47. Berlin, L., *Defending the "missed" radiographic diagnosis.* **AJR Am J Roentgenol**, **2001**. 176(2): p. 317-22.

48. Marmor, M., Hansen, E., Han, H.K., Buckley, J., and Matityahu, A., *Limitations of standard fluoroscopy in detecting rotational malreduction of the syndesmosis in an ankle fracture model.* **Foot Ankle Int**, **2011**. 32(6): p. 616-22.

49. de Muinck Keizer, R.O., et al., *Articular Gap and Step-off Revisited: 3D Quantification of Operative Reduction for Posterior Malleolar Fragments.* **J Orthop Trauma**, **2016**. 30(12): p. 670-675.

50. Conconi, M., Halilaj, E., Castelli, V.P., and Crisco, J.J., *Is early osteoarthritis associated with differences in joint congruence?* **Journal of Biomechanics**, **2014**. 47(16): p. 3787-3793.

51. Grimson, E. and Kikinis, R., *Registration for Image-Guided Surgery.* **Handbook of Medical Image Processing and Analysis, 2nd Edition**, **2009**: p. 695-705.

52.   Varnavas, A., Carrell, T., and Penney, G., *Fully automated 2D-3D registration and verification.* **Med Image Anal**, **2015**. 26(1): p. 108-19.

53.   Varnavas, A., Carrell, T., and Penney, G., *Increasing the automation of a 2D-3D registration system.* **IEEE Trans Med Imaging**, **2013**. 32(2): p. 387-99.

54.   Gong, R.H., Stewart, J., and Abolmaesumi, P., *Multiple-Object 2-D-3-D Registration for Noninvasive Pose Identification of Fracture Fragments.* **Ieee Transactions on Biomedical Engineering**, **2011**. 58(6): p. 1592-1601.

55.   Zheng, G., Dong, X., and Gruetzner, P.A., *Reality-augmented virtual fluoroscopy for computer-assisted diaphyseal long bone fracture osteosynthesis: a novel technique and feasibility study results.* **Proc Inst Mech Eng H**, **2008**. 222(1): p. 101-15.

56.   Dagnino, G., et al., *Intra-operative fiducial-based CT/fluoroscope image registration framework for image-guided robot-assisted joint fracture surgery.* **Int J Comput Assist Radiol Surg**, **2017**.

57.   Murphy, R.J., et al., *Development of a biomechanical guidance system for periacetabular osteotomy.* **Int J Comput Assist Radiol Surg**, **2015**. 10(4): p. 497-508.

58.   Marsh, J.L., Borrelli, J., Jr., Dirschl, D.R., and Sirkin, M.S., *Fractures of the tibial plafond.* **Instr Course Lect**, **2007**. 56: p. 331-52.

59.   Meijer, D.T., et al., *Diagnostic Accuracy of 2-Dimensional Computed Tomography for Articular Involvement and Fracture Pattern of Posterior Malleolar Fractures.* **Foot & Ankle International**, **2016**. 37(1): p. 75-82.

60.   Kellgren, J.H. and Lawrence, J.S., *Radiological assessment of osteo-arthrosis.* **Ann Rheum Dis**, **1957**. 16(4): p. 494-502.

61.   Besl, P.J. and Mckay, N.D., *A Method for Registration of 3-D Shapes.* **Ieee Transactions on Pattern Analysis and Machine Intelligence**, **1992**. 14(2): p. 239-256.

62.   Anderson, D.D., et al., *Physical validation of a patient-specific contact finite element model of the ankle.* **J Biomech**, **2007**. 40(8): p. 1662-9.

63.   Meng, X.L., Rosenthal, R., and Rubin, D.B., *Comparing Correlated Correlation-Coefficients.* **Psychological Bulletin**, **1992**. 111(1): p. 172-175.

64.   Grosland, N.M., et al., *IA-FEMesh: an open-source, interactive, multiblock approach to anatomic finite element model development.* **Comput Methods Programs Biomed**, **2009**. 94(1): p. 96-107.

121

65. Kern, A.M. and Anderson, D.D., *Expedited patient-specific assessment of contact stress exposure in the ankle joint following definitive articular fracture reduction.* **J Biomech**, **2015**. 48(12): p. 3427-32.

66. Abraham, C.L., et al., *A new discrete element analysis method for predicting hip joint contact stresses.* **J Biomech**, **2013**. 46(6): p. 1121-7.

67. Ateshian, G.A., Henak, C.R., and Weiss, J.A., *Toward patient-specific articular contact mechanics.* **J Biomech**, **2015**. 48(5): p. 779-86.

68. Thomas, T.P., et al., *ASB Clinical Biomechanics Award Paper 2010 Virtual pre-operative reconstruction planning for comminuted articular fractures.* **Clin Biomech (Bristol, Avon)**, **2011**. 26(2): p. 109-15.

69. Kern, A.M.A., D.D., *Toward Clinically Applicable Reconstruction Planning for Comminuted Articular Fractures* in *American Society of Biomechanics***2013**: Omaha, NE.

70. Graves, M.L., *The value of preoperative planning.* **J Orthop Trauma**, **2013**. 27 Suppl 1: p. S30-4.

71. Prince, J.L. and Links, J.M., *Medical imaging signals and systems*. 2. ed. xvii, 519 p.

72. Nickoloff, E.L., *AAPM/RSNA physics tutorial for residents: physics of flat-panel fluoroscopy systems: Survey of modern fluoroscopy imaging: flat-panel detectors versus image intensifiers and more.* **Radiographics**, **2011**. 31(2): p. 591-602.

73. Fahrig, R. and Holdsworth, D.W., *Three-dimensional computed tomographic reconstruction using a C-arm mounted XRII: image-based correction of gantry motion nonidealities.* **Med Phys**, **2000**. 27(1): p. 30-8.

74. Gutierrez, L.F., Ozturk, C., McVeigh, E.R., and Lederman, R.J., *A practical global distortion correction method for an image intensifier based x-ray fluoroscopy system.* **Med Phys**, **2008**. 35(3): p. 997-1007.

75. Navab, N., et al., *Dynamic geometrical calibration for 3-D cerebral angiography.* **Physics of Medical Imaging**, **1996**. 2708: p. 361-370.

76. Fahrig, R., Moreau, M., and Holdsworth, D.W., *Three-dimensional computed tomographic reconstruction using a C-arm mounted XRII: correction of image intensifier distortion.* **Med Phys**, **1997**. 24(7): p. 1097-106.

77. Cho, Y., Moseley, D.J., Siewerdsen, J.H., and Jaffray, D.A., *Accurate technique for complete geometric calibration of cone-beam computed tomography systems.* **Med Phys**, **2005**. 32(4): p. 968-83.

78. Schmidt, J. and Niemann, H. *Using Quaternions for Parameterizing 3-D Rotations in Unconstrained Nonlinear Optimization*. in **VMV**. **2001**. Stuttgart, Germany.

79. Grassia, S.F., *Practical Parameterization of Rotations Using the Exponential Map.* **The Journal of Graphical Tools**, **1998**. 3(3): p. 13.

80. Beucher, S., *Watershed, hierarchical segmentation and waterfall algorithm.* **Mathematical Morphology and Its Applications to Image Processing**, **1994**. 2: p. 69-76.

81. Paulhac, L., Ramel, J.Y., and Renard, T., *Interactive Segmentation of 3D Images Using a Region Adjacency Graph Representation.* **Image Analysis and Recognition: 8th International Conference, Iciar 2011, Pt I**, **2011**. 6753: p. 354-364.

82. Birngruber, E., Donner, R., and Langs, G., *MatVTK - 3D Visualization for Matlab.* **The MIDAS Journal- Systems and Architectures for Computer Assisted Interventions**, **2009**.

83. Kolmogorov, V. and Zabih, R., *What energy functions can be minimized via graph cuts?* **Ieee Transactions on Pattern Analysis and Machine Intelligence**, **2004**. 26(2): p. 147-159.

84. Delong, A., Osokin, A., Isack, H.N., and Boykov, Y., *Fast Approximate Energy Minimization with Label Costs.* **International Journal of Computer Vision**, **2012**. 96(1): p. 1-27.

85. Boykov, Y. and Kolmogorov, V., *An experimental comparison of min-cut/max-flow algorithms for energy minimization in vision.* **Ieee Transactions on Pattern Analysis and Machine Intelligence**, **2004**. 26(9): p. 1124-1137.

86. Boykov, Y., Veksler, O., and Zabih, R., *Efficient Approximate Energy Minimization via Graph Cuts.* **IEEE TPAMI**, **2001**. 20(12): p. 1222-1239.

87. Brown, S., Bailey, D.L., Willowson, K., and Baldock, C., *Investigation of the relationship between linear attenuation coefficients and CT Hounsfield units using radionuclides for SPECT.* **Applied Radiation and Isotopes**, **2008**. 66(9): p. 1206-1212.

88. Hartley, R.Z., A., *Multiple View Geometry in Computer Vision*. Second ed. **2004**: Cambridge University Press.

89. Li, X., Da, Z., and Liu, B., *A generic geometric calibration method for tomographic imaging systems with flat-panel detectors--a detailed implementation guide.* **Med Phys**, **2010**. 37(7): p. 3844-54.

90. Illingworth, J. and Kittler, J., *The Adaptive Hough Transform*. **Ieee Transactions on Pattern Analysis and Machine Intelligence**, **1987**. 9(5): p. 690-698.

91. Fischler, M.A. and Bolles, R.C., *Random Sample Consensus - a Paradigm for Model-Fitting with Applications to Image-Analysis and Automated Cartography*. **Communications of the Acm**, **1981**. 24(6): p. 381-395.

92. Sonka, M., Hlavac, V., and Boyle, R., *Image processing, analysis, and machine vision*. 3rd ed. **2008**, Toronto: Thompson Learning. xxv, 829 p.

93. Halir, R. and Flusser, J., *Numerically stable direct least squares fitting of ellipses*. **Wscg '98, Vol 1**, **1998**: p. 125-132.

94. Moore, C.S., Liney, G.P., Beavis, A.W., and Saunderson, J.R., *A method to produce and validate a digitally reconstructed radiograph-based computer simulation for optimisation of chest radiographs acquired with a computed radiography imaging system*. **Br J Radiol**, **2011**. 84(1006): p. 890-902.

95. Dorgham, O.M., Laycock, S.D., and Fisher, M.H., *GPU accelerated generation of digitally reconstructed radiographs for 2-D/3-D image registration*. **IEEE Trans Biomed Eng**, **2012**. 59(9): p. 2594-603.

96. Zhao, H.X. and Reader, A.J., *Fast ray-tracing technique to calculate line integral paths in voxel arrays*. **2003 Ieee Nuclear Science Symposium, Conference Record, Vols 1-5**, **2004**: p. 2808-2812.

97. Siddon, R.L., *Prism Representation - a 3d Ray-Tracing Algorithm for Radiotherapy Applications*. **Physics in Medicine and Biology**, **1985**. 30(8): p. 817-824.

98. Witkin, A., Terzopoulos, D., and Kass, M., *Signal Matching through Scale Space*. **International Journal of Computer Vision**, **1987**. 1(2): p. 133-144.

99. Penney, G.P., et al., *A comparison of similarity measures for use in 2-D-3-D medical image registration*. **IEEE Trans Med Imaging**, **1998**. 17(4): p. 586-95.

100. Powell, M.J.D., *The BOBYQA algorithm for bound constrained optimization without derivatives* **2009**, Cambridge University: DAMTP.

101. Nelder, J.A. and Mead, R., *A Simplex-Method for Function Minimization*. **Computer Journal**, **1965**. 7(4): p. 308-313.

102. Mistree, F., Hughes, O.F., and Phuoc, H.B., *An Optimization Method for the Design of Large, Highly Constrained Complex-Systems*. **Engineering Optimization**, **1981**. 5(3): p. 179-197.

103. Box, M.J., *A New Method of Constrained Optimization and a Comparison with Other Methods*. **Computer Journal**, **1965**. 8(1): p. 42-52.

124

104. Marchelli, G.L.S., Haynor, D.R., Ledoux, W.R., Ganter, M.A., and Storti, D.W., *Graphical User Interface for Human Intervention in 2d-3d Registration of Medical Images.* **Proceedings of the Asme International Design Engineering Technical Conferences and Computers and Information in Engineering Conference, 2013, Vol 7a**, **2014**.

105. NVidia, *CUDA Programming Guide v8.0*, **2017**: http://docs.nvidia.com/cuda/cuda-c-programming-guide/index.html.

106. Deriche, R., *Recursively implementing the Gaussian and its derivatives*, in *Robotique, Image et Vision***1993**, Institut NAtional de Recherche en Informatique et en Automatique. p. 24.

107. NVidia, *CUDA v8.0 Code Examples*, **2017**: https://developer.nvidia.com/cuda-zone.

108. Johnson, S.G., *The NLopt nonlinear-optimization package.*

109. OFFIS, *DCMTK*, **1994-2017**.

110. Bei, Y. and Fregly, B.J., *Multibody dynamic simulation of knee contact mechanics.* **Med Eng Phys**, **2004**. 26(9): p. 777-89.

111. An, K.N., Himeno, S., Tsumura, H., Kawai, T., and Chao, E.Y., *Pressure distribution on articular surfaces: application to joint stability evaluation.* **J Biomech**, **1990**. 23(10): p. 1013-20.

112. Blankevoort, L., Kuiper, J.H., Huiskes, R., and Grootenboer, H.J., *Articular contact in a three-dimensional model of the knee.* **J Biomech**, **1991**. 24(11): p. 1019-31.

113. Chao, E.Y., Volokh, K.Y., Yoshida, H., Shiba, N., and Ide, T., *Discrete element analysis in musculoskeletal biomechanics.* **Mol Cell Biomech**, **2010**. 7(3): p. 175-92.

114. Tomazevic, D., Likar, B., and Pernus, F., *"Gold standard" data for evaluation and comparison of 3D/2D registration methods.* **Comput Aided Surg**, **2004**. 9(4): p. 137-44.

115. Tomazevic, D., Likar, B., Slivnik, T., and Pernus, F., *3-D/2-D registration of CT and MR to X-ray images.* **IEEE Trans Med Imaging**, **2003**. 22(11): p. 1407-16.

116. Knirk, J.L. and Jupiter, J.B., *Intra-articular fractures of the distal end of the radius in young adults.* **J Bone Joint Surg Am**, **1986**. 68(5): p. 647-59.

117. Marsh, J.L., Weigel, D.P., and Dirschl, D.R., *Tibial plafond fractures. How do these ankles function over time?* **J Bone Joint Surg Am**, **2003**. 85-A(2): p. 287-95.

125

118. Keizer, R.J.O.D., et al., *Articular Gap and Step-off Revisited: 3D Quantification of Operative Reduction for Posterior Malleolar Fragments.* **Journal of Orthopaedic Trauma**, **2016**. 30(12): p. 670-675.

119. Wilson, W., van Donkelaar, C.C., van Rietbergen, R., and Huiskes, R., *The role of computational models in the search for the mechanical behavior and damage mechanisms of articular cartilage.* **Med Eng Phys**, **2005**. 27(10): p. 810-26.

120. CIBC, *ImageVis3D*, **2016**, Scientific Computing and Imaging Institute p. An interactive visualization software system for large-scale volume data. .

121. Uneri, A., et al., *3D-2D registration for surgical guidance: effect of projection view angles on registration accuracy.* **Phys Med Biol**, **2014**. 59(2): p. 271-87.

122. Markelj, P., Tomazevic, D., Pernus, F., and Likar, B.T., *Robust gradient-based 3-D/2-D registration of CT and MR to X-ray images.* **IEEE Trans Med Imaging**, **2008**. 27(12): p. 1704-14.

123. Leclercq, G., Lefevre, P., and Blohm, G., *3D kinematics using dual quaternions: theory and applications in neuroscience.* **Frontiers in Behavioral Neuroscience**, **2013**. 7.

124. Thomas, F., *Approaching Dual Quaternions From Matrix Algebra.* **Ieee Transactions on Robotics**, **2014**. 30(5): p. 1037-1048.

125. Kenwright, B., *A Beginners Guide to Dual-Quaternions What They Are, How They Work, and How to Use Them for 3D Character Hierarchies.* **Wscg'2012, Conference Proceedings, Pts I & Ii**, **2012**: p. 1-10.

APPENDIX A: BRIEF OVERVIEW OF DUAL QUATERNIONS

Quaternions, discovered by Hamilton in 1866, are an extension of complex numbers to a four dimensional vector. A quaternion, q, is has four scalar elements, $\langle w, x, y, z \rangle$ where:

$$q = w + ix + jy + kz$$

The symbols i, j, k represent imaginary components which, similar to complex numbers, are subject to specific properties:

$$i^2 = j^2 = k^2 = -1$$

$$ij = k, \qquad ji = -k$$

$$jk = i, \qquad kj = -i$$

$$ki = j, \qquad ik = -j$$

Typically in computer graphics a single unit quaternion, $\|q\| = 1$, is used to represent rigid rotation in three dimensional space. Conveniently, this can be interpreted as a rotation of angle, θ, about axis, n, where n is a three dimensional unit vector.

$$q = \langle w, x, y, z \rangle = \langle cos\left(\frac{\theta}{2}\right), n\, sin\left(\frac{\theta}{2}\right) \rangle$$

Dual quaternions are combination of dual numbers with quaternions, as a means of representing both translations and rotations. Dual numbers are similar to complex numbers as they contain a real and dual component. The similar to an imaginary number, i, there is a dual number, ε, which has special properties:

127

$$\varepsilon^2 = 0, \qquad \varepsilon \neq 0$$

From this the concept of a dual quaternion follows which contains both a real and dual component represented as a quaternion and denoted as q_r, and q_d, respectively.

$$q = q_r + \varepsilon q_d$$

With this set of rules, elementary operations for addition, multiplication, conjugation, and normalization can be derived allowing for a compact and robust representation of rigid transformation. Further reading, and theoretical foundations of dual quaternions can be found in Thomas 2014, and Leclercq et al. 2013.[123, 124] Kenwright 2012 has also published a simple primer focused on the practical aspects of dual quaternions and their implementation.[125]

APPENDIX B: ALGORITHMS FOR 2D-3D POINT CORRESPONDENCE

Algorithm: Find Point Correspondences

function PAIRPOINTS(*image*, *ref, refLines, refCircle*)

in:	*image*	– sequence of n pairs (i, j)
		– coordinates of bearings in fluoroscopy image
	ref	– sequence of m triplets (x, y, z)
		– coordinates of bearings in reference object
	refLines	– array of 2 x p indices to *ref*
		– *p* is the number of bearings in a line on the reference object.
		– indices ordered geometrically
	refCircle	– sequence of k indices to *ref*
		– *k* is the number of bearings in the circle on the reference object
		– indices are ordered geometrically
out:	*ptPairs*	– sequence of indices. Maps *image* to *ref*

1. *test* ← indices(*image*)
2. *ellipse* ← FINDELLIPSE(*test, image*)
3. *test* ← *test \ ellipse*
4. *line1* ← FINDLINE(*test, image*)
5. *test* ← *test \ line1*
6. *line2* ← FINDLINE(*test, image*)
7. *inliers* ← 0
8. **while** | *inliers* | < | *ellipse* | + | *line1* | + | *line2* | **do**
9.   *circlePairs* ← random permutation mapping *ellipse* to *refCircle*
        // maintain ordering of circles
10.   *linePairs* ← random permutation mapping *line1* and *line2* to *refLines*
        // maintain ordering of lines
11. x ← image(*linePairs*) || image(*circlePairs*)
12. X ← ref (*refLines*) || ref(*refCircles*)
13. P ← COMPUTEP(x, X)   // gold standard algorithm from Hartley and Zisserman
14. x_{prime} ← $P·X$ // compute reprojection
15.   *dists* ← $\| x_{prime} - x \|$ // compute reprojection error
16.   *inliers* ← *dists* < ε   // find number of points with reprojection error < ε
17. **end while**
18. x_{prime} ← $P·$ ref   // compute reprojection with all reference points
19. *dists* ← $\| x_{prime} - image \|$ // compute reprojection error with all points (n x m matrix)
20. [*refPairs* , *imagePairs*] ← BIPARTITEMATCHING(*dists*)
        // find minimum cost matching (assignment) of pairs
21. *ptPairs* ← *refPairs* || *imagePairs*

Algorithm: Find Ellipse Within Set of Points Containing Outliers

function FINDELLIPSE(*points*)

in: *points* – sequence of n pairs (i, j)
                         – coordinates of bearings in fluoroscopy image

out: *ellipsePts* – sequence of indices to *points*
                         – sorted clockwise from center of ellipse

1. *inliers* ← 0
2. **while** | *inliers* | < 12 **do**   // Highly unlikely to find twelve incorrect inliers
3.   *testPts* ← randomly select 6 indices ∈ *points*
4.   *testEllipse* ← FITELLIPSE(*points*(*testPts*))
5.   *dists* ← find distance from *testEllipse* to *points*   // distance to all points
6.   *inliers* ← *dists* < ε   // determine if there is a concensus with error < ε
7. **end while**
8. *ellipse* ← FITELLIPSE(*points*(*inliers*))   // refit ellipse with full concensus of inliers
9. *dists* ← find distance from *ellipse* to *points*   // distance to all points
10. *ellipsePts* ← *dists* < ε   // determine final concensus set with refit ellipse
11. *ellipsePts* ← sort *points*(*ellipsePts*)   // sort with polar coordinates (angle) from center of ellipse

Algorithm: Find Line Within Set of Points Containing Outliers

function FINDLINE(*points*)

in: *points*   – sequence of n pairs (i, j)
                         – coordinates of bearings in fluoroscopy image

out: *linePts*   – sequence of indices to *points*
                         – sorted by i coordinate of *points*

1. *inliers* ← 0
2. **while** | *inliers* | < 4 **do**   // Highly unlikely to find four incorrect inliers
3.   *testPts* ← randomly select two indices ∈ *points*
4.   *testLine* ← FITLINE(*points*(*testPts*))
5.   *dists* ← find distance from *testLine* to *points*   // normal distance to all points
6.   *inliers* ← *dists* < ε   // determine if there is a concensus with error < ε
7. **end while**
8. *line* ← FITLINE(*points*(inliers))   // refit line with full concensus of inliers
9. *dists* ← find distance from *line* to *points* // normal distance to all points
10. *linePts* ← *dists* < ε   // determine final concensus set with refit lines
11. *linePts* ← sort *points*(*linePts*)   // sort according to path along the line

130

Execution time of DRR generation and image comparison were computed on a single tibial plafond fracture fragment in two views simultaneously. Image size was varied from the maximum resolution of the fluoroscopy system (1536x1536) to a minimum of $1/4^{th}$ the maximum resolution ($1/16^{th}$ the total number of pixels). For the purposes of the BGS the resolution of 768x768 was used for all computations, representing ~2.5ms of total execution time. (Figure C)
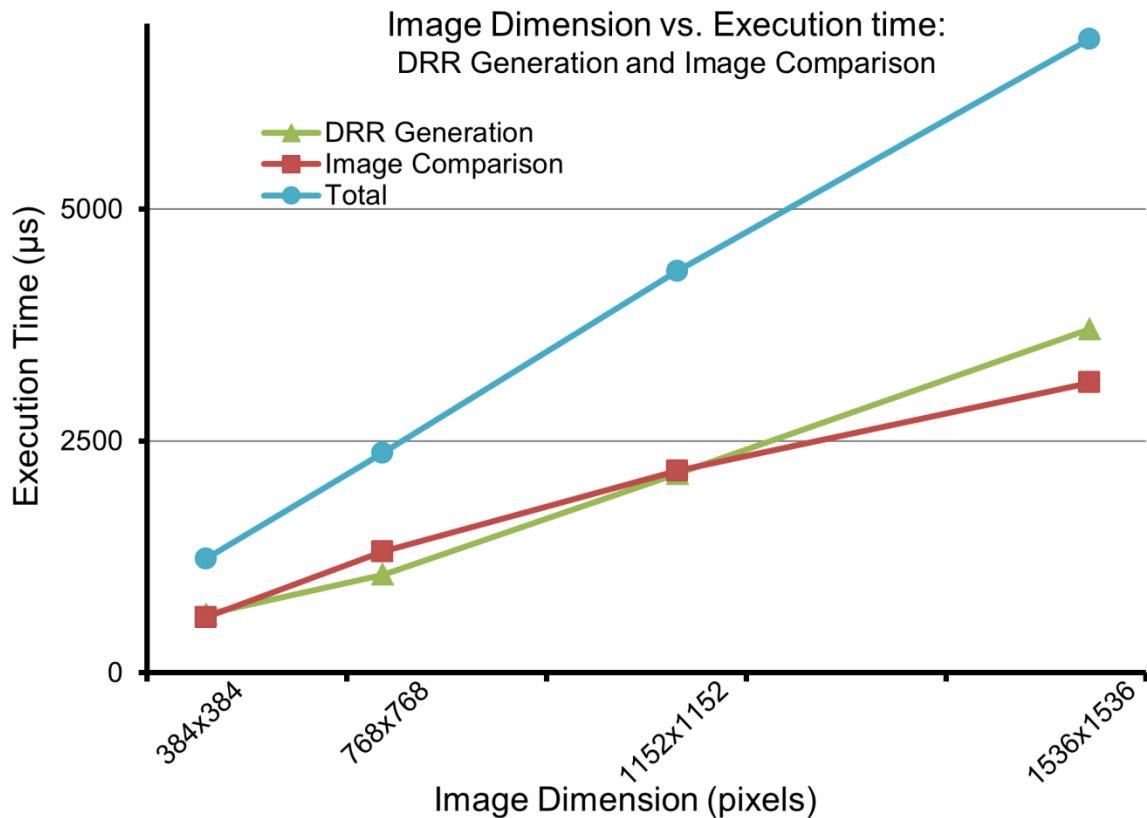

Figure C: Execution time of DRR generation (green) and image comparison (red) were evaluated for multiple image resolutions.

131